ULTRATHIN GRAPHENE OXIDE MEMBRANES FOR WATER PURIFICATION: FUNDAMENTALS & POTENTIAL APPLICATIONS

by

Weiwei Xu

Bachelor of Engineering
Jilin University, 2006

Master of Science
University of South Carolina, 2013

Submitted in Partial Fulfillment of the Requirements

For the Degree of Doctor of Philosophy in

Chemical Engineering

College of Engineering and Computing

University of South Carolina

2017

Accepted by:

Miao Yu, Major Professor

John R. Regalbuto, Committee Member

Christopher Williams, Committee Member

John W. Weidner, Committee Member

Aaron K. Vannucci, Committee Member

Cheryl L. Addy, Vice Provost and Dean of the Graduate School

DEDICATION

To Xuyang who spent all these awful years together with me, and to Amy, my motivation to keep moving on.

"Old chemists never die, they just become engineers"

ACKNOWLEDGEMENTS

I would like to express my deepest gratitude to Professor Miao Yu, my advisor, for his support, encouragement, and patience during these four years graduate study in his research group. Under his guidance, I have learnt a lot, including sense of deep thinking, scientific writing and presentation skills, which would be extremely beneficial to my entire career. I would never have been able to complete this thesis without his help. Sincere thanks also go to my committee members: Professor John Regalbuto, Professor Christopher Williams, Professor John Weidner, and Professor Aaron Vannucci for their valuable time and precious advices.

I would like to thank all the former and current group members in Yu's group: Dr. Xiaojie Zhang, Dr. Yi Huang, Dr. Mahdi Fathizadeh, Dr. Konstantin Khivantsev, Dr. Huynh Ngoc Tien, Dr. Zhuonan Song, Hang Li, Lei Wang, Fanglei Zhou, and Qiaobei Dong for many useful suggestions and discussions about my research.

I would also like to thank the staff in the Chemical Engineering department at University of South Carolina.

Last but not least, I am truthfully grateful to my wife, Xuayang, and my lovely daughter Amy for their continuous love and support.

ABSTRACT

To develop ultrathin GO membranes with both high permeation rate and excellent selectivity, it is essential to understand the interlayer nanostructure and its influence on water purification performance. We purposely deposited GO at a fast rate and at a rate ~12 times slower to control the interlayer nanostructure of the resulting membranes. The d-spacing difference between proposed thermodynamically favored interlayer structure which formed at slow deposition rate and another relative randomly packed interlayer structure formed at fast deposition rate were corroborated by XRD, organic vapor deposition, and AFM. Molecular dynamics simulations further confirmed that, in type I structure, functionalized patches and pristine graphene patches on neighboring GO layers facing themselves, which not only leaded to smaller d-spacing but also facilitated fast water permeation; in type II structure, functionalized and pristine were mismatched, leading to larger d-spacing and drastically retarded water permeation. Our experimental results also showed that compared with type II structure, narrower hydrophobic nanochannels in type I structure lead to 2.5~4 times faster water permeation rate and 1.8~4 times higher salt rejection. We believed our finding, tuning the GO interlayer nanostructure by simply controlling GO flake deposition rate in solution phase deposition process, helped break the current trade-off between water flux and precise sieving performance of GO membranes, and may eventually bring about novel design of ultrathin GO-based membranes for high flux and high selectivity water purification.

After figured out the process-structure-performance relationship of GO membranes, a layer-by-layer deposition method was designed to prepare GO membranes, through this deposition technique, GO layers could have enough time to self-assemble and form the thermodynamically favored structure. To overcome GO's inherent dispensability in the water environment and to lock the d-spacing at sub-nanometer scale, the as-prepared GO membranes were thermally reduced under vacuum. The 3 nm reduced graphene oxide (rGO) membrane exhibited no permeation even for water molecules and then O_2 plasma was introduced to create extra defects on the membrane surface, which dramatically facilitated water permeation but still could block large molecules (such as methylene blue) in high efficiency. By tuning the plasma treatment time, the 3 nm rGO membranes achieved ~98% rejection for MB and pure water flux as high as about 44 $L \cdot h^{-1} \cdot bar^{-1} \cdot m^{-2}$. Moreover, the optimized 10s plasma etched 3 nm rGO also exhibited 100% rejection and good antifouling ability for humic acid.

As the flux cross the membrane decreases with membrane thickness, to balance this pay off between permeability and selectivity, membrane should have thin thickness to provide high flux and appropriate pores to allow the passage of water but block large solutes at the same time. Therefore, the "ultimate" target in membrane science is to fabricate a membrane in the form of only one atomic thickness and with suitable pores on its surface. The properties of GO just meet these two requirements. In this part of research, by clarifying two distinct water transportation mechanisms for membranes with sub-monolayer and multilayer GO coverage, we proposed a methodology to fabricate nominal single-layered GO membrane. While the calculated GO coverage increased from less than 100% to multilayers, the water flux exhibited a transition from two stages of linear

decreases to exponential decrease, the condition to prepare nominal single-layered GO membrane was extrapolated from the turning point of the linear-to-exponential transition, the as-fabricated membrane with thickness closing to one-carbon-atom exhibited high water permeance around 64 L $\cdot h^{-1}$ ƀar^{-1} m^{-2}. In this nominal single-layered GO membrane, defects on GO flakes provided major contribution for its sieving properties. By evaluating the separation performance of this membrane with rigid molecules, the effective defect size of GO was determined to be ~1.2-1.7 nm. This membrane with nominal single-layer GO cover also show great potential in protein separation.

TABLE OF CONTENTS

LIST OF TABLES

LIST OF FIGURES

LIST OF SYMBOLS

L_D The distance of defects on graphene surface.

J Mass flux of water calculated from MD simulation.

J_0 Mass flux predicted using continuum fluid mechanics assuming no-slip boundary condition on the channel wall.

$\bar{V}_{MD}$ Average water velocity in the SLGO channel.

ρ_{MD} Density of water in the SLGO channel.

d Effective SLGO channel width $d = H - d_c$, where H is the channel width (0.69 nm here), and d_c=0.355 nm is the van der Waals diameter of the carbon atom.

μ The shear viscosity of SPC/E water at 300 K.

ρ_{bulk} Density of bulk SPC/E water at 300 K.

μ The shear viscosity of SPC/E water at 300 K.

LIST OF ABBREVIATIONS

AFM.....Atomic Force Microscope

FESEM..... Field-emission Scanning Electron Microscope

FTIR..... Fourier-Transform Infrared Spectroscopy

FO ..... Forward Osmosis

GO..... Graphene Oxide

NF .....Nanofiltration

RO.....Reverse Osmosis

SLGO .....Single Layer Graphene Oxide

XPS ..... X-ray Photoelectron Spectroscopy

CHAPTER 1

INTRODUCTION AND LITERATURE REVIEW

Due to the population boom and rapid industrial development, short of clean water has become a worldwide crisis that could not be ignored. This global water scarcity leads to great demand of high efficient, cost-effective and environmental friendly water treatment technologies.[1,2] Comparing with traditional water purification methods, such as distillation, precipitation, chemical and sorption treatments, nanofiltration (NF), reverse osmosis (RO), and forward osmosis (FO) technologies not only have lower operation cost and energy consumption, but also demonstrated to be efficient ways to remove salts and contaminations from water.[3-5] All these three processes require the use of semipermeable membranes, albeit cellulose acetate based and polyamide composites are two types of most commonly used membranes in industry, graphene and its derivative graphene oxide (GO) have exhibit great potential to replace polymeric membrane materials due to the easy membrane accessibility, chemical and mechanical stabilities, and high antifouling property.[6-9] Thus, in this paper, we are going to review recently reported graphene and graphene oxide based membranes and their application in nanofiltration (NF), reverse osmosis (RO), and forward osmosis (FO) process, respectively.

1.1 STRUCTURE OF GRAPHENE OXIDE

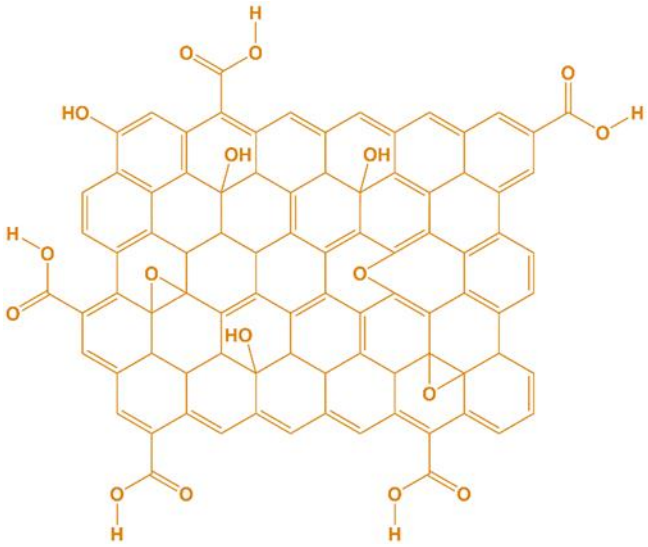

Figure 1.1Chemical structure of graphene oxide (GO) composed of a graphene sheet derivatized by phenyl epoxide and hydroxyl groups on the basal plane and carboxylic acid groups on the edge. Reprinted with permission from ref.31. Copyright 2013 WILEY-VCH Verlag GmbH & Co.

Graphene oxide (GO) is an oxidized form of graphene that is made of carbon atoms bonded in hexagonal honeycomb lattice. Due to the strong oxidation conditions during its synthesis, for example, by Hummers[10] or Staudenmaier[11] method, a large amount of oxygen-containing groups, including epoxide, hydroxyl, and carboxylic acid groups, exist in GO, as shown in Figure 1.1. These functional groups lead to good hydrophilicity and allow excellent dispersion of GO flakes in water. This, as a significant advantage, greatly facilitates GO deposition from solution using water as a low cost and environment-friendly solvent.[12] Recently, GO has attracted great attention as a novel 2-D membrane material in water purification application because of its excellent mechanical property, atomically thin thickness, excellent dispersion in water, and ease to form compact membrane structure or to be added into polymer matrix.[12,13]

1.2 CONCEPT DEMONSTRATIONS OF GRAPHENE-BASED MEMBRANES FOR WATER PURIFICATION

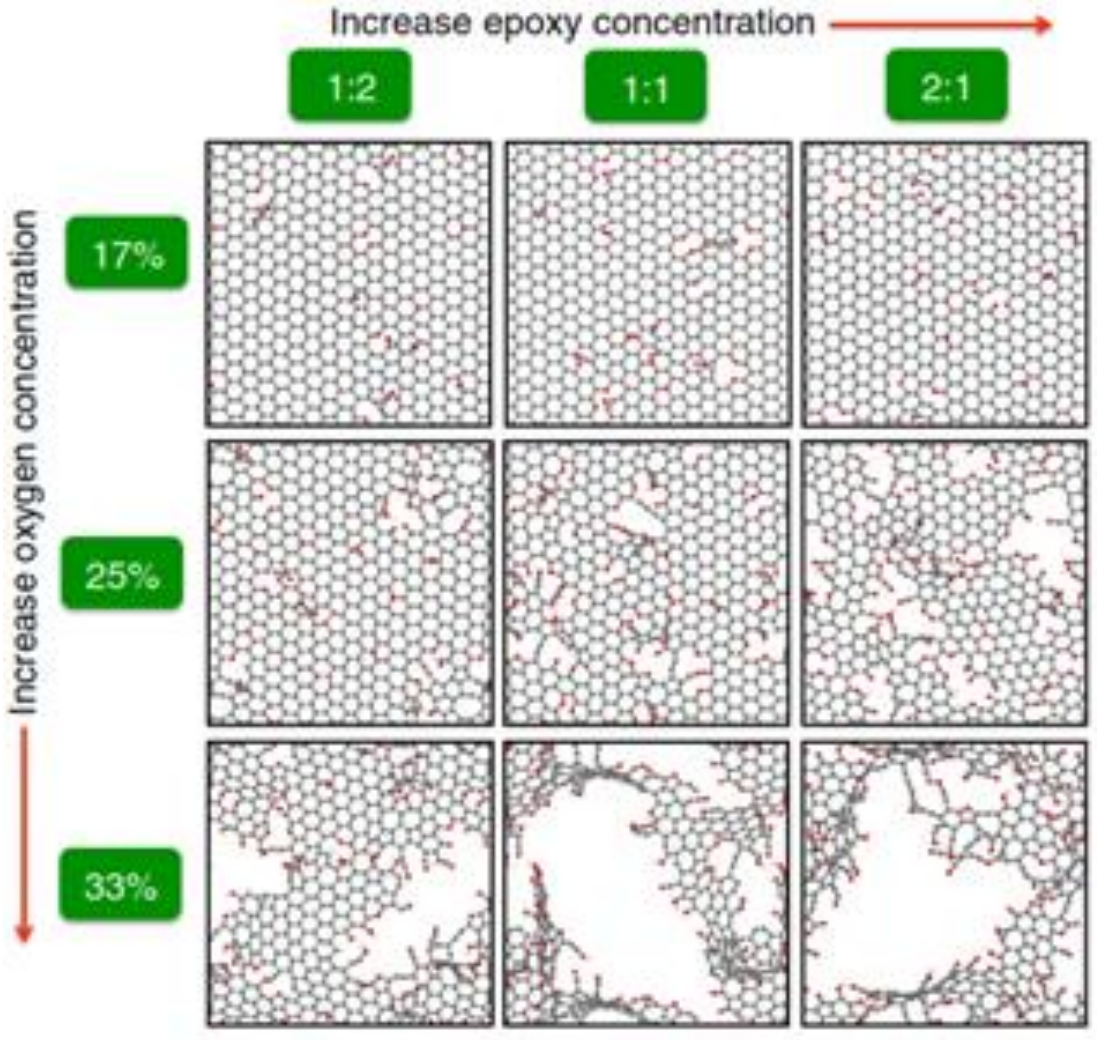

Figure 1.2 Representative defective structures of rGO after reduction at 2,500 K. The epoxy/hydroxyl ratio and initial oxygen concentration of GO sheets are shown along the horizontal and vertical directions, respectively. All structures are represented as ball and stick with carbon, oxygen and hydrogen atoms in grey, red and white color, respectively. Reprinted with permission from ref.15. Copyright 2015 Nature Publishing Group.

Concept demonstration/preliminary studies on using graphene-based membranes for water purification were focused on simulations for single layer graphene/GO/reduced GO (rGO) with structural defects. Cohen-Tanugi *et al.*[14], using molecular dynamics (MD) simulation, found that hydrogenated and hydroxylated defects with appropriate sizes on

graphene could have 2-3 orders of magnitude higher water permeability than commercial reverse osmosis (RO) membranes but similarly high salt rejection, suggesting great potential of single-layered graphene membranes for desalination. Lin *et al*.[15] showed by MD simulations that thermally reducing GO with different initial epoxy to hydroxyl ratios and different oxygen concentrations may generate selective defects on rGO for high water permeability and high salt rejection desalination. Figure 1.2 shows representative structures of rGO after reduction at 2,500 K, when GO flakes with different starting oxygen concentrations and epoxy concentrations or epoxy/hydroxyl ratios are used. With the increase of oxygen concentration and epoxy concentration, rGO becomes more defective and has bigger nanopores because of more carbon removal from the GO matrix. This suggests pores on rGO may be controlled by controlling starting GO composition and reduction conditions. Further, they studied desalination performance of defects on rGO after reduction at different temperatures and using GO with different oxygen concentrations and epoxy concentrations (Table 1.1). Too low oxygen concentration (17%) leads to complete water blocking irrespective of reduction temperature and initial epoxy concentration or epoxy/hydroxyl ratio. At higher initial oxygen concentration (25% and 33%), high water flux and 99% salt rejection can be obtained depending on reduction temperature epoxy/hydroxyl ratio. These promising simulation results, therefore, suggest appropriately reducing GO with desired starting composition may lead to high performance desalination membranes. In another study, permeation of water and ions through functionalized and un-functionalized pores of single layer graphene sheet was investigated using MD simulations.[16] They found that pristine pores with diameter approximately 0.75 nm can effectively exclude ions, whereas ion rejection decreased with the increase of ion

concertation and pore diameter. Comparison among carboxyl anion, amine cation, and hydroxyl groups indicated that carboxyl group had better ion rejection, particularly for Cl^-.

Table 1.1 Separation performance of rGO membranes in water desalination.

Initial oxygen concentration		Water flux (L cm^{-2} $\cdot day^{-1}$ $\cdot MPa^{-1}$)			Salt rejection (%)		
		1:2*	1:1*	2:1*	1:2	1:1	2:1
T = 1500 K	17%	0.0	0.0	0.0	100	100	100
	25%	0.0	0.0	0.0	100	100	100
	33%	0.0	2.6	2.0	100	99	100
T = 2000 K	17%	0.0	0.0	0.0	100	100	100
	25%	0.0	0.0	0.1	100	100	100
	33%	2.1	15.3	(L)	100	99	(L)
T = 2500 K	17%	0.0	0.0	0.0	100	100	100
	25%	0.0	0.0	15.4	100	100	93
	33%	27.4	(L)	(L)	94	(L)	(L)
T = 3000 K	17%	0.0	0.0	0.0	100	100	100
	25%	0.1	3.0	(L)	100	100	(L)
	33%	(L)	(L)	(L)	(L)	(L)	(L)

1.3 APPLICATION OF GRAPHENE-BASED MEMBRANES FOR WATER PURIFICATION

To experimentally demonstrate the feasibility of utilizing structural defects for selective water permeation, several clever experiments have been designed. Surwade *et al*.[17] covered a 5-μm pore with a single layer of graphene with a grain size of 50 μm, and then applied very short time (<10 s) oxygen plasm etching to create nanopores; their results indicated that under certain etching conditions, generated defects had an extremely high water permeability, about 1,000 times higher than commercial RO membranes, and approximately 100% salt rejection. O'Hern *et al*.[18] transferred single layer graphene grown by chemical vapor deposition to a porous polycarbonate substrate and then used ion bombardment and oxidative etching to tune defects sizes on graphene in the sub-nanometer range and thus allow slat transport while excluding organic dye molecules. These experimental studies seem to support the simulation results and show the potential of the structural defects within graphene. However, it is very challenging to make macroscopic, single-layered graphene or GO membranes that have desired structural defects that are the only transport pathway and only allow water permeation.

Another parallel pathway of using GO in membrane fabrication is to form lamellar structure and utilize nano-channels between GO flakes for selective water permeation. As the very first study, Nair *et al*.[19] fabricated approximately micrometer-thick, free-standing GO membranes and found that water vapor permeated through the membrane with negligible transport resistance, but even helium can't permeate through the dry membrane; they also found small organic molecules, such as methanol, acetone, and hexane etc., had several orders of magnitude lower permeability than water. In a following study in 2014[20],

they observed, by liquid phase diffusion experiments, thick GO membranes exhibited a sharp cutoff size of nano-channels at ~0.9 nm; species with hydrated radius lager than ~0.45 nm were sieved out, whereas small species, such as K^+, Mg^{2+} and AsO_4^{3-} ions, permeated with approximately the same rate and showed weak dependence on ion charge (Figure 1.3). These promising preliminary results demonstrated that nano-channels between GO flakes have great potential for highly selective water permeation, and stimulated extensive study of using GO membranes with lamellar structure for water purification. The enhanced water permeability through membranes composed of multiple GO flakes with pores within the flakes and having lamellar structure was studied using atomistic simulations and theoretical analysis to understand the observed water permeation behavior.[21] The physical picture of ultrafast flow between pristine graphene sheets breaks down due to a side-pinning effect by water confined between oxidized regions in GO membranes. Generally, expanded interlayer gallery, wide channels formed at wrinkles, holes, and interedge spaces could prominently improve water flow in GO sheets.[21]

Encouraged by the exciting preliminary experimental demonstrations and simulations, researchers from all over the world are exploring various ways of utilizing 2-D GO to improve membrane performance in water purification. There are three typical ways of fabricating GO-incorporated membranes: i) lamellar-structured membranes with GO as the skeleton material; ii) mixed matrix membranes (MMM) with GO as the additive; and iii) GO surface functional coatings. Figure 1.4 shows representative membrane structures formed via these three ways. In structure I, nano-channels between GO flakes in parallel dominate the molecular permeation, and current research is focused on modifying GO surface properties, controllably depositing GO flakes to form more ordered lamellar

structure, and tuning the nano-channel size (physically and chemically).[21-23] In structure II, GO serves as a functional additive to modify the properties of the matrix membrane (typically hydrophobic), such as hydrophilicity and surface roughness, to improve surface hydrophilicity and antifouling performance, and/or to introduce extra transport pathways.[21,23] In structure III, GO acts as a functional coating that changes the contacting material with the feed liquid, and thus may work as a protective layer, antibacterial and antifouling coating.[21,23,24]

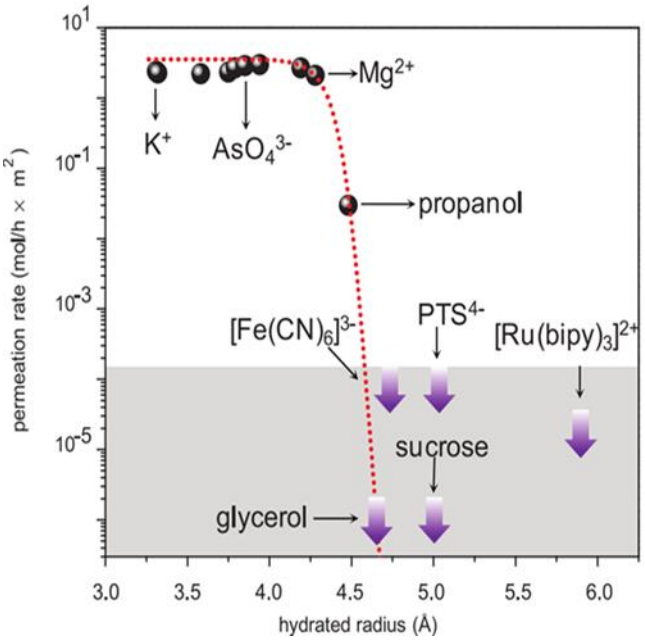

Figure 1.3 Permeation rate of ions and neutral molecules with different hydrated radius through GO membranes. Permeation rates are normalized per 1 M feed solution and measured by using 5-μm-thick membranes. Reprinted with permission from ref.15. Copyright 2014 American Association for the Advancement of Science.

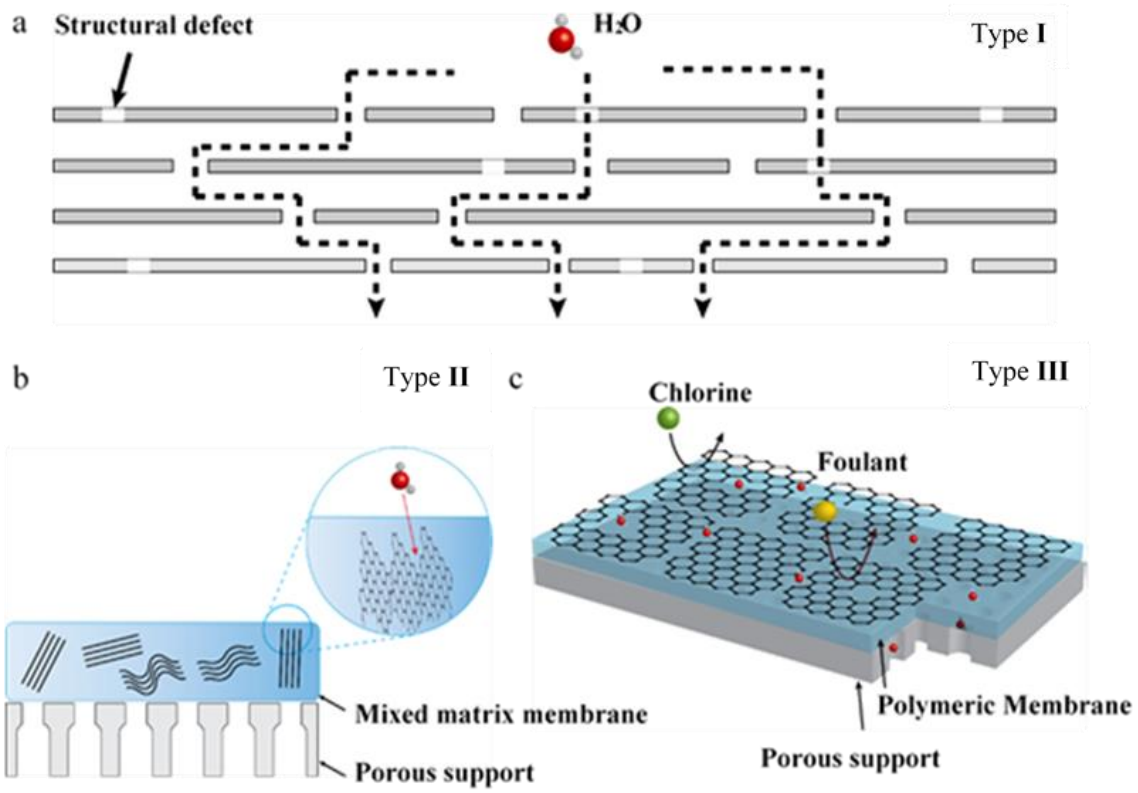

Figure 1.4. Three representative membrane structures with incorporated GO flakes: (a) GO-based membranes with lamellar structure; dashed lines indicate transport pathways of water molecules (a water molecule was shown on top of the membrane surface), and white channels within GO flakes (grey slab) are structural defects; (b) mixed matrix membranes (MMM) with GO as the additive; light blue indicates the bulk matrix material, and groups of black lines indicate agglomerates of GO flakes; and (c) GO functional coating on polymeric membrane.

1.4 APPLICATION OF GRAPHENE-BASED MEMBRANES IN NANOFILTRATION

Graphene, the network composed only by sp^2 carbon, shows promise to be backbone for high permeability, high selectivity molecular sieving material.[14,16,25-27] By creating subnanometer-size pores on graphene lattice, this 2D material can work as filer blocking the transport of molecules larger than pore size while keep the permeation of molecules smaller than pores.[28] Other than creating isolated pores, preparing macroscopic graphene with sufficient densities and size controllable pores are essential for practical

applications. Karnik et al.[18] recently reported via gallium ion bombardment and followed with acidic potassium permanganate treatment, controlled, high density, subnanometer diameter pores (average size ~0.4 nm) could be created on the surface of macroscopic single-layer graphene membrane. The primary nucleation of defects through ion bombardment was critical for pore creation. Through diffusion measurements of potassium chloride (0.66 nm) and Allura Red (~1.0 nm), the membrane shown selectivity in the transport of potassium cation over chloride anion upon etching; as the etching progressed (up to 25 min), the membrane gradually lost selectivity between potassium and chloride ions, while still excluding the diffusion of larger dye molecules; the transport of Allura Red increased with further etching and eventually saturated while etching more than 50 min. The diffusion results demonstrated the creation of highly selective pores on single-layer graphene membrane and the permselectivity of pores was tunable by controlling etching time, and the size of those subnanometer pores are in the range for future nanofiltration applications.

Although single-layer graphene show higher selectivity and permeability than current membrane materials, the harsh synthesize conditions, for instance chemical vapor deposition (CVD), have hindered its application in industrial-scale. In contrary, graphene oxide is particular attractive because they are easy to fabricate, mechanically robust and should suitable for practical use. In 2014, Nair and co-workers[20] observed, while soaking in water, the vacuum tight micrometer-thick GO membranes exhibited a sharp cutoff at ~0.9 nm, species with hydrated radius lager than ~0.45 nm were sieved out. Small species, such as K^+, Mg^{2+} and AsO_4^{3-} ions permeated with approximately same speed and shown no dependence on ion charge. Both experiments and MD simulations confirm that small

ions are affinity to GO and prefer to stay in the capillaries of GO laminates, accordingly, the large ionic pressure (> 50 bar) in the capillaries facilitates the ultrafast permeation of ions smaller than 0.45 nm. Similar selective ion transportation was also reported by Zhu's group,[29] a micrometer-thick (< 10 um) free standing GO membrane was demonstrated to separate sodium ions from copper ions due to the strong coordination interaction between heavy-metal ions and oxygen-containing functional groups of GO, furthermore, organic contaminates, such as rhodamine B, because of strong interaction with GO, can be totally blocked by the membrane as well. Inspired by the idea of coordination interaction between GO and heavy-metal ions, Liu et al.[30] fabricated 3D sulfonated reduced graphene oxide (3D-SRGO) aerogel with high Cd (II) adsorption capacity as 234.8 mg/g. Combing with 3D porous structure and sulfonic ($-SO_3H$) groups modified surface, this 3D-SRGO aerogel could provide multi-dimensional adsorption sites for Cd (II) ions, which leads to highly adsorption for Cd (II), consequently, 3D-SRGO aerogel fabricated membrane shown more than 96% removal for Cd (II) ions.

Since reported GO membranes exhibit extraordinary separation property and ultrafast transport for selective ions, graphene oxide show promise to be applied in nanofiltration technologies. Gao et al.[31] reported ultrathin (~22-53 nm thick) graphene membranes possible for nanofiltration (uGNMs). The uGNMs were fabricated by filtration base-refluxing reduced GO (brGO) dispersion on substrates (AAO disks or PVDF membranes), the membrane thickness could be controlled by the amount of brGO loading. Accompanied with pure water flux as high as 21.8 L m^{-2} h^{-1} bar^{-1}, the resulting ultrathin graphene membranes shown > 99% rejection for large organic dyes, such as methyl blue (MB) and direct red 81 (DR), moreover, the uGNMs exhibited moderate retention (~20-

60%) for ion salts as well. Gao and co-workers suggested that, the retention of organic dyes was attributed to the combination effects of size sieving and electrostatic interaction, while Donnan exclusion dominated the salt rejection of the membrane. Instead of preparing flat sheet membranes, graphene oxide has been applied to fabricate hollow fiber membranes as well.[32,33] Li's group[33] reported graphene oxide hollow fiber membranes for nanofiltration. To increase the stability of GO layer, a porous poly (methyl methacrylate) (PMMA) sacrificial layer was introduced before GO coating, the space between hollow fiber support and GO membrane allowing stress-free shrinkage, the defect-free GO hollow fiber membranes were fabricated as removal of the sacrificial layer. Up on UV-light irradiation, pure water permeability of GO hollow fiber membranes with 150 nm thickness was greatly enhanced from 0.07 to 2.8 L m^{-2} h^{-1} bar^{-1}, meanwhile, the membranes still maintained low molecular weight cut off ~250 Da. Except remarkable salt and organic contamination sieving properties of GO based membrane, the selective permeation of organic solvent and water was demonstrated by Lee's group.[34] Comparison to water, the permeance of alcohols, for instance ethanol, 1-propanol and 2-propanol, was about 80 times slower, taking advantage of the permeation difference, through simple liquid filtration, water can be efficiently filtered from water/alcohol binary solutions and produce alcohols with concentration of ~97%.

Despite graphene oxide show lots of advantages as nanofiltration material, the membrane stability in aqueous solutions is one important technical limitation needs to be faced. To avoid the swelling of GO laminates, stable chemical bonds are normally introduced into GO laminates to "lock" interlayer distance.[35-38] In Mi's paper,[36] via a layer-by-layer deposition technique, 1, 3, 5-benzenetricarbonyl trichloride (TMC) was used to

cross-link adjacent GO flakes. The resulting stabilized membrane exhibited extraordinary high water flux ranged between 8 to 27.6 L m^{-2} h^{-1} bar^{-1}. Albeit TMS cross-linked GO membranes did not show high salt rejection (6-46%), they gave a moderate rejection (46-66%) of Methylene blue and high rejection (93-95%) of Rhodamine-WT. Except TMS used by Mi's group, diamine is another type of cross-linkers could be applied to fix GO interlayer distance. Li et al.[35] reported, by using different diamine (DA) cross-linkers, ethylenediamine (EDA), 1,3-propaneddamine (PDA) and m-phenylenediamine (mPDA), the inter-layer spacing of GO membrane was fixed to 0.92, 0.96 and 0.98 nm, respectively. Comparing with ~0.6 nm swelling of pure GO membrane, under wet condition, the expansion of DA locked membranes was only about 0.2 nm, which consequently enhanced their ability to remove low molecular weight and fulvic acid-like NOM. By taking similar idea, Chung and co-workers used EDA to cross-link GO membrane as well, in addition, 60 K hyperbranched polyethylenimine (HPEI) was applied to modify the surface of membrane.[37] The amine modified membrane shown slightly positive charge, and was demonstrated having high water permeation of 5.01 L m^{-2} h^{-1} bar^{-1} and comparable high rejection towards heavy metal ions, such as Mg^{2+}, Pb^{2+}, Ni^{2+},Cd^{2+}, and Zn^{2+}.

Although graphene and graphene oxide based membranes present remarkable nanofiltration properties, water permeance and antifouling abilities still needed to be improved to compete with commercial pressure-driven nanofiltration membranes. Recently, inorganic materials, such as carbon nanotube,[39-42] TiO_2, Ag and other nanoparticles,[43-50] haven been hybridized with GO membranes to improve their nanofiltration performance.

Gao et al. reported a high flux nanofiltration membrane (G-CNTm) by assembling multiwalled carbon nanotubes with reduced graphene oxide. The water flux of resulting hybridized membrane (11.3 L m^{-2} h^{-1} bar^{-1}) was more than two times higher than corresponding pure graphene-based membrane, which can be attributed to the expended inter-layer spacing by carbon nanotubes. Addition to enhanced water permeation, the membrane still keep high rejection for organic contaminations, > 99% for Direct Yellow and > 96% for Methyl Orange. Besides that, G-CNTm also exhibited good rejection for salt ions (83.5% for Na_2SO_4) and excellent antifouling for sodium alginate (SA) and humic acid (HA).[40] Instated of physically assembling carbon nanotube with graphene oxide, Ray's group[42] fabricated a 3D porous membrane by bridging GO and CNTs together with amide bonds, with further peptides modification, the 3D GO hybrid membrane presented antimicrobial and heavy-metal ion retention properties. Ray and co-workers demonstrated PGLa modified membrane not only gave 100% rejection for E. coil, but also shown efficient disinfection abilities. However, glutathione attached 3D membrane can efficiently capture As (III) (98%), As (V) (94%), and Pb (II) (98%) from waste water.

Besides carbon nanotube, inorganic nanoparticles, such as TiO_2 and Ag, hybridized GO membranes present interesting properties as well. Fu et al.[45] reported that by assembling TiO_2 nanoparticles with GO, a membrane with average pore size ~3.5 nm can be fabricated. The final hybrid GO membrane shown relative high water flux (7 L m^{-2} h^{-1} bar^{-1}) and 100% rejection of methyl orange. Crumpled graphene oxide nanocomposites were reported by Fortner's group,[47] upon assembling these nanocomposites, the resulting membranes achieved extraordinarily high water flux of 246 m^{-2} h^{-1} bar^{-1}. Moreover, the function of the membranes was tunable with encapsulating different nanoparticles into GO.

GO-TiO_2 nanocomposite based membrane not only presented >80% rejection of bovine serum albumin and ~30% rejection of methyl orange, but also demonstrated in situ photocatalytic degradation ability for MO. GO-Ag nanocomposite based membrane, however, exhibited superior antimicrobial properties.

Except directly using as membrane material, due to its high hydrophilicity and antifouling property, GO have also been blended into polymer matrix to improve the host polymer nanofiltration properties. [51-56] By first time directly involving GO flakes into interfacial polymerization, Lee et al.[57] reported the fabrication of novel GO/PA membranes. Unlike physical blend GO with polymer, during the polymerization process, GO flakes can be cross-linked with 1, 3, 5-benzenetricarbonyl trichloride via the formation of ester bonds. Up on GO loading from 0.0 to 0.3%, the hydrophilicity and zeta potential of membrane increased and surface roughness decreased. While maintaining high salt retention, the pure water flux of GO/PA membranes was greatly enhanced to 22 L m^{-2} h^{-1}, and presented excellent antifouling properties for bovine albumin and humic acid.

1.5 APPLICATION OF GRAPHENE-BASED MEMBRANES IN REVERSE OSMOSIS SEPARATIONS

In recent years, reverse osmosis (RO) has become one of the most popular desalination technologies. Although based on similar separation mechanism, RO membranes exhibit higher efficiency in excluding small species, such as Na^+ and K^+ ions, than the nanofiltration correspondents. Unlike applied directly as nanofiltration material, graphene oxide normally work as nanocomposite and surface modification material to improve performance for commonly used RO membranes, for instance, to increase water permeation, enhance antifouling abilities and chlorine resistance.

Due to the high water permeability and extraordinary salt rejection, polyamide (PA) and cellulose based (CA) RO membranes have been commercialized for more than 30 years. Although investments on improving the performances of PA and CA membranes have never been stopped, it still needs improvements on their permselectivity, anti-biofouling abilities, and resistance for chlorine. Park and co-workers reported the fabrication of n/ovel thin-film composite (TFC) membranes by introducing GO into the m-phenylenediamine (MPD)/trimesoyl chloride (TMC) PA polymerization process[58]. The hydrophilicity of the resulting membranes (GO-TFC) was improved with the incensement of GO loading, while surface roughness and the Zeta potential was declined. Without loss high salt rejection. The water flux of the 38-GO-TFC (38 ppm GO content) membrane (~16.6 LMH) was about 80% higher than bear TFC membrane. The anti-biofouling property of GO-TFC membranes was evaluated by a cell attachment test, attributed to the smooth, negatively charged, and more hydrophilic surface, the membrane antifouling performance was improved by 98%. Because of the hydrogen boding between embedded GO and PA, the salt rejection of GO-TFC was retained even at 48,000 ppm h chlorination. Inspired by similar idea, Vatanpour's group embedding reduced GO/TiO_2 nanocomposites into MPD/TMC PA polymer matrix[59]. The rGO/TiO_2/RO membranes exhibited 51.3 LMH waster flux and 99.45% salt rejection as rGO/TiO_2 loaded in 0.02 wt%. With incorporation of rGO/TiO_2, the anti-biofouling ability of final rGO/TiO_2/RO membranes was great improved, and salt rejection only dropped 3% upon chlorination.

Instead of embedding into polymeric matrix, to enhance surface-based interaction (bio-fouling), graphene oxide also work as surface modification material for RO membranes. [[60]][61] Elimelech et al.[62] demonstrated, by reacting with 1-ethyl-3-[3-

(dimethylamino)propyl] carbodiimide (EDC) and N-hydroxysuccinimide (NHS), then cross linked with ethylenediamine, graphene oxide can be reversibly bonded to PA/RO membrane surface (78.6% coverage). GO surface modification exhibited no detrimental effect to intrinsic PA/RO membrane transport properties, however anti-biofouling performance of resulting membranes was enhanced by reducing about 65% of E. *coli*.

To improve both fouling and chloride resistance of PA membranes, Lee's group alternatively deposited oppositely charged GO (aminated GO and regular GO) sheets on the surface of PA membrane through LBL method[63]. GO multilayers could pack tightly on PA surface through electrostatic interaction. Ten GO bilayer (GO_{10}) coated PA membrane shown lower surface roughness and improved hydrophilicity than neat PA membrane. It was shown that membrane performance was remain unchanged after GO coating, however, the water flux of GO_{10}-coated PA membrane reduced only 15% after 12 h filtration of BSA (100 mg/L) solution and NaCl rejection dropped by only ~3%, which represent highly anti-biofouling and chloride resistance improvements for PA based RO membrane after GO coating.

Using same method as Elimelech's group to bond GO to the surface of PA membrane, Jun and co-workers sequentially deposited Au nanostars (AuNS) and polyethylene glycol (PEG) to fabricate a novel PA-GO-AuNS-PEG membrane. The resulting PA-GO-AuNS-PEG membrane not only approximately retained PA membrane performance, but also reduced fouling from mineral ($CaCO_3$ and $CaSO_4$), organic (humic acid) and bacteria (E. *coli*). The multi-antifouling properties mechanism of this PA-GO-AuNS-PEG membrane was also investigated by Jun's group[64]. They suggested that, the neutral surface charge and the existence of Au particles prevented the nucleation of Ca^{2+}

salts, consequently the mineral scaling of the membrane was improved. Moreover, attributed to the hydrophilic and uncharged surface properties and AuNS's ability to prevent organic matter accumulation, the PA-GO-AuNS-PEG membrane exhibited good anti-organic fouling ability.

1.6 APPLICATION OF GRAPHENE-BASED MEMBRANES IN FORWARD OSMOSIS SEPARATIONS

As a low energy consumption process (no hydraulic pressure needed), forward osmosis (FO) has attracted great attention for the past decade as an alternate separation method for conventional pressure-driven technics. To date, commonly commercialized FO membranes can be categorized into cellulose based membranes and thin film composite (TFC) membranes. Besides water flux, rejection, antifouling, and other factors that normally considered to be improved in NF and RO membranes, the membrane support selection is also important for FO membrane performance, because the internal concentration polarization (ICP) could significantly reduce membrane flux and aggravate fouling.

Zhang et al. [65]reported the fabrication of ultrathin (100 nm) rGO freestanding FO membranes which totally overcome the ICP effects brought by FO membrane support. In this novel membrane fabrication strategy, HI steam worked as reducing agent for GO membrane, which also triggered the peeling of reduced GO membrane from cellulose eater substrate as immersing into water. The resulting rGO freestanding membrane shown high mechanical robust, which makes it suitable for FO application. The water flux of 100 nm rGO freestanding FO membrane reached 57.0 LMH while using water as feed and NaCl (2.0 M) as draw solution. The water flux of rGO freestanding membrane exhibit linear

incensement to draw solution concentration (0.5-2.0 M), this indicated the ICP effects was almost eliminated in the membrane. After 12 h FO operation, the reverse NaCl flux was measured to 1.3 g m^{-2} h^{-1}. The rGO freestanding FO membrane also presented high rejection for NaCl, acid orange7 and Cu^{2+} ion. Using poly(acrylonitrile) as support, Mi's group prepared GO based FO membranes through LBL assembly of GO with poly(allylamine hydrochloride) (PAH) via electrostatic interaction[66]. GO/PAH bilayer was around 16.5 nm thick and dominated by GO. The resulting 10-bilayer GO membrane had water flux 3-4 times higher than commercial HTI membrane. Although reverse flux for ionic species (3.3 mol m^{-2} s^{-1}) of the membrane was not low enough, the rejection of sucrose for 10-bilayer GO membrane was round 99%, therefore, the present GO membrane was suitable for FO separation while using sucrose as drawing solution.

Similar to the application in NF and OF, graphene oxide can also work as surface modifier to improve the water permeability, reverse flow and anti-fouling ability of FO membranes. Ginic-Markovic and co-workers two methods to attach GO on the surface of thin film composite (TFC) polyamide FO membranes through poly L-Lysine (PLL)[67], one using layer-by-layer strategy (LBL), the other using hybrid (H) grafting strategy. After GO/PLL surface modification, the water flux maintained the same as neat PA membrane. The reverse flow (2 M NaCl draw solution) of GO/PLL-H membrane was dramatically declined by 63%, however, reverse flow of GO/PLL-LBL membrane was increased 78%, which suggested hybrid grafting of GO was a better way to improve PA based FO membranes. The resulting GO/PLL-H membrane also exhibited high antibacterial activities.

Except modify FO membranes directly, Graphene oxide also combined with other nanoparticles to improve membrane performance. Rahaman's group recently reported GO/AgNPs decorated thin film composite (TFC) polyamide FO membranes with significant anti-biofouling ability (>95%)[68]. Graphene oxide flakes worked as support for anti-bacterial Ag nanoparticles, the GO/AgNPs composite was then drafted on the PA surface by cysteamine through amide bonds. While retaining the membrane transport properties, the resulting GO/Ag/PA membrane exhibited > 95% bacterial inactivetion for E. *coli*. Similar GO/Ag/PA membranes were prepared by Asadishad and co-workers[69]. Rather than synthesize GO/Ag composite first, Asadishad's group did silver decoration in situ on the top of GO modified PA membrane. The resulting GO/Ag/PA membrane shown improved bacterial inactivation for E. *coli*.D21f2, E. *coli*.O157:H7 and Enterococcus faecalis. Moreover, after 7 days of sliver releasing, surface Ag particles could be regenerated by the same way. After sliver regeneration, membrane could retain its antibacterial properties and 75% of its initial sliver loading.

1.7 THESIS SCOPE

Owing to its atomically-thin thickness, favorable 2-D morphology and the sub-nanometer interlayer channels which provide pathways for size-dependent molecular sieving and frictionless water permeation, graphene oxide is emerging as a new-generation membrane material for high-flux, high-selectivity water purification. While numerous attempts have been made to fabricate ultrathin (< 100 nm) GO-based membranes for water treatment recently, only relatively thick membranes exhibit reliable and precise sieving performance so far. Therefore, the targets of my dissertation are: 1) find the factor might impede the development of ultrathin GO membranes with both high permeation rate and excellent

selectivity; 2) by addressing this problem, find a way to prepare ultrathin GO-based membrane for nanofiltration; 3) develop a methodology to fabricate membrane with only one carbon atomic thickness --- single-layer GO membrane.

REFERENCE

(1) Shannon, M. A.; Bohn, P. W.; Elimelech, M.; Georgiadis, J. G.; Marinas, B. J.; Mayes, A. M. *Nature* **2008**, *452*, 301.

(2) Elimelech, M. *Journal of Water Supply Research and Technology-Aqua* **2006**, *55*, 3.

(3) Basile, T.; Petrella, A.; Petrella, M.; Boghetich, G.; Petruzzelli, V.; Colasuonno, S.; Petruzzelli, D. *Industrial & Engineering Chemistry Research* **2011**, *50*, 8389.

(4) Comerton, A. M.; Andrews, R. C.; Bagley, D. M.; Hao, C. Y. *J Membrane Sci* **2008**, *313*, 323.

(5) Kimura, K.; Toshima, S.; Amy, G.; Watanabe, Y. *J Membrane Sci* **2004**, *245*, 71.

(6) Geim, A. K.; Novoselov, K. S. *Nature Materials* **2007**, *6*, 183.

(7) Geim, A. K. *Science* **2009**, *324*, 1530.

(8) Dreyer, D. R.; Park, S.; Bielawski, C. W.; Ruoff, R. S. *Chem. Soc. Rev.* **2010**, *39*, 228.

(9) Huang, H. B.; Ying, Y. L.; Peng, X. S. *Journal of Materials Chemistry A* **2014**, *2*, 13772.

(10) Hummers, W. S.; Offeman, R. E. *J. Am. Chem. Soc.* **1958**, *80*, 1339.

(11) Lomeda, J. R.; Doyle, C. D.; Kosynkin, D. V.; Hwang, W. F.; Tour, J. M. *J. Am. Chem. Soc.* **2008**, *130*, 16201.

(12) Xu, Q.; Xu, H.; Chen, J. R.; Lv, Y. Z.; Dong, C. B.; Sreeprasad, T. S. *Inorg. Chem. Front.* **2015**, *2*, 417.

(13) Hegab, H. M.; Zou, L. D. *J. Membrane Sci.* **2015**, *484*, 95.

(14) Cohen-Tanugi, D.; Grossman, J. C. *Nano Lett.* **2012**, *12*, 3602.

(15) Lin, L. C.; Grossman, J. C. *Nat. Commun.* **2015**, *6*.

(16) Konatham, D.; Yu, J.; Ho, T. A.; Striolo, A. *Langmuir* **2013**, *29*, 11884.

(17) Surwade, S. P.; Smirnov, S. N.; Vlassiouk, I. V.; Unocic, R. R.; Veith, G. M.; Dai, S.; Mahurin, S. M. *Nature Nanotechnology* **2015**, *10*, 459.

(18) O'Hern, S. C.; Boutilier, M. S. H.; Idrobo, J. C.; Song, Y.; Kong, J.; Laoui, T.; Atieh, M.; Karnik, R. *Nano Lett.* **2014**, *14*, 1234.

(19) Nair, R. R.; Wu, H. A.; Jayaram, P. N.; Grigorieva, I. V.; Geim, A. K. *Science* **2012**, *335*, 442.

(20) Joshi, R. K.; Carbone, P.; Wang, F. C.; Kravets, V. G.; Su, Y.; Grigorieva, I. V.; Wu, H. A.; Geim, A. K.; Nair, R. R. *Science* **2014**, *343*, 752.

(21) Wei, N.; Peng, X. S.; Xu, Z. P. *Acs Appl. Mater. Inter.* **2014**, *6*, 5877.

(22) Li, H.; Song, Z. N.; Zhang, X. J.; Huang, Y.; Li, S. G.; Mao, Y. T.; Ploehn, H. J.; Bao, Y.; Yu, M. *Science* **2013**, *342*, 95.

(23) Qu, X. L.; Alvarez, P. J. J.; Li, Q. L. *Water Res.* **2013**, *47*, 3931.

(24) Mahmoud, K. A.; Mansoor, B.; Mansour, A.; Khraisheh, M. *Desalination* **2015**, *356*, 208.

(25) Zhao, S. J.; Xue, J. M.; Kang, W. *J. Chem. Phys.* **2013**, *139*.

(26) Jiang, D. E.; Cooper, V. R.; Dai, S. *Nano Lett.* **2009**, *9*, 4019.

(27) Du, H. L.; Li, J. Y.; Zhang, J.; Su, G.; Li, X. Y.; Zhao, Y. L. *Journal of Physical Chemistry C* **2011**, *115*, 23261.

(28) Bunch, J. S.; Verbridge, S. S.; Alden, J. S.; van der Zande, A. M.; Parpia, J. M.; Craighead, H. G.; McEuen, P. L. *Nano Lett.* **2008**, *8*, 2458.

(29) Sun, P. Z.; Zhu, M.; Wang, K. L.; Zhong, M. L.; Wei, J. Q.; Wu, D. H.; Xu, Z. P.; Zhu, H. W. *Acs Nano* **2013**, *7*, 428.

(30) Wu, S. B.; Zhang, K. S.; Wang, X. L.; Jia, Y.; Sun, B.; Luo, T.; Meng, F. L.; Jin, Z.; Lin, D. Y.; Shen, W.; Kong, L. T.; Liu, J. H. *Chem. Eng. J.* **2015**, *262*, 1292.

(31) Han, Y.; Xu, Z.; Gao, C. *Adv. Funct. Mater.* **2013**, *23*, 3693.

(32) Goh, K.; Setiawan, L.; Wei, L.; Si, R.; Fane, A. G.; Wang, R.; Chen, Y. *J Membrane Sci* **2015**, *474*, 244.

(33) Chong, J. Y.; Aba, N. F. D.; Wang, B.; Mattevi, C.; Li, K. *Scientific Reports* **2015**, *5*.

(34) Liu, R.; Arabale, G.; Kim, J.; Sun, K.; Lee, Y.; Ryu, C.; Lee, C. *Carbon* **2014**, *77*, 933.

(35) Xia, S. J.; Ni, M.; Zhu, T. R.; Zhao, Y.; Li, N. N. *Desalination* **2015**, *371*, 78.

(36) Hu, M.; Mi, B. X. *Environmental Science & Technology* **2013**, *47*, 3715.

(37) Zhang, Y.; Zhang, S.; Chung, T. S. *Environmental Science & Technology* **2015**, *49*, 10235.

(38) Mishra, A. K.; Ramaprabhu, S. *Desalination* **2011**, *282*, 39.

(39) Chen, X. F.; Qiu, M. H.; Ding, H.; Fu, K. Y.; Fan, Y. Q. *Nanoscale* **2016**, *8*, 5696.

(40) Han, Y.; Jiang, Y. Q.; Gao, C. *Acs Applied Materials & Interfaces* **2015**, *7*, 8147.

(41) Liu, H. Y.; Zhang, G. Q.; Zhao, C. Q.; Liu, J. D.; Yang, F. L. *Journal of Materials Chemistry A* **2015**, *3*, 20277.

(42) Nellore, B. P. V.; Kanchanapally, R.; Pedraza, F.; Sinha, S. S.; Pramanik, A.; Hamme, A. T.; Arslan, Z.; Sardar, D.; Ray, P. C. *Acs Applied Materials & Interfaces* **2015**, *7*, 19210.

(43) Safarpour, M.; Khataee, A.; Vatanpour, V. *Sep. Purif. Technol.* **2015**, *140*, 32.

(44) Safarpour, M.; Vatanpour, V.; Khataee, A.; Esmaeili, M. *Sep. Purif. Technol.* **2015**, *154*, 96.

(45) Xu, C.; Cui, A. J.; Xu, Y. L.; Fu, X. Z. *Carbon* **2013**, *62*, 465.

(46) Filice, S.; D'Angelo, D.; Libertino, S.; Nicotera, I.; Kosma, V.; Privitera, V.; Scalese, S. *Carbon* **2015**, *82*, 489.

(47) Jiang, Y.; Wang, W. N.; Liu, D.; Nie, Y.; Li, W. L.; Wu, J. W.; Zhang, F. Z.; Biswas, P.; Fortner, J. D. *Environmental Science & Technology* **2015**, *49*, 6846.

(48) Cui, J. H.; Liu, Y. L. *Rsc Advances* **2015**, *5*, 85748.

(49) Jiang, Y.; Liu, D.; Cho, M. J.; Lee, S. S.; Zhang, F. Z.; Biswas, P.; Fortner, J. D. *Environmental Science & Technology* **2016**, *50*, 2514.

(50) Vatanpour, V.; Shockravi, A.; Zarrabi, H.; Nikjavan, Z.; Javadi, A. *Journal of Industrial and Engineering Chemistry* **2015**, *30*, 342.

(51) Yeh, T.-M.; Wang, Z.; Mahajan, D.; Hsiao, B. S.; Chu, B. *Journal of Materials Chemistry A* **2013**, *1*, 12998.

(52) Suhas, D. P.; Raghu, A. V.; Jeong, H. M.; Aminabhavi, T. M. *Rsc Advances* **2013**, *3*, 17120.

(53) Wang, N.; Ji, S.; Zhang, G.; Li, J.; Wang, L. *Chem. Eng. J.* **2012**, *213*, 318.

(54) Wang, N.; Ji, S.; Li, J.; Zhang, R.; Zhang, G. *J Membrane Sci* **2014**, *455*, 113.

(55) Lee, J.; Chae, H.-R.; Won, Y. J.; Lee, K.; Lee, C.-H.; Lee, H. H.; Kim, I.-C.; Lee, J.-m. *J Membrane Sci* **2013**, *448*, 223.

(56) Wang, L.; Wang, N.; Li, J.; Li, J.; Bian, W.; Ji, S. *Sep. Purif. Technol.* **2016**, *160*, 123.

(57) Bano, S.; Mahmood, A.; Kim, S.-J.; Lee, K.-H. *Journal of Materials Chemistry A* **2015**, *3*, 2065.

(58) Chae, H. R.; Lee, J.; Lee, C. H.; Kim, I. C.; Park, P. K. *J Membrane Sci* **2015**, *483*, 128.

(59) Safarpour, M.; Khataee, A.; Vatanpour, V. *J Membrane Sci* **2015**, *489*, 43.

(60) Kim, S. G.; Hyeon, D. H.; Chun, J. H.; Chun, B. H.; Kim, S. H. *Desalination and Water Treatment* **2013**, *51*, 6338.

(61) Hegab, H. M.; Wimalasiri, Y.; Ginic-Markovic, M.; Zou, L. *Desalination* **2015**, *365*, 99.

(62) Perreault, F.; Tousley, M. E.; Elimelech, M. *Environmental Science & Technology Letters* **2014**, *1*, 71.

(63) Choi, W.; Choi, J.; Bang, J.; Lee, J. H. *Acs Applied Materials & Interfaces* **2013**, *5*, 12510.

(64) Ray, J. R.; Tadepalli, S.; Nergiz, S. Z.; Liu, K. K.; You, L.; Tang, Y. J.; Singamaneni, S.; Jun, Y. S. *Acs Applied Materials & Interfaces* **2015**, *7*, 11117.

(65) Liu, H. Y.; Wang, H. T.; Zhang, X. W. *Adv. Mater.* **2015**, *27*, 249.

(66) Hu, M.; Mi, B. X. *J Membrane Sci* **2014**, *469*, 80.

(67) Hegab, H. M.; ElMekawy, A.; Barclay, T. G.; Michelmore, A.; Zou, L. D.; Saint, C. P.; Ginic-Markovic, M. *Acs Applied Materials & Interfaces* **2015**, *7*, 18004.

(68) Soroush, A.; Ma, W.; Silvino, Y.; Rahaman, M. S. *Environmental Science-Nano* **2015**, *2*, 395.

(69) Soroush, A.; Ma, W.; Cyr, M.; Rahaman, M. S.; Asadishad, B.; Tufenkji, N. *Environmental Science & Technology Letters* **2016**, *3*, 13.

CHAPTER 2

SELF-ASSEMBLY: A FACILE WAY OF FORMING ULTRATHIN, HIGH PERFORMANCE GRAPHENE OXIDE MEMBRANES FOR WATER PURIFICATION [1]

2.1 ABSTRACT

Single-layer graphene oxide (SLGO) is emerging as a new-generation membrane material for high-flux, high-selectivity water purification, owing to its favorable 2-D morphology that allows facile fabrication of ultrathin membranes with sub-nanometer interlayer channels. However, reliable and precise molecular sieving performance still necessarily depends on thick graphene oxide (GO) deposition which usually leads to low water flux. This trade-off between selectivity and flux significantly impedes the development of ultrathin GO membranes. In this work, we demonstrate that the selectivity/flux trade-off can be broken by self-assembly of SLGO via simple deposition rate control. We find GO membranes, prepared by slow deposition of SLGO flakes, exhibit considerably improved salt rejection, while counterintuitively having 2.5~4 times higher water flux than that of membranes prepared by fast deposition. This finding has extensive implications of designing/tuning interlayer nanostructure of ultrathin GO membranes by simply controlling SLGO deposition rate, and thus may greatly facilitate their development for high flux, high selectivity water purification

1：Reprinted with permission from Xu, W. W. L.; Fang, C.; Zhou, F. L.; Song, Z. N.; Liu, Q. L.; Qiao, R.; Yu, M. *Nano Lett* **2017**, *17*, 2928. Copy right 2017 American Chemical Society. (Appendix A)

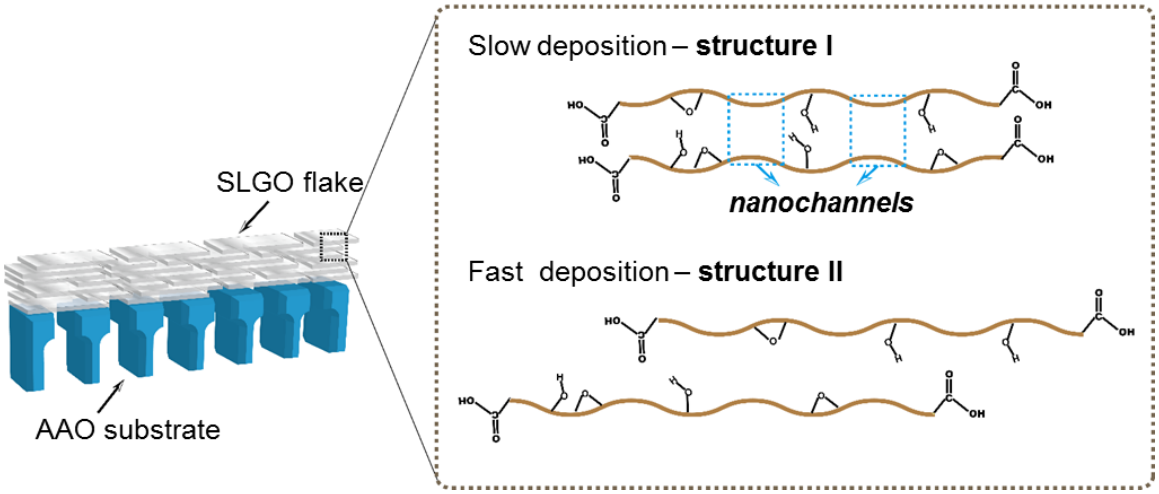

Figure 2.1 Proposed conceptual interlayer nanostructures of GO membranes prepared by slow and fast deposition rates. When prepared at slow deposition rate, oxygen-containing groups on adjacent SLGO flakes prefer to self-assemble with each other to form thermodynamically favored interlayer structure; In contrast, at fast deposition rate, oxygen-containing groups may arrange in a more random fashion.

2.2 INTRODUCTION

Recently, single-layer graphene oxide (SLGO) has attracted increasing attention as a new membrane material due to its atomically-thin thickness, two-dimensional (2-D) structure, and high chemical stability.[1-6] Owing to the large number of oxygen-containing functionalization groups, SLGO can be easily dispersed in water. Consequently, solution-based coating processes, such as vacuum filtration, have been applied to fabricate graphene oxide (GO) membranes with lamellar structure and sub-nanometer interlayer nanochannels.[7,8] Previous studies have illustrated that the 2-D nanochannels between adjacent SLGO flakes can provide pathways for size-dependent molecular sieving and frictionless water permeation.[7,9-11] Encouraged by these exciting experimental results,

many following studies have focused on exploring the water purification potential of GO membranes with lamellar structure.[12-20] While numerous attempts have been made to fabricate ultrathin (<100 nm) SLGO-based membranes for water treatment recently,[12,13,20] only relatively thick membranes exhibit reliable and precise sieving performance so far.[7,9,10,16]

Fundamentally, the permeation characteristics of a GO membrane with lamellar structure are expected to be mainly governed by the interlayer nanostructure formed between neighboring SLGOs. Different from graphene, SLGO features abundant oxygen-containing surface functional groups. Therefore, the interlayer nanostructure of SLGO-based membranes depends on how the surface functional groups of adjacent SLGO layers are arranged. So far, no study, however, has been conducted to understand the interlayer nanostructure and its influence on water purification performance. To develop ultrathin membranes with both high permeation rate and excellent selectivity, it is essential to understand process-structure-performance relationship of SLGO-based membranes, i.e., how membrane fabrication conditions control the membrane interlayer nanostructures and how interlayer nanostructures in turn determine the permeation characteristics.

In this study, we explore the process-structure-performance relationship of GO membranes prepared by vacuum filtration. Here, we purposely deposited SLGO at a fast rate and at a rate ~12 times slower to control the interlayer nanostructure of the resulting membranes. We find, while maintaining the same SLGO loading per unit area, the slowly deposited GO membranes show greatly enhanced water permeation rate. We propose that, at slow deposition rate, SLGO flakes better self-assemble to approach the thermodynamically favored interlayer structure with functionalized patches on neighboring

GO layers facing each other and pristine graphene patches on adjacent GO layers forming fast water transport channels (type I structure, Figure 2.1). At fast deposition rate, relatively random packing of SLGOs is locked into less favorable interlayer structures with significant mismatches between functionalized and pristine patches on neighboring GO layers (type II structure, Figure 2.1), leading to drastically retarded water permeation. The different molecular details of these interlayer structures and their effect on water transport were corroborated by X-ray diffraction (XRD), organic vapor permeation, atomic force microscopy (AFM), and molecular dynamics (MD) simulations. Moreover, GO membrane as thin as 4.7 nm and with the favorable interlayer nanostructure exhibits considerably improved salt rejection. This study, for the first time, clarifies the process-structure-performance of GO membranes, and the insight gained here can be utilized to guide new designs of ultrathin GO membranes for high-flux, high selectivity water purification.

2.3 EXPERIMENTAL

Graphene oxide synthesis

Graphene oxide (GO) was synthesized by Hummers method.[21] All chemicals were purchased from Sigma-Aldrich or VWR and used without further purification. Concentrated H_2SO_4 (69 mL) was slowly added into the mixture of graphite flakes (3.0 g, 1 equv.) and $NaNO_3$ (1.5 g, 0.5 equv.), and the mixture was cooled down to 0 ℃ in an ice bath. $KMnO_4$ (9.0 g, 3.0 equv.) was added into the reaction mixture slowly to keep the mixture at a low temperature. The mixture was warmed up to 35 ℃ and kept stirring for 30 min. Then 138 mL water was added into the reaction mixture, which produced large amount of heat and brought reaction temperature to 98 ℃. Maintained the reaction temperature at 98 ℃ for 2 h and then slowly cooled it down with water bath. Additional

420 mL water and 3 mL of H_2O_2 (30%) was added into the mixture, and the black solid was collected by filtration after the mixture cooled down to r.t. The final product was washed with 200 mL of water, 200 mL of 1N HCl and 200 mL of ethanol for two times, and then dried under vacuum.

Dispersion (1mg/mL) of as-prepared GO was sonicated for 1 hour and followed by centrifugation at 10,000 rpm for 30 min. The supernatant was collected and the sediment was re-dispersed in water, repeated this procedure for several times and collected all the supernatant. Single-layer graphene oxide was obtained by drying supernatant under vacuum

Characterizations of GO

The as-synthesized GO was characterized by Raman spectroscopy, Fourier transform infrared (FTIR), atomic force microscopy (AFM), X-ray photoelectron spectroscopy (XPS), and 77 K N_2 adsorption/desorption.

Raman spectra were recorded with a J Y Horiba LabRam system using a 632 nm excitation laser. According to Ferrari et al's work,[22] on the low-defect regime of graphene, where the distance between point-like defects ($\boldsymbol{L_D}$) was defined larger than 10 nm, equation $L_D^2(nm^2) = \frac{(4.3\pm1.3)\times10^3}{E_L^4}(\frac{I_D}{I_G})^{-1}$ could be used to correlate the I_D/I_G ratio with $\boldsymbol{L_D}$. By assuming the same dependence of $\boldsymbol{L_D}$ on I_D/I_G for GO, the distance of defects ($\boldsymbol{L_D}$) on our single layer GO was calculated between 12.1 to 16.5 nm, which suggests that our as-prepared GO still keeps high order (less defect).

FTIR spectrum was measured by Nicolet 670 FTIR Spectrometer.

Atomic Force Microscopy (AFM) images were scanned by TT-AFM system purchased from AFM workshop under vibration mode, and analyzed by Gwyddion 2.41.

X-ray Photoelectron Spectroscopy (XPS) was conducted using a Kratos AXIS Ultra DLD XPS system, which was equipped with a monochromatic Al Kα source. The monochromatic Al Kα source was operated at 15 keV and 120 W, and the pass energy was fixed at 40 eV for the detailed scans. The binding energy was calibrated using an Ag foil with $Ag3d_{5/2}$ set at 368.21 ± 0.025 eV for the monochromatic Al X-ray source.

N_2 Adsorption and Desorption Isotherm.

To estimate the BET surface area of GO, 77 K N_2 adsorption/desorption on GO was measured using Micromeritics ASAP 2020 instrument. Before isotherm measurement, GO sample was pre-treated at 60 ℃ for 12 h in the vacuum to make sure all the water was removed. The surface area of GO was estimated to be 670 m^2/g.

Fabrication and characterization of GO membranes

The SLGO dispersion was prepared by dispersing certain amount of SLGO in 25 mL or 250 mL DI water, followed by 10 min sonication. The membrane was deposited through a simple vacuum filtration process on a commercial available anodized aluminum oxide (AAO) substrate which has an effective area of 10.5 cm^2. During the membrane preparation process, the vacuum degree was fixed at 0.07 MPa. To fabricate membranes with different thickness, a series of SLGO dispersion were prepared with SLGO loading ranging from 7.4 to 184.4 mg/m^2. For instance, to deposit 118 nm thick SLGO on the area

of 10.5 cm^2 AAO substrate at slow rate, 250 mL SLGO dispersion with concentration of 0.88 μg/mL was filtered through AAO. Based on the same idea, to prepare 118 nm GO membrane at fast deposition rate, 25 mL SLGO dispersion with concentration of 8.8 μg/mL was used. The average thickness of our maximum GO loading was measured to be 118 ± 5.2 nm and confirmed by SEM. The thickness of membrane with less SLGO loading was estimated as 23.6 and 4.7 nm, respectively, by assuming thickness is proportional to the amount of SLGO. All the membranes were dried in the vacuum at r.t for 12 hours before use and characterization. The reduced GO (rGO) membranes were prepared by reducing corresponding GO membranes in vacuum at 220 ℃ for 12 hours. To study the structure difference between fast and slow deposited membranes, 118 nm thick GO/ membranes and corresponding rGO membranes were subjected to XRD analysis.

The actual SLGO concentration in water was measured by Total Organic Carbon (TOC) analysis. The concentration of SLGO stock solution was ~13.6 mg/L.

The thickness of membrane with maximum SLGO loading (184.4 mg/m^2) was confirmed by the cross-section SEM image. SEM images were taken by using a Zeiss ultraplus thermal field emission scanning electron microscope and without gold coating.

Since 4.7 nm and 23.6 nm membranes were too thin to give detectable X-ray diffraction signal, we only did XRD analysis on 118.4 nm GO and rGO membranes to study the structure difference induced by deposition rate. The XRD experiments were performed on a Rigaku D/Max 2100 Powder X-ray Diffractometer (Cu Kα radiation), and the experiments were run by using a zero background slide on which the GO membrane

was gently pressed. Data were collected at increments of 0.02 degrees, and an exposure time of 1.2 s/step in the angular range of 5-35 degree 2-theta at ambient temperature.

Measurement of pure water flux

Pure water flux of GO membranes was measured on a dead end system purchased from Sterlitech and driven by pressurized N_2 gas. The permeation area was 19.6 mm^2, and the chosen sample was fixed at the bottom of the water tank. The driving pressure drop for 4.7 and 23.6 nm GO membranes was fixed at 5 bar; for 118 nm GO membrane, the applied pressure drop was adjusted to 10 bar. The water flux was obtained by measuring the mass of water collected with permeation time for at least 48 h under a specific pressure drop. Steady state water flux was reported after permeation reached steady state for at least 2h. For GO membranes with different thickness, three repeat water flux tests were performed, and average pure water flux of 4.7, 23.6, 118 nm GO membranes prepared at fast and slow deposition rates were summarized in Table 2.6; s.e.m error bars (standard error = standard deviation/$\sqrt{n}$) were applied to all the data points.

Organic vapor permeation measurements

The vapor permeation experiments of two chosen organic molecules, hexane and 2,2-dimethylbutane (DMB), with different molecular diameters were set up to investigate the effect of deposition rate on the effective pore size of GO and corresponding rGO membranes. The experiment set up was illustrated in Figure 2.9. The membrane was first glued to an aluminum foil which has a hole with a diameter of 3 mm in the center. After the glue was dry overnight, this aluminum foil was used to seal the vial in which chosen organic solvent was added, and then vial was placed into a small chamber and blew with

dry air. The weight loss of the vial was measured at different time interval to study the permeation rate (Figure 2.10). Organic vapor permeance of 118 nm GO/rGO membranes were given in Table 2.4. Vapor permeation results of thinner membrane (4.7 and 23.6 nm) were given in Table 2.5.

Vapor permeation measurements were also applied to the 118 nm GO/rGO membranes, which was deposited at an intermediate rate (0.08 nm/s), to see if intermediate deposition rate will have notable influence on organic permeation performance. The structural characterization for this membrane was shown in Figure 2.11, and the permeation rate for hexane and DMB was shown in Figure 2.12. We found the GO/rGO membranes prepared at intermediate rate exhibit similar d-spacing as fast-deposited sample (GO: 10.6 Å; rGO: 21.66 Å). According to Figure 2.12, the permeances of hexane and DMB through GO membrane prepared at intermediate rate are calculated as 1.92×10^{-9} and 1.04×10^{-9} $mol\cdot m^{-2}\ s^{-1}\ Pa^{-1}$, and the permselectivity of hexane over DMB is ~1.8; after reduction, the permeances of hexane and DMB are 3.3×10^{-9} and 0.83×10^{-9} $mol\cdot m^{-2}\ s^{-1}\ Pa^{-1}$, respectively, and the permselectivity is ~4.

Water adsorption isotherm of GO.

Water adsorption isotherm was employed to study how water molecules adsorb on the GO surface. The room temperature water adsorption isotherm was measured by a homemade system, and the experiment set up was illustrated in Figure 2.13a. GO powder was first degassed at 60 ℃ in vacuum for 12 h to remove adsorbed water, and then 165.6 mg of degassed GO powder was transferred into a sealed chamber with flowing air with different humidity. The relative humidity of the air was controlled by the ratio of the flow

rate of dry air (MFC #1) and water saturated air (MFC #2). Weight change of GO was monitored by a balance in the chamber. At certain humidity, the equilibrium adsorbed amount was determined while a stabilized weight was read from the balance. The isotherm was shown in Figure 2.13b.

AFM topology scan on overlapped GO double-layers under different humidity.

Monitoring the change of interlayer distance *d* and SLGO double-layer surface roughness with different humidity using AFM might provide evidence for the discontinuity of water between SLGO layers and preferential water adsorption on hydrophilic sites.[8] The AFM sample was prepared by drop diluted SLGO suspension on mica substrate and let the sample dried on the substrate through slow evaporation of water under r.t. To simulate the fast membrane fabrication process, corresponding fast deposited AFM sample was prepared by sweeping the sample surface with 70 ℃ hot air. All the samples were further dehydrated under vacuum for 12 h before subjected to AFM scan.

Molecular dynamic (MD) simulation for self-assembly of GO layers

The simulation system consists of two SLGOs immersed in water (Figure 2.15a). The upper and lower SLGOs measure 4×4 nm^2 and 6×6 nm^2, respectively. Each SLGO contains pristine and oxidized strips measuring 1 nm in width. Initially, the oxidized strips of the upper SLGO is offset from those of the lower SLGO by ~0.5 nm. The simulation system is periodical in all three directions.

The oxidized strips of each SLGO contain hydroxyl and epoxide groups on both their sides. The oxidized C atoms were randomly chosen for the C atoms in the oxidized

region to have O/C ratio of 30%-40%. The OPLS-AA[23] force fields were used for the GOs. The rigid SPC/E[23] model was used for the water molecules.

MD simulations were performed on GROMACS package.[24] The LINCS algorithm[25] was applied to constrain all GO bonds. A NVT ensemble with velocity-rescale thermostat[26] at 300 K was implemented. A global cutoff 1.2 nm was used for computing the Lennard-Jones potential and the particle mesh Ewald (PME) method[27] was used to calculate the electrostatic interactions.

Initially, the upper SLGO was placed at a distance of ~2.0 nm from the lower SLGO. The lower SLGO is fixed in the space by constraining the C atoms throughout the simulation. By applying a constant force on all water molecules, a flow was generated to push the upper SLGO toward to the lower SLGO for 2 ns, when the average separation between the two SLGOs is ~0.9 nm. The applied force on the water molecules was then removed and an equilibrium run of 20 ns was performed.

Movie shows the self-assembly process during the 20 ns-long production run. Figure 2.15b shows the histogram of the spacing between the two SLGOs during the last 10 ns of the simulation. The average spacing between the two SLGO is 0.69 nm. This separation is close to what has been reported for two SLGOs separated by a single water layer, in which a PMF minimal is reached at a SLGO separation of 0.7 nm.[28]

Molecular dynamic (MD) simulation for water permeation through self-assembled GO bilayers

Figure 2.16c in the shows a snapshot of the system used for studying the permeation of water through SLGO bilayers. The two SLGOs have the same lateral dimension of 6×6

nm^2, and each features alternating oxidized and pristine regions with a constant width (taken to be 0.3, 0.6, 1.0, and 1.5 nm in different simulations). The oxidized regions of the two SLGOs are either fully aligned (i.e., oxidized regions facing each other and pristine regions facing each other; termed "good assembly" in the main text) or fully offset (termed poor assembly in the main text). The spacing between the two SLGO flakes is 0.69 nm. The system is periodical in all three directions. A large vacuum space was placed between SLGO and their periodical images, and the slab-PME method was used in computing the electrostatic interactions so as to effectively model a 2D system periodical only in the SLGO plane (i.e., *xy*-plane). Molecular models for the GO and water molecules are the same as those used in the self-assembly simulation. All carbon atoms were fixed during the simulation, but the oxygen and hydrogen atoms were allowed to move.

To obtain the system described above, we first determine the right number of water molecules between the two SLGO layers. To this end, we built a system (Figure 2.17) in which the GO layers are connected to two water reservoirs at their two ends. Starting from a configuration in which the space between the two GO layers is empty, equilibrium MD simulations were performed for 10 ns. We found that the number of water molecules between the GO layers reaches a steady state in less than 5 ns. Next, the water reservoirs are removed and the system is made periodical in the *xy*-plane. To drive water transport, a constant acceleration of g_x is applied in the flow direction (*x*-direction), and a non-equilibrium run of 10 ns was performed.

During the non-equilibrium run, the average velocity of water molecules in the flow direction was computed on the fly. The data in the last 5 ns were used to obtain the average velocity of water molecules. The mass flux of water is reported as

$$\frac{J}{J_0} = \frac{\bar{V}_{MD}(g_x)\rho_{MD}}{\bar{V}_{con}(g_x, \rho_{bulk}, d, \mu)\rho_{bulk}} \quad (1)$$

where J is computed from the MD simulation using the average water velocity $\bar{V}_{MD}$ and density (ρ_{MD}) in the SLGO channel. J_0 is the mass flux predicted using continuum fluid mechanics assuming no-slip boundary condition on the channel wall.[28]

$$\bar{V}_{con} = -\frac{1}{12\mu} d^2 \rho_{bulk} g_x \quad (2)$$

where d is the effective channel width, $\mu = 0.729$ mPa · s is the shear viscosity of SPC/E water at 300 K.[29] $\rho_{bulk} = 0.998$ g/cm^3 is the density of bulk SPC/E water at 300 K.[30] We take $d = H - d_c$, where H is the channel width (0.69 nm here), and d_c=0.355 nm is the van der Waals diameter of the carbon atom.

Figure 2.16d shows the water flux for different SLGO configurations when the GO spacing is 0.69 nm. Number of hydrogen bonds between water and SLGOs per water molecule for different strip size in good and poor assembly is shown in Figure 2.18a. We also performed simulations in which the SLGO spacing is fixed to 0.72 nm and the same trend as shown in Fig. 4d was obtained (Figure 2.18b).

Salt rejection.

The influence of nanostructure on the metal ion removal was investigated by salt rejection experiments. Salt rejection experiments were performed on 4.7 nm GO membranes to demonstrate superior ion removal performance of slow-deposited GO membranes. The salt rejection tests were performed on the same dead end system for water flux measurement, and 100 mL of diluted salt solution (KCl, NaCl and $MgSO_4$ with

concentration of 10 mM) was filtered through 4.7 nm GO membranes. Effective membrane area was 19.6 mm^2, and the pressure drop was fixed at 5 bar. After 2 hours of equilibrium, 4 mL of permeance was collected, the conductivity of both permeate and feed were monitored to evaluate the rejection, and three repeat rejection tests were performed for each salt. To further investigate the influence of salt concentration on the rejection performance, NaCl rejection tests with higher concentration (50 and 100 mM) were applied on both fast- and slow-deposited 4.7 nm GO membranes.

2.4 RESULTS AND DISCUSSION

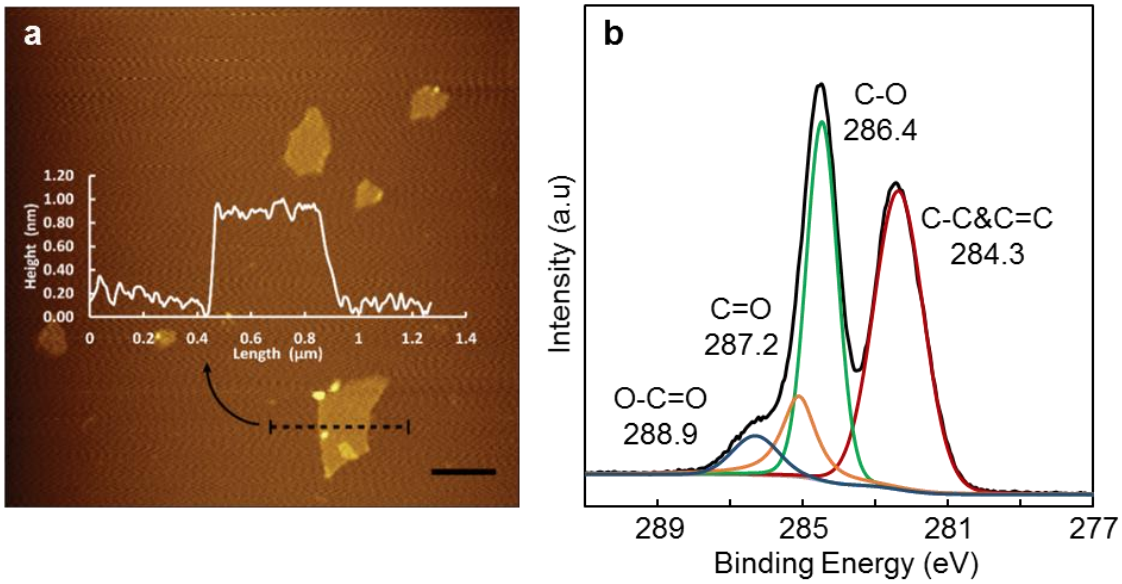

Figure 2.2 Characterization of single layer graphene oxide (SLGO): (a) AFM image of SLGO deposited on a mica substrate; inset shows the height profile of a SLGO flake (scale bar: 500 nm); (b) XPS C_1s spectrum of SLGO.

GO was prepared by Hummers method.[21] After washing, sonication, and centrifugation, the as-synthesized GO show single-layer features with an average thickness of ~0.8 nm and a lateral size of ~500 nm (Figure 2.2a). The Raman spectrum (Figure 2.3) exhibits a G peak at ~1590 cm^{-1} and a D peak at ~1350 cm^{-1}, assigned to the graphitized structure and local defects/disorders, respectively;[31,32] the low I_D/I_G ratio (1.39) suggests high order is still maintained in the graphitized structure of the synthesized GO.[22] Various oxygen-containing groups on SLGO are observed on the Fourier transform infrared (FTIR) spectrum (Figure 2.4). X-ray photoelectron spectroscopy (XPS) was also conducted to explore the chemical environment of carbon atoms in SLGO (Figure 2.2b), which indicates that ~49% of the carbon is non-oxidized, 41% is C-O bonded, and 10% attributes to C=O and COOH bonding. GO membranes were deposited on commercial anodized aluminum oxide (AAO) substrates (~20 nm pore size in the top layer) with an effective area of 10.5 cm^2 through a simple vacuum-filtration process (Figure 2.5a). Thickness of GO membranes was controlled by the amount of SLGO in the suspension (= liquid volume × SLGO concentration in suspension), and the actual SLGO concentration in suspension was measured by a total organic carbon (TOC) analyzer. The membrane thickness with GO loading of 184.4 mg/m^2 was determined from the cross-sectional scanning electron microscopy (SEM) image (Figure 2.5b), which is 118$\pm$ 5.2 nm. Thickness of membranes with lower SLGO loadings was extrapolated by assuming it changes linearly with deposition amount.

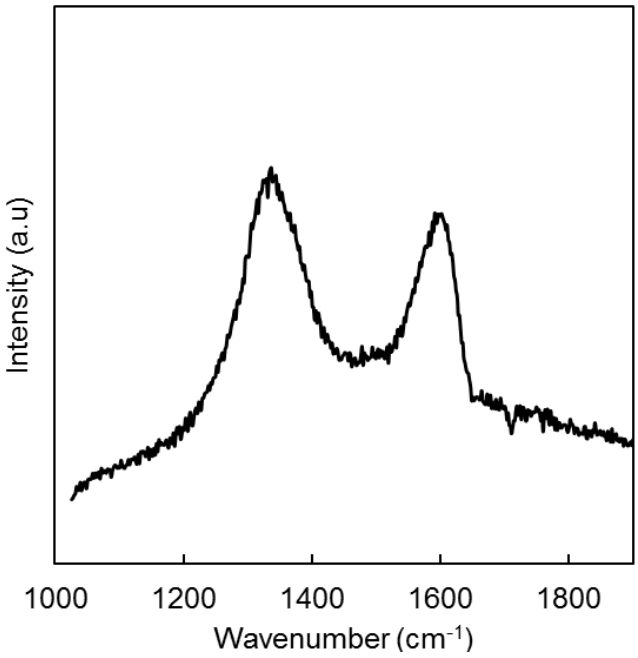

Figure 2.3 Raman spectrum of as-synthesized graphene oxide

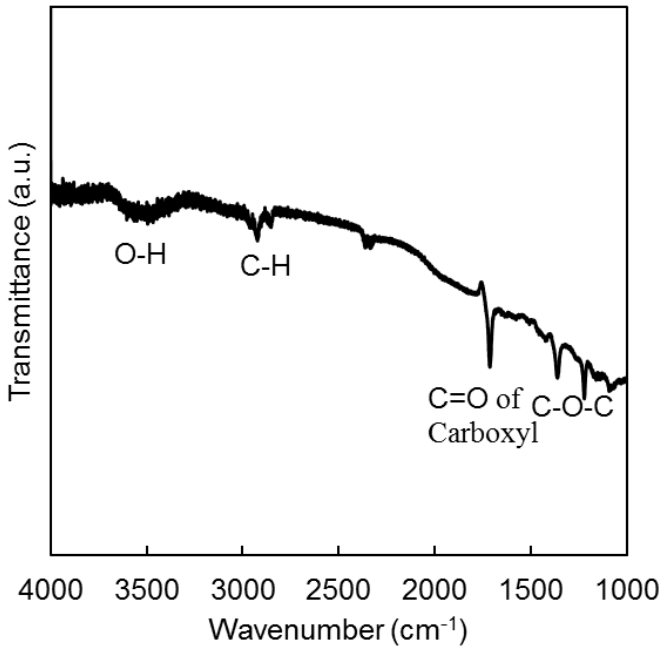

Figure 2.4 FTIR spectrum of as-synthesized GO.

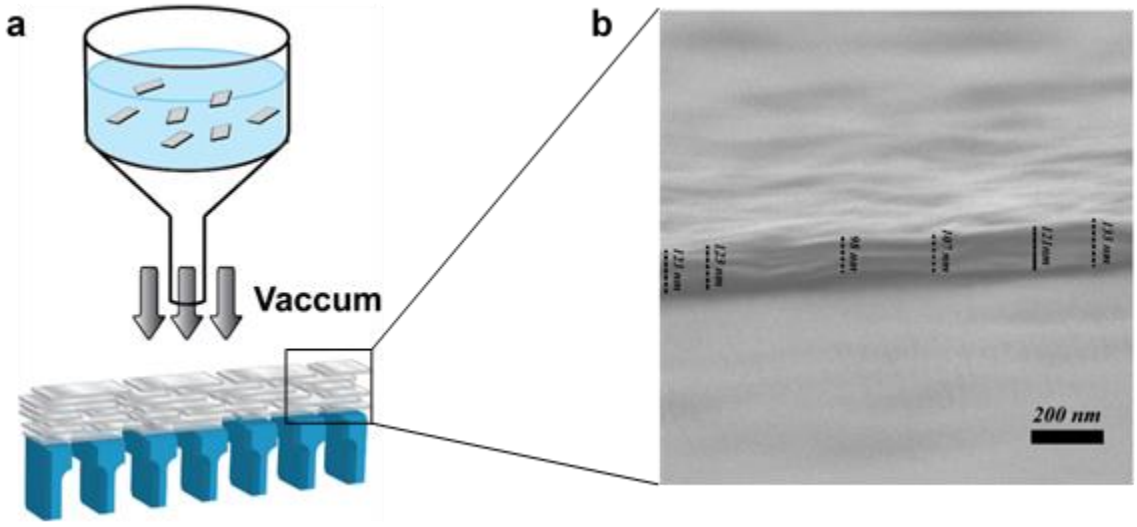

Figure 2.5 (a) Schematic showing vacuum filtration deposition of SLGO flakes on AAO support; (b) calibration of GO loading on AAO by SEM.

In an attempt to fabricate the proposed two interlayer nanostructures (Figure 2.1), GO membranes with the same thickness/SLGO loading were prepared by dispersing the same amount of SLGO in 25 and 250 mL DI water, respectively, to allow fast and slow deposition by vacuum filtration. For instance, to prepare a 118-nm thick GO membrane, it took ~5 min to filter a 25-mL suspension with 0.19 mg of SLGO; for a 250-mL suspension with the same SLGO amount, ~1.5 h was needed to complete the filtration process. Accordingly, the average fast and slow deposition rates of the 118-nm thick GO membrane are calculated as 0.37 and 0.02 nm/s, respectively. The deposition rates of three different GO membrane thicknesses by the slow and fast deposition processes are summarized in Table 2.1. Thus fabricated membranes are denoted as slow- and fast-deposited GO membranes in the following. Cross-sectional FESEM images of representative fast- and slow-deposited membranes were shown in Figure 2.6, demonstrating good lamellar structure of GO membranes prepared within our GO deposition rate range.

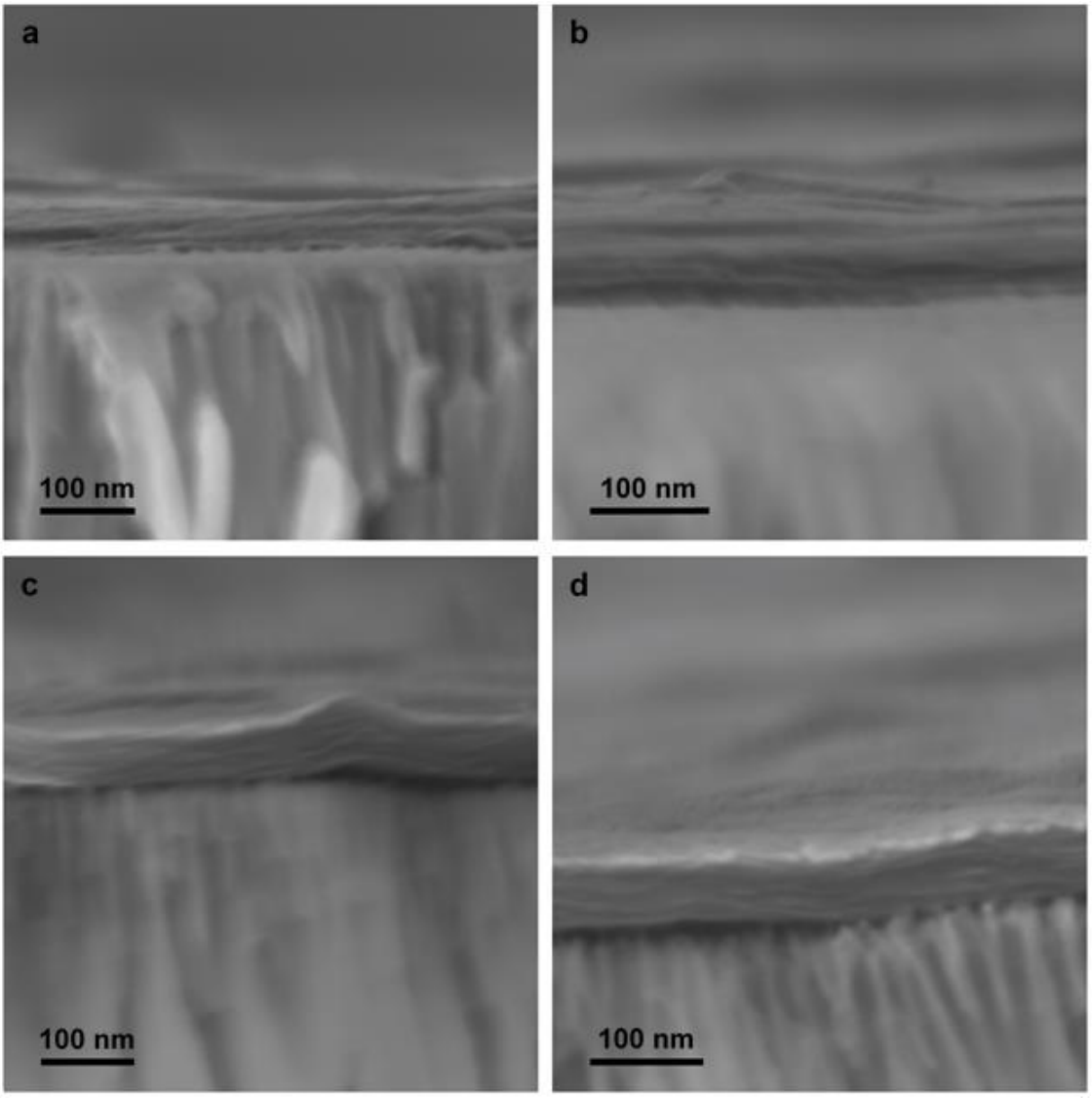

Figure 2.6 Cross-sectional FESEM images of 118-nm rGO membranes prepared at fast deposition rate (a and b: two different spots of the same membrane) and slow deposition rate (c and d: two different spots of the same membrane).

Table 2.1 Average deposition rate of GO membranes with different GO loading and thickness.

GO loading (mg/m^2)	7.4		37.0		184.4	
Membrane thickness (nm)	4.7		23.6		118	
Feed volume (mL)	25	250	25	250	25	250
Average deposition rate (nm/s)	0.10	0.003	0.25	0.02	0.37	0.02

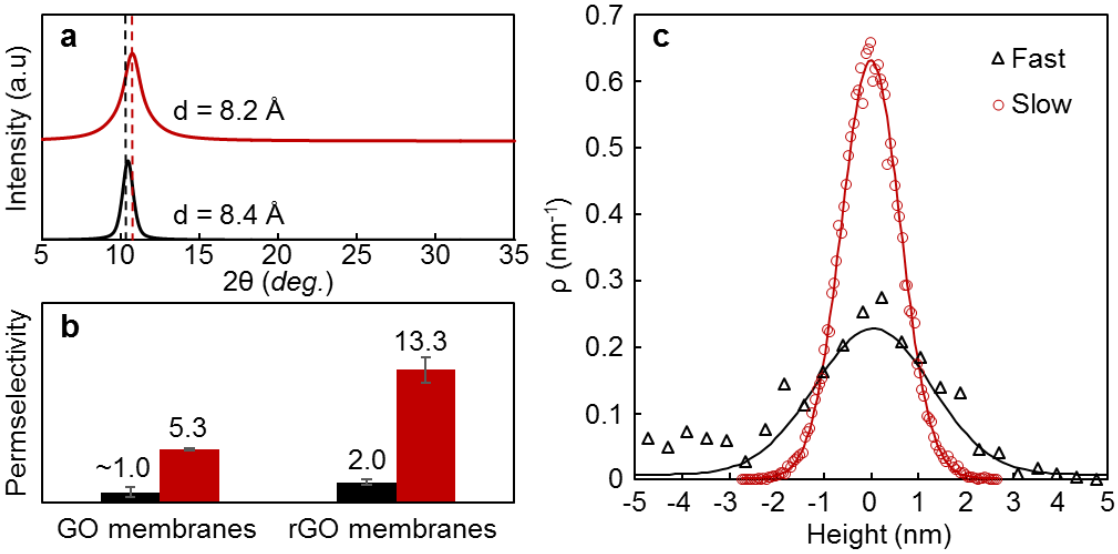

Figure 2.7 Characterization of fast- and slow-deposited GO membranes: (a) XRD patterns of 118-nm thick GO membranes prepared by fast (black) and slow (red) deposition rates; (b) Permselectivity for n-hexane over 2, 2-dimethylbutane (DMB) of fast- (black) and slow-deposited (red), 118-nm thick GO and corresponding rGO membranes which prepared by mild thermal reduction; (c) Height distributions for the top layer of two overlapped SLGO flakes prepared at fast (black) and slow (red) deposition rate; the AFM scan was conducted for the samples exposed to 100% water relative humidity. The solid line is the Gaussian fit of height distribution. To clarify the top layer roughness difference between overlapped SLGO flakes prepared at slow and fast deposition conditions, the mean of the Gaussian fit was set as zero and the height distribution curve was shifted accordingly as well.

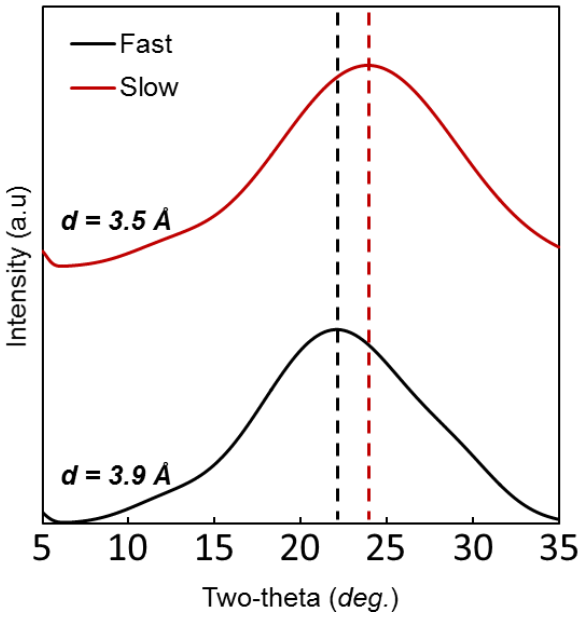

Figure 2.8 XRD patterns of the correspondent rGO membranes which prepared by thermal reduction of 118 nm GO membrane.

To explore the possible structure difference between slow- and fast-deposited GO membranes, XRD was firstly performed to measure the average interlayer spacing (d-spacing). XRD analysis was conducted for a 118-nm thick GO membrane to obtain better signal (Figure 2.7a). The XRD pattern shows that the (001) peak of the fast-deposited GO membrane locates at 10.46°, whereas that of slow-deposited GO membrane is at 10.72°. This suggests that the average interlayer spacing is slightly narrowed from 8.4 to 8.2 Å, when SLGO flakes were slowly deposited on AAO surface. As shown in Figure 2.8, similar trend could be found on thermally reduced GO membranes. After reduction, the interlayer spacing of the fast-deposited GO membrane shrinks to 3.9 Å, whereas the slow-deposited membrane shows even tighter packing with an interlayer distance of ~3.5 Å. These XRD results suggest that different deposition rates might bring about structural change in GO membranes, and slow deposition leads to narrower interlayer nanochannels. XPS

measurements of reduced GO membranes were conducted to further clarify the structural difference between slow- and fast-deposited GO membranes and its influence on mild thermal reduction (Tables 2.2 and 2.3). After reduction, GO membrane prepared at slow deposition rate exhibits higher C/O ratio (1.61) than the fast-deposited one (1.49), implying that the narrower interlayer nanostructure of slow-deposited GO membrane might facilitate the dehydration of GO in the thermal reduction process.

Table 2.2 XPS parameter of rGO membrane prepared at fast/slow rate.

Fast filtrate membrane	Peak	Position (eV)	Function group	Ratio
C1s	0	284.543	C=C	56.9 ± 6.0 %
	1	286.46	C-O	23.1 ± 1.4 %
	2	288.715	C=O	20.0 ± 4.6 %
O1s	0	533.301	C-O-C	43.3 ± 3.1 %
	1	531.952	OH	34.1 ± 1.4 %
	2	531.1	C=O	22.6 ± 1.8 %
Slow filtrate membrane	Peak	Position (eV)	Function group	Ratio
C1s	0	284.54	C=C	64.4 ± 4.4 %
	1	286.46	C-O	20.8 ± 1.1 %
	2	288.677	C=O	14.8 ± 3.4 %

O1s	0	533.344	C-O-C	38.9 ±4.1 %
	1	532.044	OH	37.1 ±2.7 %
	2	531.17	C=O	24.0 ±1.8 %

Table 2.3 Carbon/oxygen ratio of GO and rGO membrane.

	GO	Fast Prepared rGO	Slow Prepared rGO
C:O	0.75	1.49	1.61

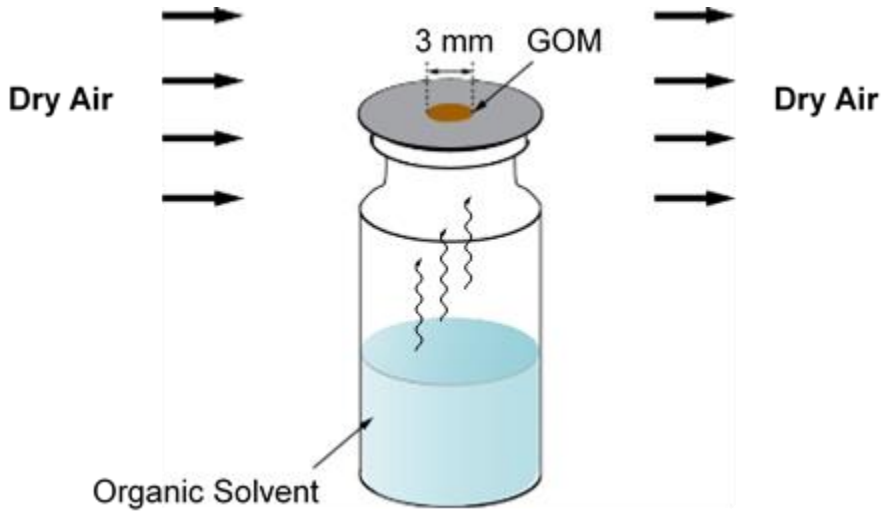

Figure 2.9 Schematic showing of organic vapor diffusion setup.

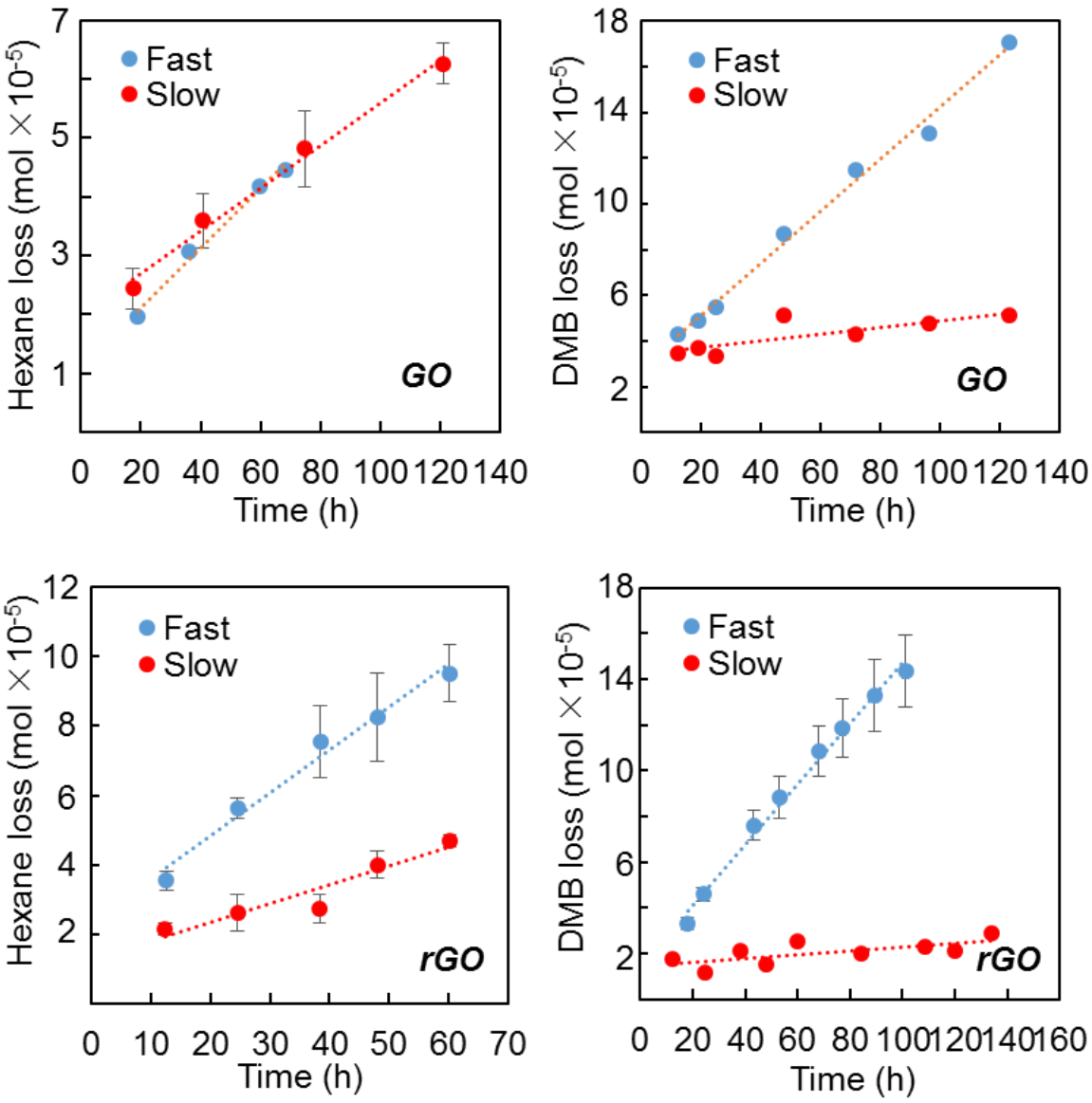

Figure 2.10 Permeation of organic vapor (hexane & 2,2-dimethylbutane (DMB)) through 118 nm GO and rGO membranes at 20 ℃.

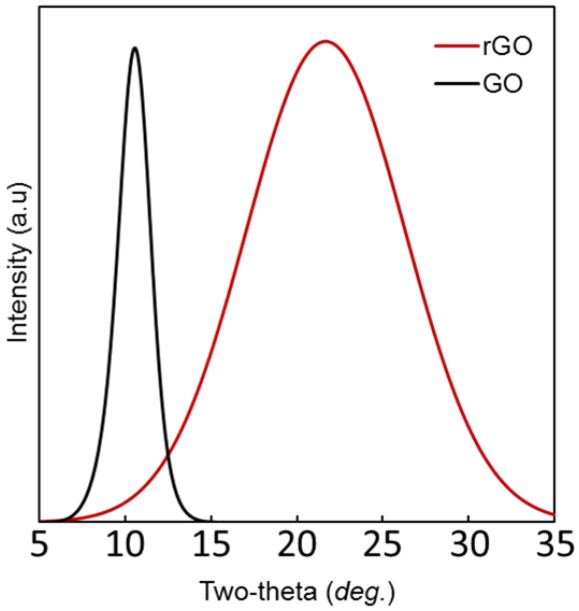

Figure 2.11 XRD pattern of 118 nm GO membrane which was fabricated at intermediate deposition rate (0.08 nm/s) and the corresponding rGO membrane.

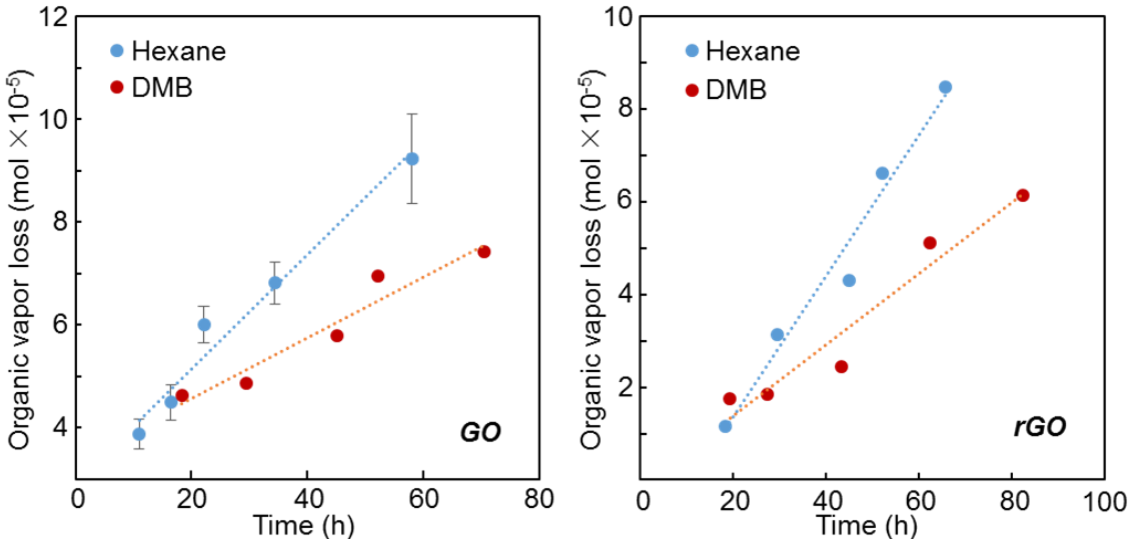

Figure 2.12 Permeation of organic vapor (hexane & 2,2-dimethylbutane (DMB)) through 118 nm GO membranes which fabricated at intermediate deposition rate (0.08 nm/s) and corresponding rGO membranes at 20 ℃.

Vapor permeation measurements (Figure 2.9-2.12 for the experimental detail) for two probe molecules, hexane (kinetic diameter: 0.43 nm) and 2,2-dimethylbutane (DMB;

kinetic diameter: 0.62 nm), were also employed to investigate the effective size of nanochannels between SLGO flakes of slow- and fast-deposited GO membranes. Since these two isomers have different vapor pressure (17.6 kPa for hexane and 36.88 kPa for DMB) and thus different driving force for permeation, permeance (= permeation rate/(membrane area×pressure drop) = flux/pressure drop) was used to study the permeation rate difference and selectivity of membranes. The vapor permeation results (Figure 2.7b) exhibit that hexane transported ~5 times faster than DMB in the slow-deposited GO membrane, whereas the corresponding fast-deposited GO membrane shows no obvious difference. Compared with fast-deposited membrane, although the permeation of both hexane and DMB is retarded in the slow-deposited membrane, DMB permeates ~8 time slower, whereas hexane only ~1.3 times (Table 2.4). This suggests that the higher hexane/DMB selectivity of slow-deposited GO membrane might be attributed to the narrower d-spacing/average nanochannel size, which drags down the transport of larger DMB more than that of hexane. The influence of deposition rate on organic vapor permeation becomes even more notable for the reduced GO membranes. After reduction, the permselectivity (ratio of the permeances) of hexane over DMB of the slow-deposited membrane increases to 13, while the fast-deposited one has a selectivity of only ~2. These vapor permeation results indicate GO membrane prepared at slow deposition rate possesses smaller effective size of the interlayer nanochannels, which further supports the XRD results. Since hexane and DMB are expected to interact more favorably with hydrophobic domains in GO membranes and thus their main transport pathway is expected to be the hydrophobic nanochannels, the nanochannel size explored is probably corresponding the hydrophobic domains.

Table 2.4 Organic vapor permeance (mol·m-2 s-1 Pa-1) of 118 nm GO and rGO membranes.

Membrane Thickness (nm)	118 (GO)		118 (rGO)	
Deposition rate	Fast	Slow	Fast	Slow
Hexane (4.3 Å)	1.13×10^{-9}	8.11×10^{-10}	2.75×10^{-9}	1.20×10^{-9}
DMB (6.2 Å)	1.22×10^{-9}	1.52×10^{-10}	1.41×10^{-9}	9.05×10^{-11}

Table 2.5 Organic vapor permeance (10^{-6} mol.m^{-2} s^{-1} Pa^{-1}) of 4.7 and 23.6 nm GO and rGO membranes.

Membrane Thickness (nm)	4.7 (GO)		4.7 (rGO)		23.6 (GO)		23.6 (rGO)	
Deposition	Fast	Slow	Fast	Slow	Fast	Slow	Fast	Slow
Hexane (4.3 Å)	1.32	1.40	1.10	1.21	0.04	0.04	0.24	0.06
DMB (6.2 Å)	1.29	1.42	1.15	1.41	0.37	0.37	0.15	0.03

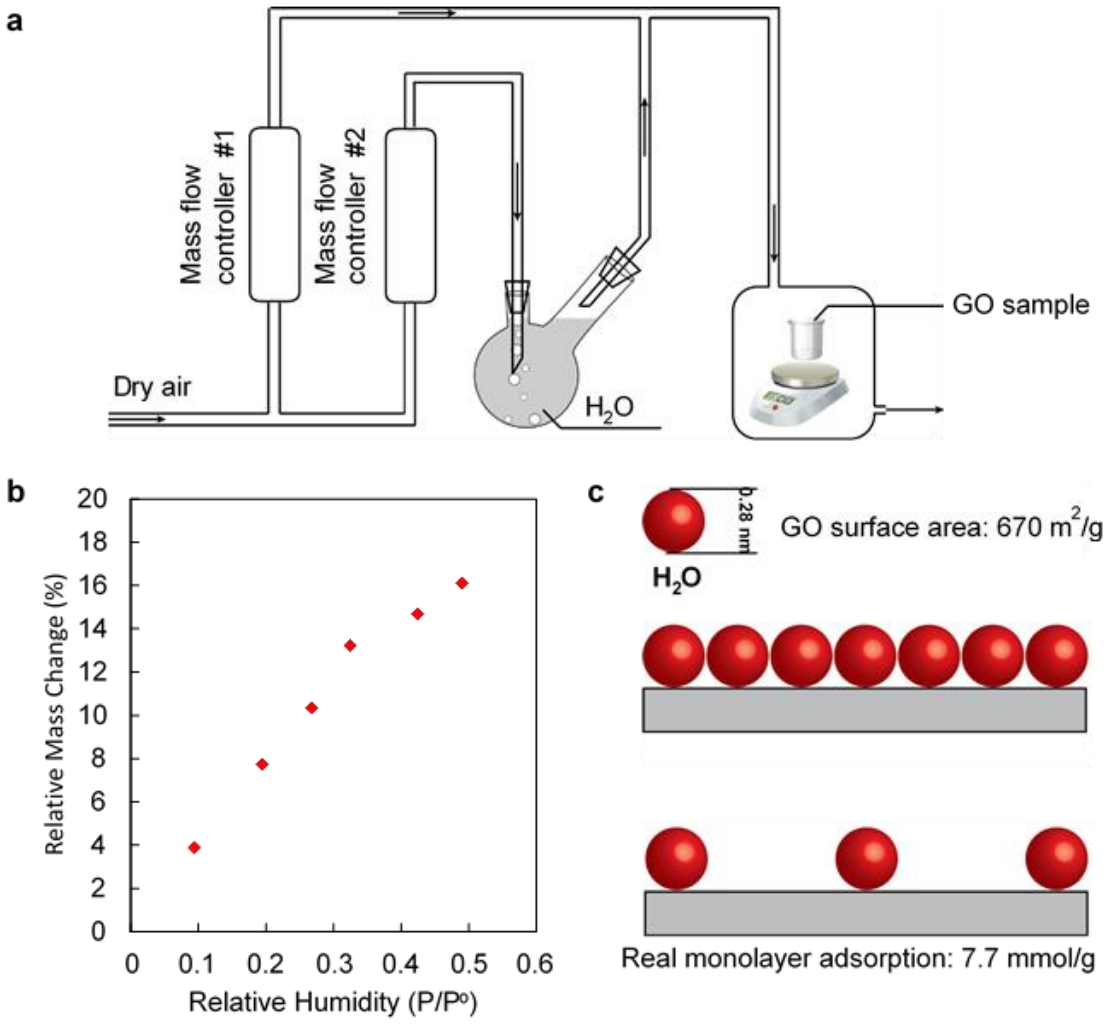

Figure 2.13 (a) Schematic showing of water adsorption isotherm system; (b) Water adsorption isotherm at 20 ℃; (c) Schematic showing of ideal and real monolayer adsorption on graphene oxide surface.

Understanding water adsorption on and between SLGO flakes and the response of interlayer nanostructures upon water adsorption may further help reveal the difference between interlayer nanostructures formed by slow and fast deposition of SLGO. Bases on the water adsorption isotherm shown in Figure 2.13b, water monolayer adsorption (n_m) can be estimated by using the linear form of BET equation:$\frac{p}{n(p^0-p)} = \frac{1}{n_m C} + \frac{C-1}{n_m C} \times \frac{p}{p^0}$, and was calculated as ~7.7 mmol/g. This suggests that a maximum of 7.7 mmol of water molecules

are distributed on the surface of GO before water molecules starts to form clusters. If water molecule was considered as a hard sphere with a diameter of 0.28 nm (Figure 2.13c), theoretically, at least 18.1 mmol is needed to form a continuous monolayer cover on GO with a BET surface area of 670 m^2/g (measured form 77 K N2 adsorption). This suggests that, in the real case, water molecules are not continuously distributed and can only cover ~43% of the area of a GO surface, on average, which is consistent with the percentage of oxidized regions (~50%, confirmed by XPS) on GO. Therefore, the water adsorption isotherm on SLGO indicates that water molecules may preferentially adsorb on hydrophilic sites and thus do not form a continuous water phase between GO flakes.

Considering different hydrophilic sites/oxygen-containing groups distribution between SLGO flakes, type I and type II structures are expected to respond differently to water adsorption. AFM was applied to investigate surface roughness change, when two SLGO flakes were stacked together by fast and slow deposition processes and then exposed to different humidity. As shown in Figure 2.14a, the interlayer distance *d* could be estimated by subtracting the height of single layer GO (I) from double layer (II). After scanning two overlapped SLGO flakes, deposited through a slow evaporation process, under different humidity conditions, the expansion of interlayer distance was plotted as a function of humidity and is shown in Figure 2.14b. We observed that the interlayer distance *d* was gradually expanded with the increase of humidity. The detailed topography image of double layer SLGO flakes (II) is shown the insets of Figure 2.14b, these two images have the same color scale of 4 nm from black to white. Incensement of SLGO-double layer thickness can be easily represented by the color of scan image. At higher humidity (65%), the height of SLGO bilayer was not evenly distributed in the scan area, and different sites

on the GO flakes exhibit uneven reflection to water. Combing with the gradual expansion of interlayer distance, these two phenomena may suggest that, instead of simply separate SLGO flakes through a continuous monolayer structure, water was gradually inserted into SLGO layers and accumulate at the oxidized domains of SLGO flakes as clusters. The uneven distribution of water between SLGO flakes can also be supported by the height distribution of SLGO double-layer. The height distribution of overlapped SLGO flakes (Figure 2.14c) shows that, while the relative humidity increased from 16% to 65%, the FWHM of height profile expanded from 0.85 nm to 1.11 nm. This indicates that the surface of the region composed of two layers of SLGO became rougher at high humidly condition, suggesting water molecules preferentially insert/accumulate on some sites between SLGO flakes. This supports the discontinuous distribution of water between SLGO flakes and consistent with Rezania et al.'s finding.[8]

As water molecules are shown to adsorb preferentially to the oxidized sites of GO flakes, using AFM to scan water saturated SLGO double-layers prepared under different deposition rates might give an intuitive evidence to our deposition rate dependent membrane assembly mechanism. For SLGO double-layers prepared at ultraslow rate, well assembled hydrophilic groups will make less water accumulation sites in the SLGO layer. On the contrary, random packed membrane, prepared at ultrafast deposition rate, will have more hydrophilic sites exposed to water and consequently make the membrane surface rougher. The slow deposited SLGO double-layer sample was prepared through slow evaporation at r.t; the fast deposited correspondent was prepared by sweeping the sample surface with 70 ℃ hot air. The height distribution, which measured at 16% relative

humility, of overlapped SLGO flakes prepared at fast and slow deposition rate is shown in Figure 2.14d.

As water molecules are shown to adsorb preferentially on the oxidized sites of GO flakes, AFM topological scanning on 100%-water-saturated overlapped SLGO flakes prepared at different deposition rates could provide evidence for our deposition-rate-correlated interlayer nanostructures. For the overlapped SLGO flakes deposited at slow evaporation rate of water, well-assembled hydrophilic groups (type I structure) are expected to result in fewer exposed water accumulation sites between the GO flakes. In contrast, as overlapped SLGO flakes were deposited at a fast evaporation rate, more hydrophilic sites are expected to be exposed to water (type II structure), and consequently make the top layer surface rougher. The height distribution diagram indicates that, under dry condition, both fast- and slow-deposited SLGO bilayers have similar top layer surface roughness (Figure 2.14d). While under 100% relative humidity, the Gaussian fit for the height distribution of the fast-deposited SLGO bilayer presents a full width at half maximum (FWHM) of 2.9 nm, whereas slow-deposited GO bilayer has a FWHM of only 1.5 nm, as shown in Figure 2.7c, demonstrating that the surface of the fast-deposited GO bilayer is about twice as rough as the slow-deposited one. This is consistent with our assumption, and supports the conclusion that fast deposition rate leads to type II nanostructure, while the type I nanostructure results at a slow deposition rate.

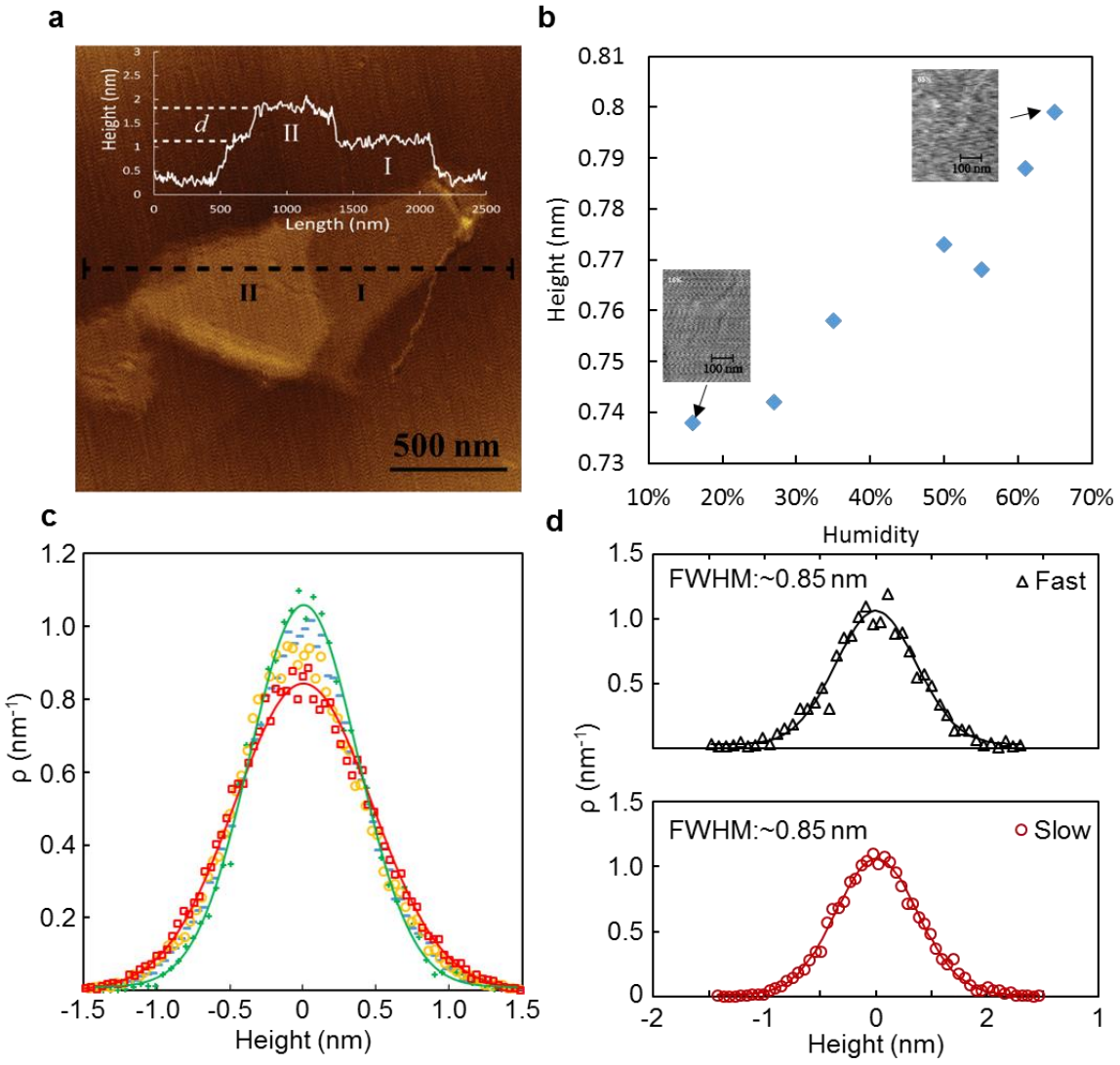

Figure 2.14 Characterization of water insertion between SLGO layers: (a) AFM image of two overlapped SLGO flakes; regions of one SLGO flake and two stacking SLGO flakes are labeled as I and II, respectively; inset shows the height profile measured along the black dash line draw; (b) Growth of the interlayer distance d with humidity in air; inset images show the detailed topography image of the same area in region II at 16% and 65% humidity, and these two images were nominalized to the same color scale of 4 nm from black to white; (c) Height distribution of the top layer of selected area (region II) of overlapped SLGO flakes. The solid line is the Gaussian fit of height distribution. To clarify the top layer roughness changing at different humility, the mean of the Gaussian fit was set as zero and the height distribution curve was shifted accordingly as well; (d) Height distributions for the top layer of two overlapped SLGO flakes which prepared at fast and slow deposition rate, the AFM scan was conducted under 16% water relative humility.

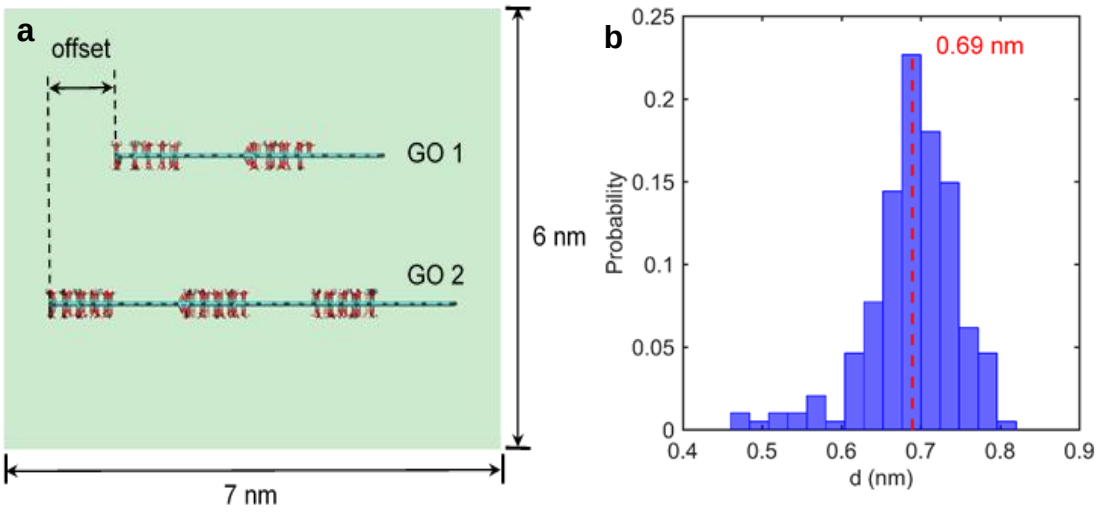

Figure 2.15 (a) Schematic of self-assembly simulation system consists of two SLGOs immersed in water. (b) The histogram of the spacing between the two SLGOs at different positions in the horizontal plane when the self-assembly has reached equilibrium (t = 10 ns-20 ns). The average spacing is 0.69 nm (red dashed line).

To ascertain that the type I nanostructure is indeed thermodynamically more favorable than the type II nanostructure, we performed molecular dynamics (MD) simulations to study the self-assembly of SLGO flakes in water. Prior experiments and simulations revealed that the surfaces of GOs are heterogeneous: oxygen-containing surface groups tend to cluster together to form oxidized patches with size of 1-2 nm, thus leaving many pristine areas free of functionalization groups.[33-37] Here, without losing generality, we simulated the self-assembly of two SLGO flakes both featuring 1 nm wide strips of oxidized and pristine surfaces (Figure 2.16a). The self-assembly of SLGO in water can lead to different interlayer structures depending on the relative arrangement of oxidized and pristine surfaces in the neighboring GOs. The interlayer structure formed by these two SLGO flakes typically exhibits three types of subdomains (inset in Figure 2.16b): an oxidized surface facing another oxidized surface (O-O), a pristine surface facing another pristine surface (P-P), and an oxidized surface facing a pristine surface (O-P). The O-O

and P-P subdomains correspond to the type I structure shown in Figure 2.1, while the O-P subdomain corresponds to the type II structure. At the beginning of the self-assembly process, the oxidized strips of the two SLGOs are offset by ~0.5 nm. Hence the interlayer nanostructure is dominated by O-P subdomains (~50%). As shown in Figure 2.16b, as the self-assembly proceeds, the fraction of O-P subdomains decreases, whereas that of the O-O and P-P subdomains increases. At $t > 5$ ns, the interlayer structure approaches equilibrium with the fractions of O-O and P-P subdomains both approaching 40%. Overall, self-assembly of SLGOs in liquid water favors the formation of type I interlayer structure over type II interlayer structure.

To ascertain that the type I nanostructure is indeed thermodynamically more favorable than the type II nanostructure, we performed molecular dynamics (MD) simulations to study the self-assembly of SLGO flakes in water. Prior experiments and simulations revealed that the surfaces of GOs are heterogeneous: oxygen-containing surface groups tend to cluster together to form oxidized patches with size of 1-2 nm, thus leaving many pristine areas free of functionalization groups.[33-37] Here, without losing generality, we simulated the self-assembly of two SLGO flakes both featuring 1 nm wide strips of oxidized and pristine surfaces (Figure 2.16a).

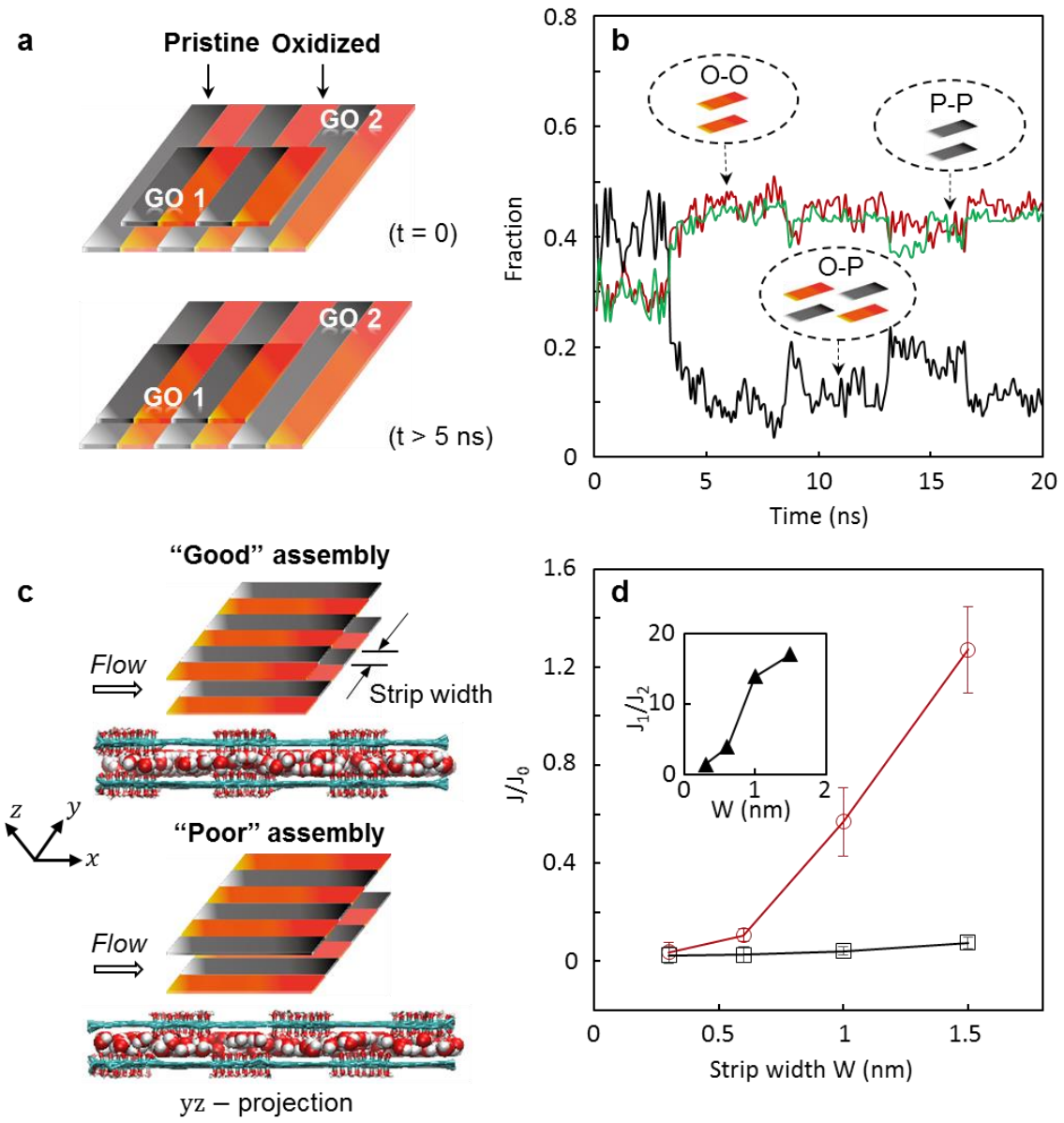

Figure 2.16 Self-assembly of SLGO in water and water transport through interlayer nanochannels: (a) A sketch of the two heterogeneous SLGOs used in self-assembly simulations. The oxidized and pristine strips of the two SLGOs are offset by ~0.5 nm at the beginning of self-assembly. (b) Evolution of the three type subdomains of the SLGO during self-assembly. Inset sketches the subdomain types: O-O (an oxidized surface of one GO faces an oxidized surface of the other GO), P-P (a pristine surface of one GO faces a pristine surface of the other GO), and O-P (an oxidized surface of one GO faces a pristine surface of the other GO). (c) Sketches of the systems for studying water transport through two SLGO flakes in good and poor assembly configurations. (d) Normalized mass flux from "good" (red) and "poor" (black) assembly configurations with different strip sizes. The inset shows the ratio of water flux for good and poor assembly configurations as a function of strip size.

The self-assembly of SLGO in water can lead to different interlayer structures depending on the relative arrangement of oxidized and pristine surfaces in the neighboring GOs. The interlayer structure formed by these two SLGO flakes typically exhibits three types of subdomains (inset in Figure 2.16b): an oxidized surface facing another oxidized surface (O-O), a pristine surface facing another pristine surface (P-P), and an oxidized surface facing a pristine surface (O-P). The O-O and P-P subdomains correspond to the type I structure shown in Figure 2.1, while the O-P subdomain corresponds to the type II structure. At the beginning of the self-assembly process, the oxidized strips of the two SLGOs are offset by ~0.5 nm. Hence the interlayer nanostructure is dominated by O-P subdomains (~50%). As shown in Figure 2.16b, as the self-assembly proceeds, the fraction of O-P subdomains decreases, whereas that of the O-O and P-P subdomains increases. At $t > 5$ ns, the interlayer structure approaches equilibrium with the fractions of O-O and P-P subdomains both approaching 40%. Overall, self-assembly of SLGOs in liquid water favors the formation of type I interlayer structure over type II interlayer structure.

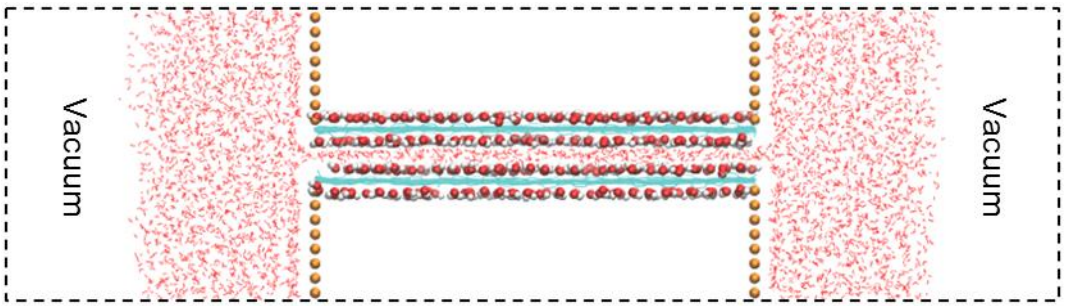

Figure 2.17 A snapshot of the MD system used to determine the number of water molecules between SLGO bilayers. The dashed lines denote the periodical simulation box.

The interlayer structure between SLGO flakes can potentially influence the transport of water molecules through GO membranes. We examine its effect using MD simulations. Given the complexity and heterogeneity of the interlayer structure in practical GO membranes are difficult to be fully accounted for in simulations, here we consider only two limiting cases (Figure 2.16c): the "good" assembly that contains only O-O and P-P subdomains and the "poor" assembly that contains only O-P subdomains. For SLGO flakes featuring alternating strips of pristine and oxidized surfaces, these two interlayer structures are idealistic representations of the type I and II structures illustrated in Figure 2.1, and they correspond to the most and least thermodynamically favorable states of packed SLGO. Since the size of pristine and oxidized patches in real GO membranes shows a statistical distribution, we varied the width of pristine and oxidized strips in both "good" assembly and "poor" assembly from 0.3 to 1.5 nm in different simulations. In these simulations, the spacing between SLGO flakes was taken as 0.69 nm, the equilibrium spacing between SLGOs found in the above self-assembly simulations. Adopting a constant spacing is in line with the experimental observation that, for GO membranes prepared by different methods, the difference in the interlayer spacing is on the order of sub-angstroms;[38,39] we also verify that using a different spacing does not qualitatively change the water transport behavior. Figure 2.16d compares the water flux through the nanochannels between the SLGO flakes with "good" and "poor" assemblies. For a strip width of 1.5 nm, the mass flux of water in the "good" assembly case is slightly higher than that predicted by using the classical Poiseuille flow equation, but the flux in the "poor" assembly case is about 10 times lower than the Poiseuille flow prediction. As shown in the inset of figure 2.16d, the water flux in the two different structures becomes similar as the strip width reduces but

remains significant for a strip width of 1.0 nm. The water flux is higher in the "good" assembly case because the hydrophobic nanochannels in the P-P subdomains provide more effective transport pathways for water molecules than the nanochannels in the O-O and O-P subdomains. In the latter subdomains, water molecules form extensive hydrogen bonds with the OH groups on the surface of SLGO, which impedes the transport of water.[38,40] Note that water flux in the "good" assembly case does not greatly exceed that predicted by classical theory assuming no-slip boundary condition at GO-water interfaces. This is consistent with the recent findings that the slip of water monolayers confined between the hydrophobic patches in GO membranes is greatly suppressed by the slow transport of the water molecules confined between oxidized patches (termed "side-pinning" in some studies).[41] Nevertheless, it is clear that water permeance is faster through type I interlayer structure than through type II interlayer structure.

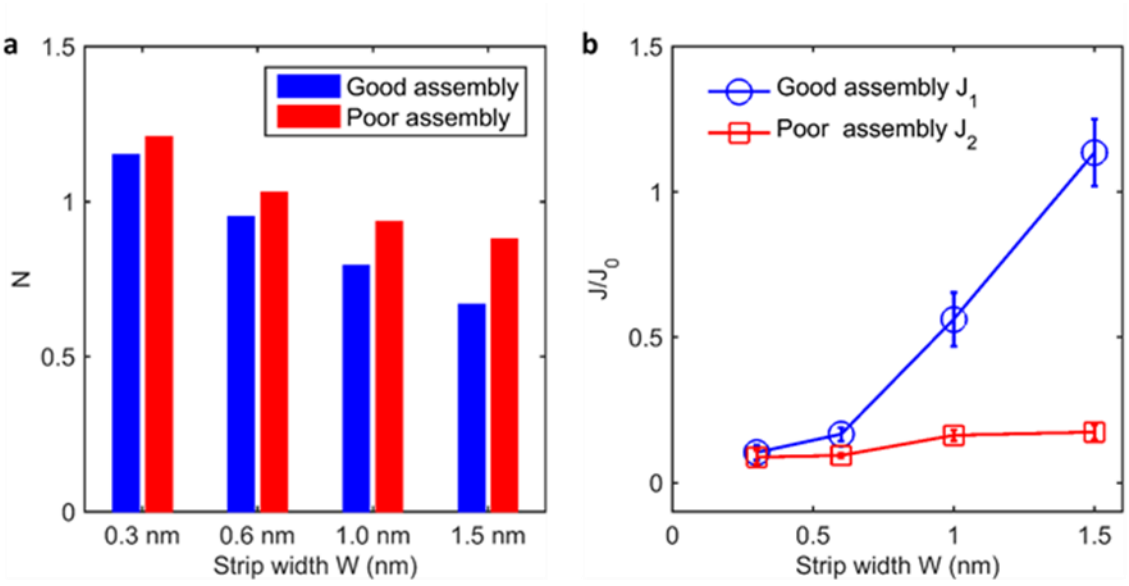

Figure 2.18 (a) Number of hydrogen bonds between water molecule and SLGOs per water molecule in the flux simulation with different strip size and assembly configuration. The spacing between the SLGOs is 0.69 nm; (b) Normalized mass flux from good and poor

assembly configuration with different strip sizes. The spacing between the two SLGOs is 0.72 nm.

Motivated by the above predictions that interlayer structure of GO membranes significantly affects the water transport through the membranes, we next experimentally measured the flux of pure water through fast- and slow-deposited GO membranes. We find that the slow-deposited GO membranes have much higher water permeance (pressure normalized water flux) than the fast-deposited membranes. As shown in Figure 2.19a, the slow-deposited 4.7- and 23.6-nm GO membranes show ~2.5 times higher steady state water permeance than that of the fast-deposited ones. As the thickness increasing to 118 nm (inset, Figure 2.19a), the water permeance of the slow-deposited membrane is around 4 times higher than that of the fast-deposited GO membrane. Since slow-deposited GO membranes are expected to feature more type I interlayer structure than the fast-deposited membranes, these observations corroborate the MD predictions that water transport is faster through GO membranes with type I interlayer structure. The difference of water permeance in slow- and fast-deposited GO membranes is not as significant as that revealed in the MD simulations because the oxidized regions on SLGO surfaces in real GO membranes is unlikely to be well-aligned as modeled in the MD simulations.

To demonstrate superior nanofiltration performance of slow-deposited GO membranes, long term salt rejection tests for KCl, NaCl and $MgSO_4$ were conducted on 4.7-nm GO membranes due to its high water permeance, and the rejection results for various salts reported in Figure 2.19b represent steady state results, meaning no measurable changes within last 2 h. Figure 2.19b shows that the slow-deposited GO membrane with favorable nanostructure after self-assembly has 1.8~4 times higher salt rejection than that

of the fast-deposited GO membrane. As far as we know, this is the thinnest GO membrane with comparable salt rejection as that of much thicker GO membranes.[12,13] The slow-deposited, 4.7-nm GO membrane maintains its higher salt rejection at higher salt concentration, as shown in Figure 2.20; as concentration increases to 50 and 100 mM, slow-deposited GO membrane still exhibits at least ~2 times higher NaCl rejection than that of the fast-deposited GO membrane. Thus, the ion exclusion results clearly illustrate that a membrane with type I structure has better size-dependent sieving properties besides its greatly enhanced water flux.

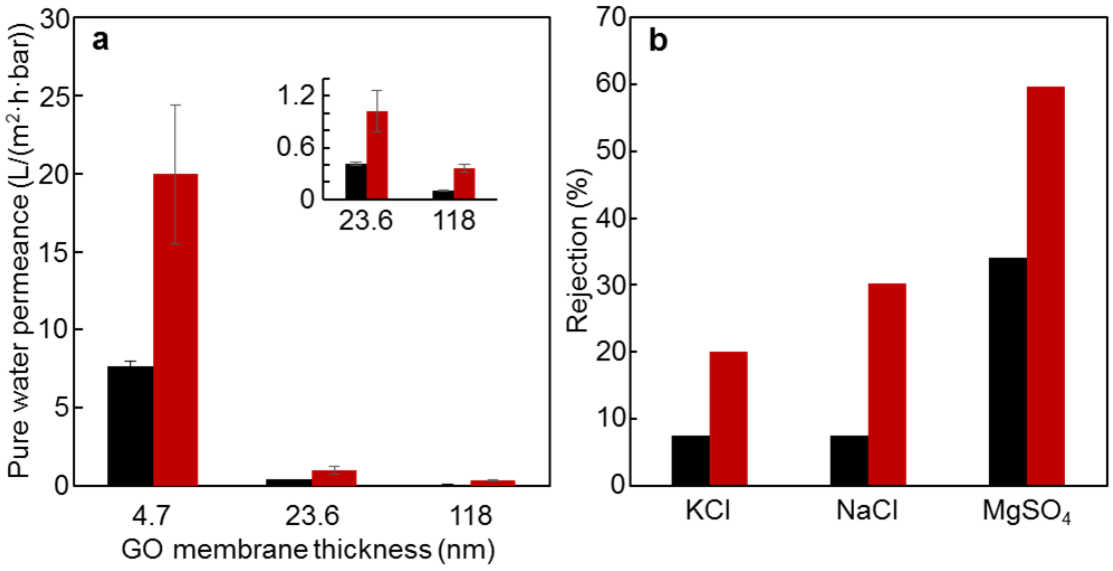

Figure 2.19 (a) Water permeation through GO membranes prepared by fast (black) and slow-deposition (red) rates; inset shows the water permeance of two thicker membranes at smaller scale of y-axis; (b) Salt rejection of 4.7-nm thick GO membrane prepared at fast/slow deposition rate

Table 2.6 Pure water flux of 4.7, 23.6, 118-nm GO membranes prepared at fast and slow deposition rate, respectively.

Membrane Thickness (nm)	4.7		23.6		118	
Deposition Rate	Fast	Slow	Fast	Slow	Fast	Slow
Pure Water Flux ($L.m^{-2}.h^{-1}.bar^{-1}$)	7.64	19.97	0.41	1.02	0.10	0.36

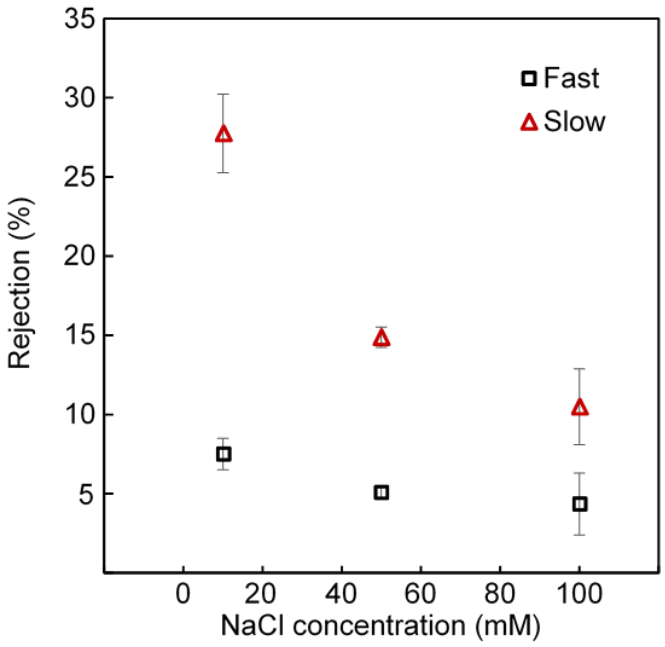

Figure 2.20 Rejection of different concentrations of NaCl by 4.7 nm thick GO membranes prepared at fast and slow deposition rates.

2.5 CONCLUSION

In summary, we demonstrate that interlayer nanostructures between SLGO flakes can be "tuned" between type I structure and type II structure, as shown in Figure 2.1, by simply controlling SLGO flake deposition rate in solution phase deposition process. Structure characterization and MD simulations confirm that type I structure is more thermodynamically favored structure and facilitates fast water permeation. Experimental results show that compared with type II structure, narrower hydrophobic nanochannels in type I structure lead to 2.5~4 times faster water permeation rate and 1.8~4 times higher salt rejection. We believe this finding helps break the current trade-off between water flux and precise sieving performance of GO membranes, and may eventually lead to novel design of ultrathin GO-based membranes for high flux and high selectivity water purification.

REFERENCE

(1) Geim, A. K.; Novoselov, K. S. *Nature Materials* **2007**, *6*, 183.

(2) Geim, A. K. *Science* **2009**, *324*, 1530.

(3) Dreyer, D. R.; Park, S.; Bielawski, C. W.; Ruoff, R. S. *Chem. Soc. Rev.* **2010**, *39*, 228.

(4) Huang, H. B.; Ying, Y. L.; Peng, X. S. *Journal of Materials Chemistry A* **2014**, *2*, 13772.

(5) Surwade, S. P.; Smirnov, S. N.; Vlassiouk, I. V.; Unocic, R. R.; Veith, G. M.; Dai, S.; Mahurin, S. M. *Nature Nanotechnology* **2015**, *10*, 459.

(6) Fathizadeh, M.; Xu, W. L.; Zhou, F.; Yoon, Y.; Yu, M. *Advanced Materials Interfaces* **2017**, *4*.

(7) Nair, R. R.; Wu, H. A.; Jayaram, P. N.; Grigorieva, I. V.; Geim, A. K. *Science* **2012**, *335*, 442.

(8) Rezania, B.; Severin, N.; Talyzin, A. V.; Rabe, J. P. *Nano Lett.* **2014**, *14*, 3993.

(9) Sun, P. Z.; Zhu, M.; Wang, K. L.; Zhong, M. L.; Wei, J. Q.; Wu, D. H.; Xu, Z. P.; Zhu, H. W. *Acs Nano* **2013**, *7*, 428.

(10) Joshi, R. K.; Carbone, P.; Wang, F. C.; Kravets, V. G.; Su, Y.; Grigorieva, I. V.; Wu, H. A.; Geim, A. K.; Nair, R. R. *Science* **2014**, *343*, 752.

(11) Sun, P. Z.; Liu, H.; Wang, K. L.; Zhong, M. L.; Wu, D. H.; Zhu, H. W. *Chem. Commun.* **2015**, *51*, 3251.

(12) Han, Y.; Xu, Z.; Gao, C. *Adv. Funct. Mater.* **2013**, *23*, 3693.

(13) Hu, M.; Mi, B. X. *Environmental Science & Technology* **2013**, *47*, 3715.

(14) Huang, H. B.; Mao, Y. Y.; Ying, Y. L.; Liu, Y.; Sun, L. W.; Peng, X. S. *Chem. Commun.* **2013**, *49*, 5963.

(15) Li, H.; Huang, Y.; Mao, Y. T.; Xu, W. W. L.; Ploehn, H. J.; Yu, M. *Chem. Commun.* **2014**, *50*, 9849.

(16) Sun, P. Z.; Zheng, F.; Zhu, M.; Song, Z. G.; Wang, K. L.; Zhong, M. L.; Wu, D. H.; Little, R. B.; Xu, Z. P.; Zhu, H. W. *Acs Nano* **2014**, *8*, 850.

(17) Zhang, Y.; Zhang, S.; Chung, T. S. *Environmental Science & Technology* **2015**, *49*, 10235.

(18) Liu, H. Y.; Wang, H. T.; Zhang, X. W. *Adv. Mater.* **2015**, *27*, 249.

(19) Chong, J. Y.; Aba, N. F. D.; Wang, B.; Mattevi, C.; Li, K. *Scientific Reports* **2015**, *5*.

(20) Akbari, A.; Sheath, P.; Martin, S. T.; Shinde, D. B.; Shaibani, M.; Banerjee, P. C.; Tkacz, R.; Bhattacharyya, D.; Majumder, M. *Nature Communications* **2016**, *7*.

(21) Marcano, D. C.; Kosynkin, D. V.; Berlin, J. M.; Sinitskii, A.; Sun, Z. Z.; Slesarev, A.; Alemany, L. B.; Lu, W.; Tour, J. M. *Acs Nano* **2010**, *4*, 4806.

(22) Cancado, L. G.; Jorio, A.; Ferreira, E. H. M.; Stavale, F.; Achete, C. A.; Capaz, R. B.; Moutinho, M. V. O.; Lombardo, A.; Kulmala, T. S.; Ferrari, A. C. *Nano Lett.* **2011**, *11*, 3190.

(23) Jorgensen, W. L.; Maxwell, D. S.; Tirado-Rives, J. *Journal of the American Chemical Society* **1996**, *118*, 11225.

(24) Hess, B.; Kutzner, C.; van der Spoel, D.; Lindahl, E. *Journal of Chemical Theory and Computation* **2008**, *4*, 435.

(25) Hess, B.; Bekker, H.; Berendsen, H. J. C.; Fraaije, J. G. E. M. *Journal of Computational Chemistry* **1997**, *18*, 1463.

(26) Bussi, G.; Donadio, D.; Parrinello, M. *The Journal of Chemical Physics* **2007**, *126*, 014101.

(27) Darden, T.; York, D.; Pedersen, L. *The Journal of Chemical Physics* **1993**, *98*, 10089.

(28) Raghav, N.; Chakraborty, S.; Maiti, P. K. *Physical Chemistry Chemical Physics* **2015**, *17*, 20557.

(29) González, M. A.; Abascal, J. L. F. *The Journal of Chemical Physics* **2010**, *132*, 096101.

(30) Mark, P.; Nilsson, L. *The Journal of Physical Chemistry A* **2001**, *105*, 9954.

(31) Ferrari, A. C.; Robertson, J. *Physical Review B* **2000**, *61*, 14095.

(32) Graf, D.; Molitor, F.; Ensslin, K.; Stampfer, C.; Jungen, A.; Hierold, C.; Wirtz, L. *Nano Lett.* **2007**, *7*, 238.

(33) Wilson, N. R.; Pandey, P. A.; Beanland, R.; Young, R. J.; Kinloch, I. A.; Gong, L.; Liu, Z.; Suenaga, K.; Rourke, J. P.; York, S. J.; Sloan, J. *ACS Nano* **2009**, *3*, 2547.

(34) Pacilé, D.; Meyer, J. C.; Fraile Rodríguez, A.; Papagno, M.; Gómez-Navarro, C.; Sundaram, R. S.; Burghard, M.; Kern, K.; Carbone, C.; Kaiser, U. *Carbon* **2011**, *49*, 966.

(35) Zhou, S.; Bongiorno, A. *Scientific Reports* **2013**, *3*, 2484.

(36) Kumar, P. V.; Bardhan, N. M.; Tongay, S.; Wu, J.; Belcher, A. M.; Grossman, J. C. *Nat Chem* **2014**, *6*, 151.

(37) Erickson, K.; Erni, R.; Lee, Z.; Alem, N.; Gannett, W.; Zettl, A. *Advanced Materials* **2010**, *22*, 4467.

(38) Devanathan, R.; Chase-Woods, D.; Shin, Y.; Gotthold, D. W. *Scientific Reports* **2016**, *6*.

(39) Talyzin, A. V.; Hausmaninger, T.; You, S. J.; Szabo, T. *Nanoscale* **2014**, *6*, 272.

(40) Wei, N.; Peng, X.; Xu, Z. *ACS Applied Materials & Interfaces* **2014**, *6*, 5877.

(41) Nair, R. R.; Wu, H. A.; Jayaram, P. N.; Grigorieva, I. V.; Geim, A. K. *Science* **2012**, *335*, 442.

CHAPTER 3

OXYGEN PLASMA ETCHED ULTRATHIN rGO MEMBRANE FOR NANOFILTRATION

3.1 ABSTRACT

We reported a novel procedure to fabricate ultrathin nanofiltration membrane by applying oxygen plasma treatment on multilayered reduced GO (rGO) membrane. The 5 nm thick multilayered graphene oxide based membrane was deposited through a layer-by-layer method, to overcome GO's inherent dispensability in the water environment and to lock the interlayer d-spacing at sub-nanometer scale, the membrane was thermally reduced under vacuum. Upon plasma etching, this non-permeative multilayered rGO membrane exhibited significantly improved water flux, but still demonstrated to keep the ability to block larger solutes, such as methylene blue and humic acid. By tuning the plasma treatment durations, the 5 nm rGO membrane achieved high flux (44 $L \cdot h^{-1} \cdot bar^{-1} \cdot m^{-2}$), high selectivity (98% rejection for MB), good antifouling ability and recovery capability. Our method, applying plasma etching on water tight multilayered rGO membrane, was proved to have more potential to prepare ultrathin GO-based nanofiltration membrane with high efficiency.

3.2 INTRODUCTION

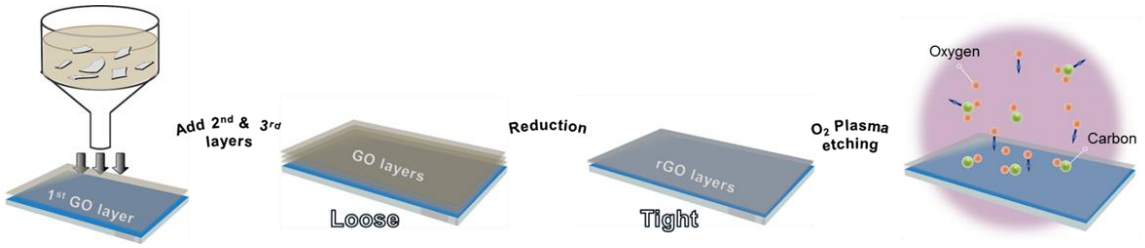

Figure 3.1 Schematic illustration of layer-by-layer method to prepared GO membrane, the membrane was reduced in the vacuum to obtain a tight layered structure, and then etched with oxygen plasma treatment.

Rapid industrialization and urbanization has made the shortage of clean water a worldwide issue[1]. Demand for clean water has forced us to develop highly efficient, cost-effective, and 'environmentally friendly' water treatment technologies[2,3]. Compared with 'traditional' water purification methods, such as distillation, chemical precipitation, or adsorption etc.[4,5], membrane-based water treatment technologies are not only more economic, but also being commercially demonstrated with high efficiency in removing salts and contaminants from water[6-8].

Graphene and it derivatives have attracted great attention and been considered as very promising membrane materials due to their good stability[9] and high mechanical strength[10], moreover, the atomically thin thickness and two-dimensional (2D) structure also makes it become possible to prepare thinnest membrane for high flux separation by graphene based materials.[11-14] Recently, one-atomic-thick nanoporous graphene brings in some new strategies in separation applications, computational studies have shown that nanoporous graphene could greatly improve the water permeability, and laboratory works have also demonstrated its potential in desalination and selective ionic transport.[15-20] However, the fabrication of nanoporous graphene in industrial scale remains a big

challenge. To date, large area of single layer graphene could be prepared through CVD growth, but creating isolated pores, preparing macroscopic graphene with sufficient densities and size controllable pores are essential for practical applications. Although techniques including ionic bombardment, e-beam lithography, plasma or UV-induced etching are proved to create small pores on graphene surface,[21-25] it's still challenging to scale on the graphene membranes for industrial use.

Herein, instead of etching on single layer graphene, apply post membrane fabrication treatments, such as oxygen plasma etching, on the ultrathin water tight multilayered reduced graphene oxide (rGO) membranes are studied as scalable alternative replacements for the one-atomic-thick nanoporous graphene membranes. The water tight ultrathin rGO membranes could be obtained by depositing large single layer GO flakes with average size around 1-2 μm through a layer-by-layer technique, and followed with thermal reduction in the vacuum (Figure 1). Therefore, the rGO membranes possess similar scalable manufacturability as the graphene oxide precursors. Since oxygen-containing functional groups are removed in a significant degree, the rGO membranes could retain tight layered structure in water environment.[26] In contrast, the GO membranes with "loose" structure are less stable in water due to the super hydrophilicity nature of graphene oxide.[27] Although the narrower interlayer spacing of rGO membranes leads to high transport resistance during the water separation process, applying etching treatments, such as oxygen plasma etching (Figure 1), could significantly improve the water permeability of the membranes.[28] Moreover, comparing with direct etching on single layer graphene, the top few layers of the ultrathin multilayered rGO membrane could work as protection layers to prevent over etching, which in turn bring the etching process with more control. In this

work, the effect of oxygen plasma treatment durations on the membrane permeability and separation performance were investigated. We found that, with exposed to plasma treatment for as long as 30 s, the ultrathin rGO membrane still achieved > 90% dye rejection, and high flux as 44 $L \cdot h^{-1} \cdot bar^{-1} \cdot m^{-2}$. Moreover, the ultrathin rGO membrane with optimized 10 s etching also exhibited good stability, antifouling ability and recovery capability after three cycles of fouling test.

3.3 EXPERIMENTAL

GO synthesize. Graphene oxide (GO) was synthesized by Hummers' method. Concentrated H_2SO_4 (69 mL) was slowly added into the mixture of graphite flakes (3.0 g, 1 equv.) and $NaNO_3$ (1.5 g, 0.5 equv.). After the mixture was cooled down to 0 ℃ in ice bath, $KMnO_4$ (9.0 g, 3.0 equv.) was added into the reaction mixture slowly to keep the mixture at a low temperature. The mixture was warmed up to 35 ℃ and kept stirring for 30 min. Then 138 mL D.I water was added into the reaction mixture, which produced large amount of heat and brought reaction temperature to 98 ℃. Maintained the reaction temperature at 98 ℃ for 2 hour and then slowly cooling it down with water bath. Additional 420 mL D.I water and 3 mL of H_2O_2 (30%) was added into the mixture, the black solid was collected by filtration after the mixture cool down to r.t. The final product was washed with 200 mL of water, 200 mL of 1N HCl and 200 mL of ethanol for two times, then dried under vacuum.

The large size (1-2 μm) single layer graphene oxide was exfoliated from as-synthesized GO through a Freeze−Thaw method. GO suspension with concentration of 2 mg/mL was prepared by dissolving 10 mg of as-synthesized GO in the centrifuge tube with 5 mL D.I water. Then soaked the centrifuge tube in liquid nitrogen bath for 30s. After the

GO suspension was completely frozen, transferred the centrifuge tube into water bath (60 ℃) and soaked for 30 min to completely thaw the suspension. Repeated this freeze-thaw procedure for six times and followed with centrifugation at 3,500 rpm for 25 min. The supernatant was collected to prepare single layer GO stock solution with concentration of 0.002 mg/mL.

The single-layer GO prepared by Freeze−Thaw method was characterized by AFM, XPS, XRD, Raman and FTIR.

Fabrication of membrane. The GO membrane was deposited on a commercial available anodized aluminum oxide (AAO) substrate through a layer-by-layer (LBL) filtration process. To theoretically cover the AAO substrate with an effective area of 10.5 cm^2, 1.07 μg of single layer GO was needed for each layer of deposition, the second layer of GO was deposited until the previous layer was completely dry. Upon fabrication, GO membranes were reduced in the vacuum at 220 ℃ for 12 hours. The ultrathin rGO membranes reported in this work were prepared through three steps of LBL deposition.

O_2 plasma treatments (UNITRONICS PE-50) were applied on the surface of the rGO membranes, different etching time intervals was used to study the effects of etching time on the flux and separation properties of rGO membrane.

Membrane Characterizations. X-ray diffraction (XRD) was employed to determine the d-spacing of GO and rGO membranes in dry/wet conditions. To dehydrate the membranes in the maximum degree, dry state GO and rGO membranes were kept in the vacuum for 24 hours, in contrary, wet state GO and rGO membranes were socked in D.I water for 24 hours. The XRD experiments were performed on a Rigaku D/Max 2100

powder X-ray diffractometer (Cu Kα radiation, data was collected at increments of 0.02 degrees, and an exposure time of 1.2 s/step in the angular range of 5-35 degree 2-theta at ambient temperature. The chemical structures of plasma etched rGO membranes were analyzed by a J Y Horiba LabRaman system using a 632 nm excitation laser. X-ray photoelectron spectroscopy (XPS) was employed to determine the surface chemistry of plasma etched rGO membrane by using monochromatic Al Kα source which operated at 15 keV and 120 W, and the pass energy was fixed at 40 eV for the detailed scans.

The surface morphologies of both rGO and 10 s O_2 plasma etched rGO membranes was observed by the field scanning electron microscopy (a Zeiss ultraplus). The thickness of rGO membrane reported in this work was confirmed by the cross-section SEM image. Water contact angles of rGO membranes with different time of etching were measured by using VCP optima system (Model: Optima XE). The detailed topography image of plasma etched rGO flakes were examined by TT-AFM system purchased from AFM workshop under vibration mode, the height distribution of the rGO flakes (corresponding to selective regains with size of 250×500 nm^2) were analyzed by Gwyddion 2.41.

Membrane Permeation Test. Pure water permeability and rejection performance of plasma etched rGO membranes were tested at 5 bar in a dead end system purchased from Sterlitech, the permeation area of the system was 19.6 mm^2. Pure water permeability was measured with D.I water. Methylene blue (MB) (6.4 mg/L), NaCl (10 mM), Na_2SO_4 (10 mM), $MgCl_2$ (10 mM), $MgSO_4$ (10 mM), and humic acid (30 ppm) rejections tests were performed to evaluate water purification performance of plasma etched rGO membranes, the feed solution was stirred at 500 rpm. Concentration of MB and humic acid in the collected permeate was analyzed using UV–vis spectrophotometer (Shimadzu UV-

1800). Concentration of NaCl, Na_2SO_4, $MgCl_2$, and $MgSO_4$ was measured by conductivity meter (Pour Grainger International, Lake Forest, IL, USA). The humic acid fouling tests were conducted in the same system by using 10 ppm feed solution, after each cycle of tests, the membrane was soaked in D.I with slow stirring for overnight.

3.4 RESULTS AND DISCUSSION

"Water Tight" Ultrathin rGO Membrane

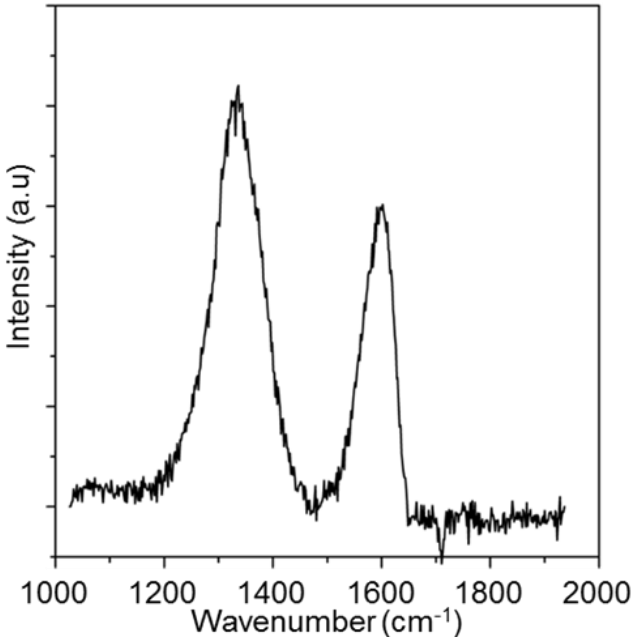

Figure 3.2 The Raman spectrum of as-synthesized graphene oxide

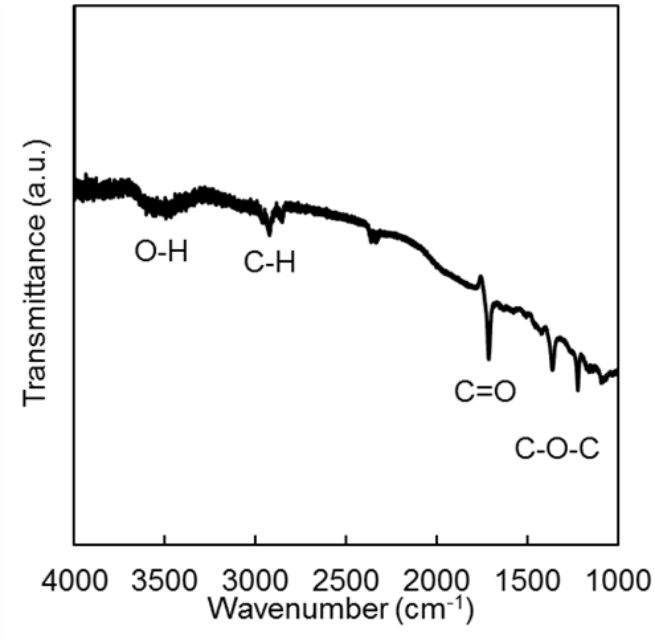

Figure 3.3 The FTRI spectrum of as-synthesized graphene oxide

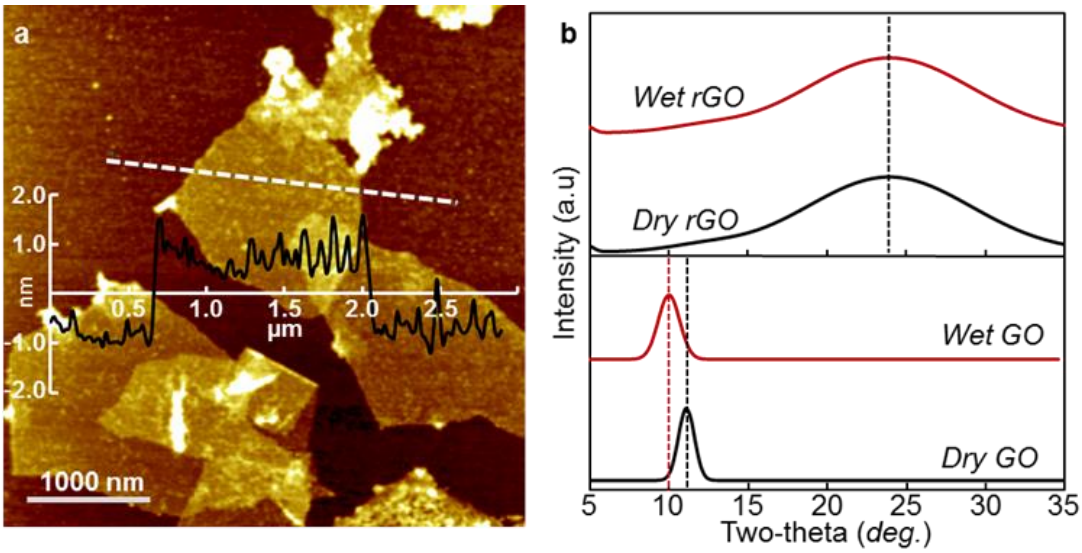

Figure 3.4 Characterization of GO flakes and GO/rGO membranes: (a) AFM image of single layer GO deposited on a mica substrate; (b) XRD patterns of GO/rGO membranes measured under dry and wet conditions.

Graphene oxide used in this work was synthesized by Hummers method,[29] the large size single layer GO (SLGO) flakes were exfoliated through the Freeze−Thaw technique.[30] The atomic force microscopy (AFM), shown in Figure 3.4a, confirms the single layer feature of the GO flakes with average size around 1-2 μm. The Raman spectrum (Figure 3.1) show a G peak at ~1590 cm^{-1} and a D peak at ~1350 cm^{-1}, which confirms the sp^2 hybridization of graphic carbon and distortion of carbon lattice respectively.[31,32] The as-prepared SLGO flakes exhibit characteristic FTIR peaks (Figure 3.2) of –C=O stretching at 1760 cm^{-1}, C-O-C stretching at 1220 cm^{-1}, and –OH stretching at 3500 cm^{-1}, which well correspond to the GO structure typically reported, and indicates the presence of unoxidized graphic carbon and various oxygen-containing groups on the GO flakes. The XPS date (Figure 3.5) show that about 49% of carbon is not oxidized, 41% have C-O bond, and 10% have C=O and COOH bonds.

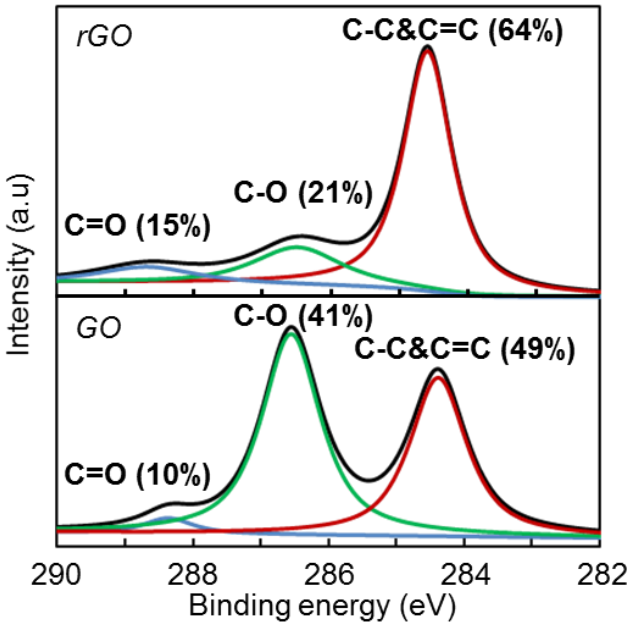

Figure 3.5 XPS C-1s spectrum of GO and rGO

When SLGO flakes stack on top of each other and form the lamellar structure, the oxygen containing functional groups, such as hydroxyl, epoxy and carbonyl groups act as spacers to keep distance of adjacent SLGO flakes, and due the strong hydrophilicity of these spacers, water can easily intercalate into GO layers and cause the swelling of GO membranes, which in turn reduce both selectivity and stability of the membranes for water purification.[27,33] The XRD patterns in Figure 3.4b show that the characteristic peak of dry GO membrane is located at 11.06 °, corresponding to a d-spacing of 7.8 Å; after soaked it in D.I water for 24 hours, the peak shift to 10.4 °and indicating the expansion of d-spacing to 8.9Å. However, reduction of GO membranes can help to "lock" the interlayer d-spacing and increase the membrane stability in water environment. As shown in Figure 3.4b, upon reducing at 220 ℃ in the vacuum for 12 hours, the d-spacing of reduced GO (rGO) membrane become 3.7 Å, and longtime humidification did not affect the d-spacing of rGO membrane, which suggests that the removal of oxygen containing groups through reduction (Figure 3.5) could shrink the interlayer d-spacing and exclude the water penetration into GO flakes, and it is possible to improve both selectivity and stability for rGO membranes in water environments.

Our previous study demonstrates that the structure GO membrane is greatly depends on its fabrication condition and slow deposition rate could lead to thermal dynamically favored interlayer nanostructure.[34] Therefore, in this work, a layer-by-layer membrane deposition method was developed to prepare membrane with stabilized structure. As shown in Figure 3.1, the vacuum filtration method was still used, but the membrane was deposited in layer by layer fashion, the 2nd and 3rd layer of GO was deposited as previous layer was totally dry. Through this method, the previous GO

layer/layers could significantly reduce deposition rate, made the GO flakes had enough time to assemble and form the thermal dynamically stabilized structure. Figure 3.6 indicates that, as GO deposition layer increasing, the pure water permeance of corresponding membrane decrease from 160.4 to 9.2 L h^{-1} bar^{-1} m^{-2}. After "locking" interlayer d-spacing of these membranes though thermal reduction, the pure water permeance significantly drop to 37.8 and 9.5 L h^{-1} bar^{-1} m^{-2} for one-layer and double-layer rGO membranes, respectively. For the triple-layer deposited rGO membrane, no water permeation was observed for the more than 24 hours under high pressure of 5 bar, which suggests that the triple-layer rGO membrane is "dense" enough to block the transport of water molecules and can be approximately treated as "water tight".

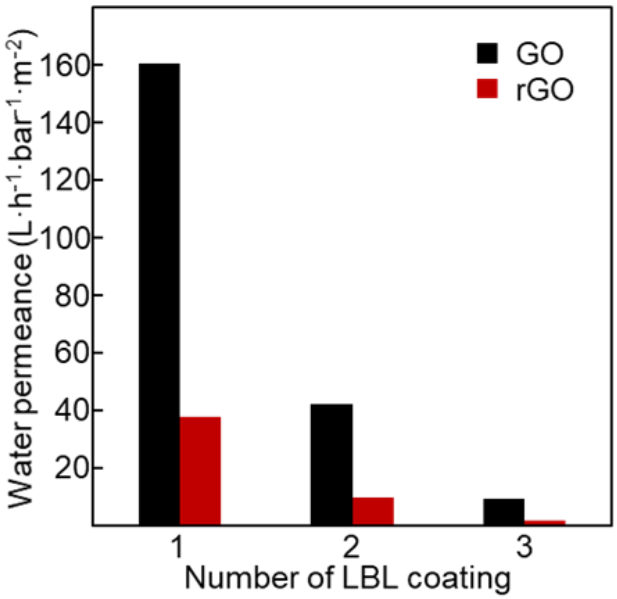

Figure 3.6 Water permeance of GO/rGO membranes with different layers of GO deposition.

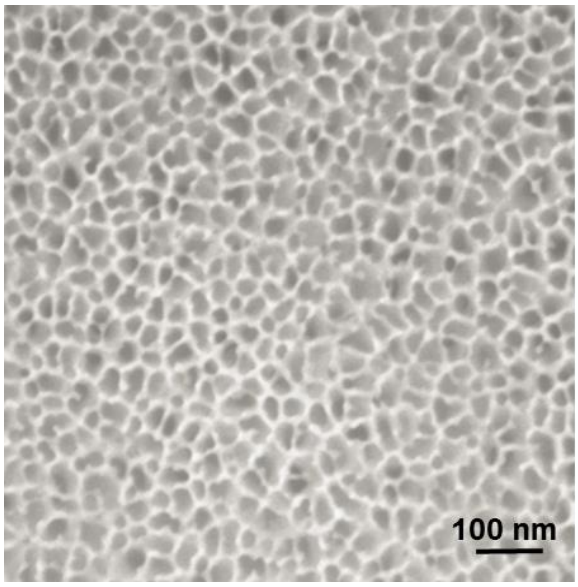

Figure 3.7 Morphology characterization of the AAO substrate

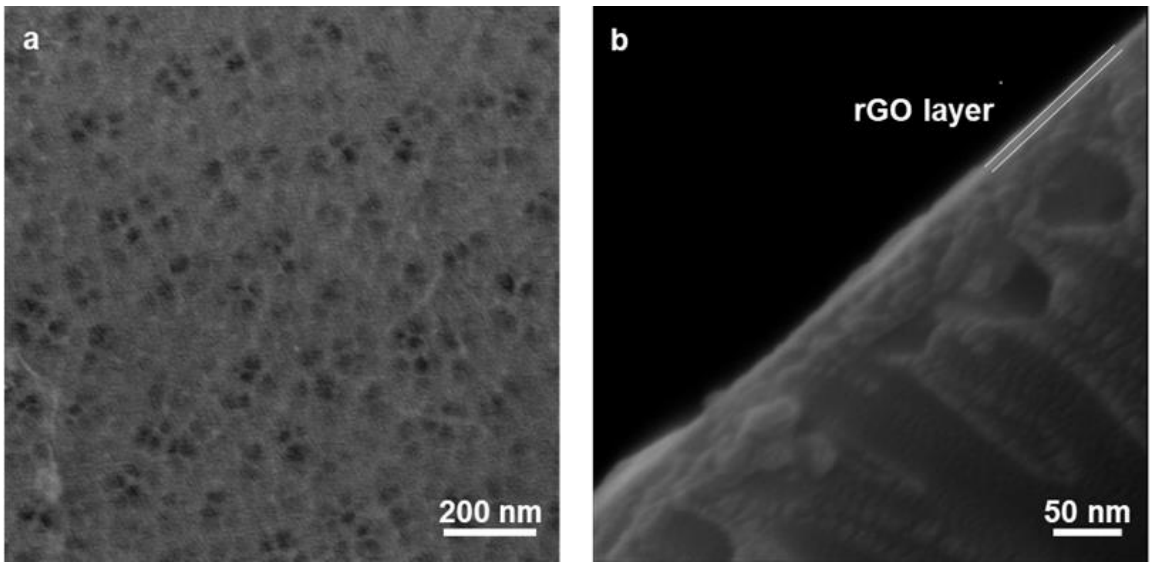

Figure 3.8 Morphology characterization of the triple-layer rGO: (a) FESEM of rGO membrane surface; (b) cross-sectional SEM image of rGO membrane.

FESEM was employed to examine the surface morphology of the "water tight" triple-layer rGO membrane, the as-prepared samples have pale black appearance indicative of a thin rGO layer. Comparing with the SEM image of bare AAO subtract (Figure 3.7), Figure 3.8a indicates that the surface of the rGO membrane is flat and smooth, and the rGO layer is thin enough that the substrate can still be observed, but the pores on AAO substrate are all well covered and no pin-hole is detected. The thickness of this as-prepared rGO membrane was determined from the cross-sectional SEM image (Figure 3.8b), which is about 5 nm. If suitable pores with size larger than water but smaller than solute particles could be further created by post treatments, such as plasma etching, UV-irradiation or ion bombardment, on the surface of this ultrathin membrane, it could exhibit great potential for high flux and high selectivity water purification.

Plasma Treatment on rGO Flake and rGO Membrane.

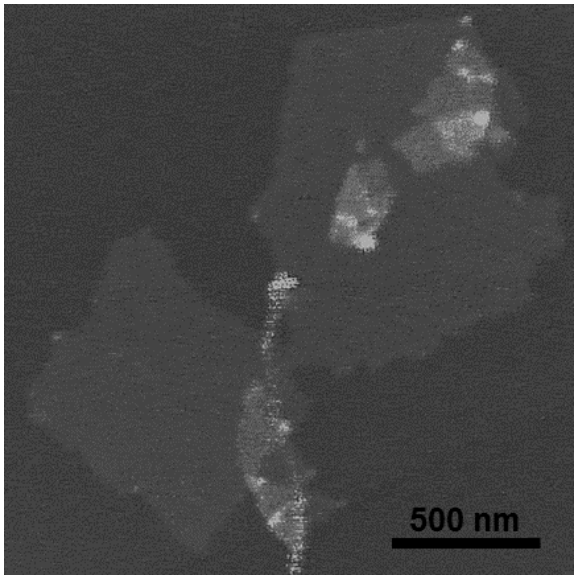

Figure 3.9 AFM images of rGO flakes without plasma treatment

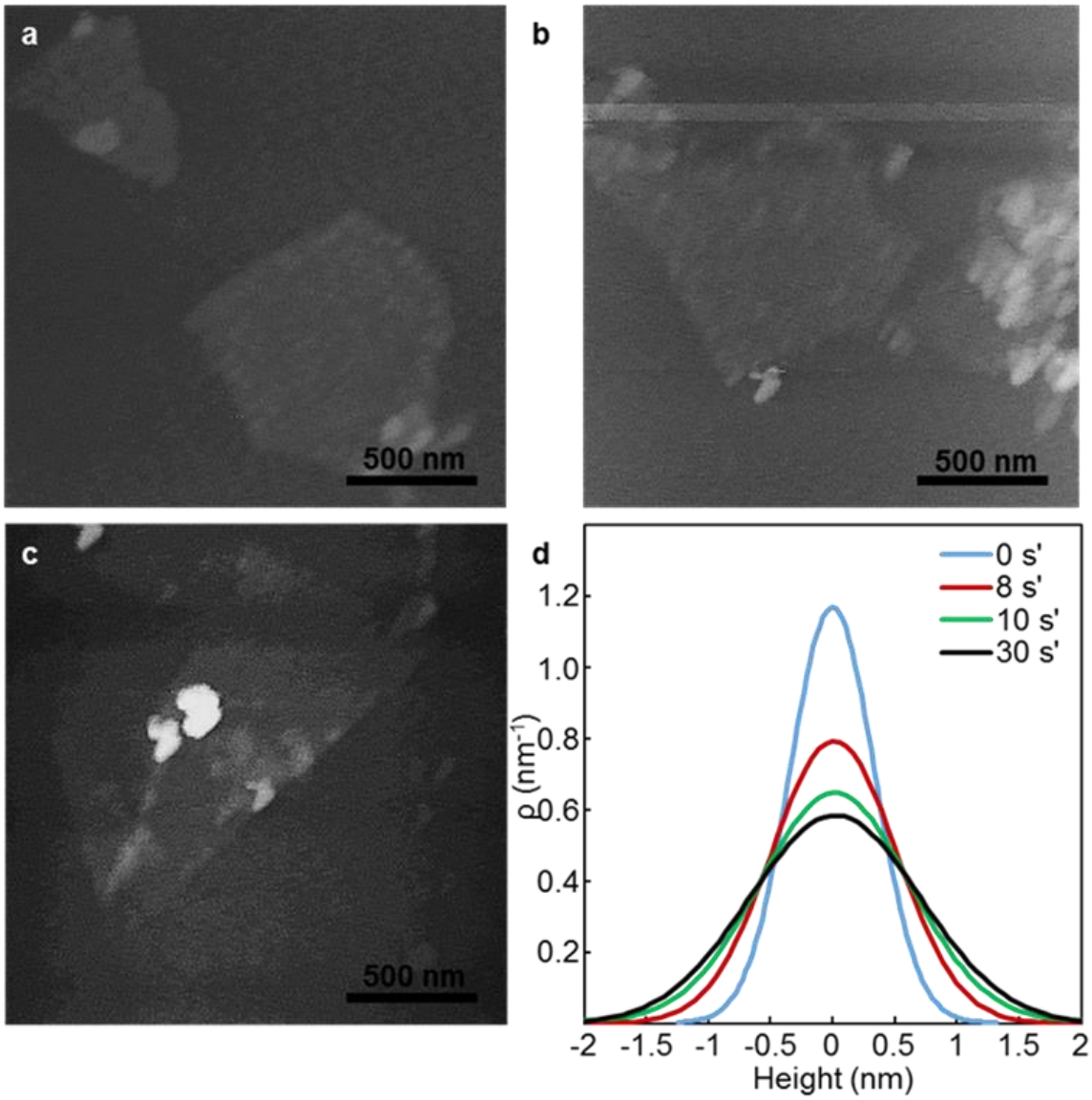

Figure 3.10 Topology evaluation of rGO flakes exposed to plasma etching for different times: (a), (b) and (c) AFM images of rGO flakes exposed to O_2 plasma treatment for 8, 10 and 30 s; (d) Height distributions for the rGO flakes exposed to plasma etching for different times. The solid line is the Gaussian fit of height distribution. To clarify the roughness difference between rGO flakes treated with different plasma etching conditions, the mean of the Gaussian fit was set as zero and the height distribution curve was shifted accordingly as well.

Herein, oxygen plasma etching was chosen as post fabrication treatment on the triple-layer rGO membrane, but before applied on the membrane, the effect of oxygen plasma treatment on individual rGO flakes investigated. Figure 3.9 shows the representative AFM image of rGO flakes without any plasma treatment, under this magnification, and the as-prepared rGO single layer flakes appear rather featureless and flat. Figure 3.10a-c illustrates the morphology evaluation of rGO flakes exposed to plasma etching for different times. Upon 8 s plasma exposure, no obvious changes were observed except the appearance of some rounded pits within the rGO flakes (Figure 3.10a). Subsequently, the pits tended to grow in number at longer time plasma exposure (Figure 3.10b). As plasma etching time elongated to 30 s, the etching pits seemed expand and made the rGO flakes less visible (Figure 3.10c). Another useful description of topological changes was shown through surface roughness,[35] the height distribution diagram of rGO flakes with different etching times is presented in Figure 3.10d, the Gaussian fit for the height distribution of the as-prepared rGO flake presents a full width at half maximum (FWHM) of 0.77 nm, as plasma treatment applied, the FWHM extends to 1.18 nm for 8 s etched rGO flakes, 1.42 nm for 10 s and 1.62 nm for 30 s etched rGO flakes, indicating the surface of rGO flakes became more and more rough when the plasma exposure duration increased. The incremental increase of surface roughness is due to the progressively increased small defects which created through the oxidation of the carbons of rGO flakes.[36]

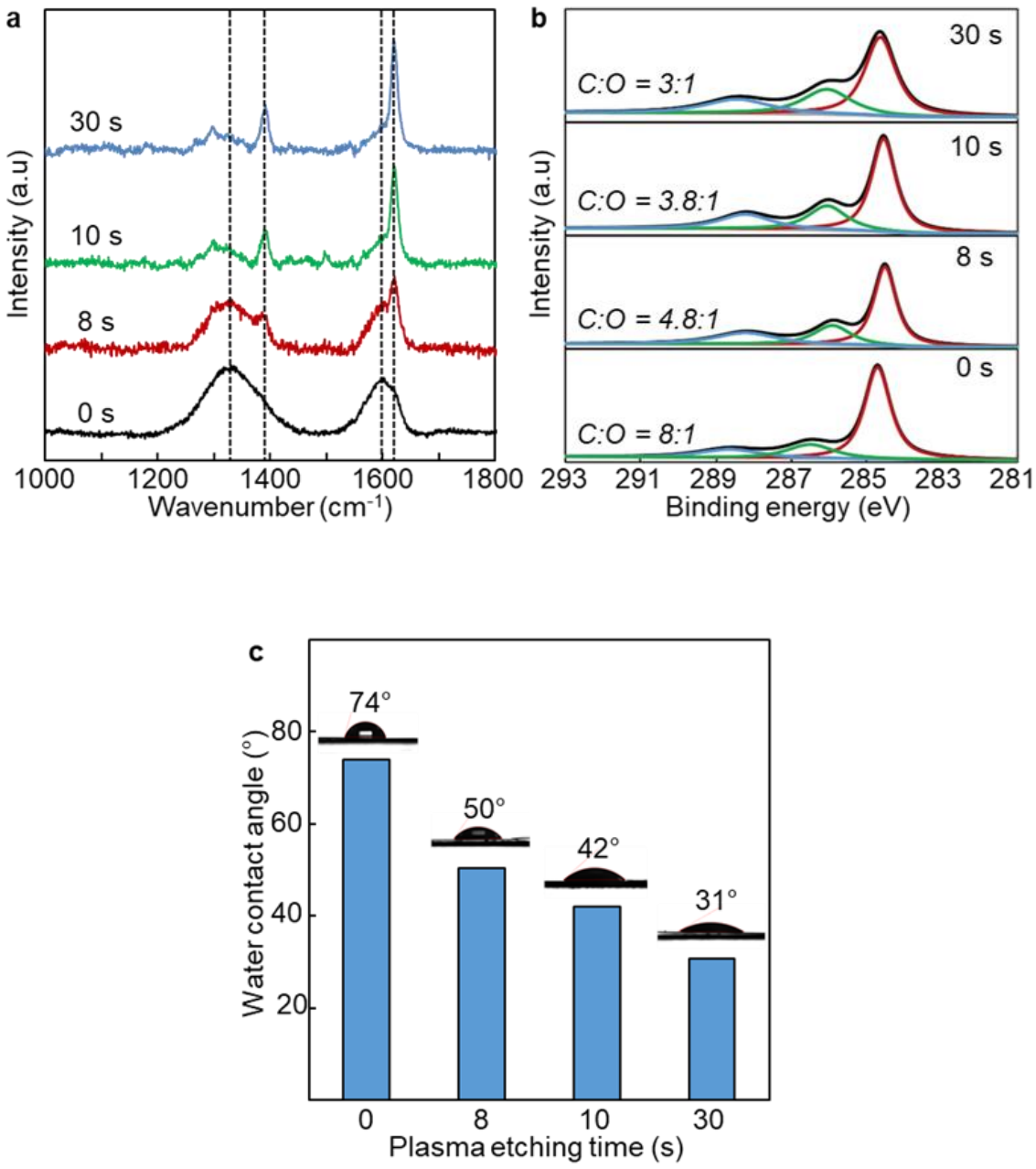

Figure 3.11Characterization of oxygen plasma etched triple-layer rGO membranes: (a) Raman spectra; (b) XPS C_1s spectra and (c) Water contact angle of rGO membranes etched under different O_2 plasma durations

A combination of Raman, XPS and water contact angle measurements were employed to characterize the effects of oxygen plasma etching on the chemical modification and surface hydrophilicity of the triple-layer rGO membrane. Figure 3.11a shows the Raman spectra of rGO membranes with oxygen plasma exposure time varied from 0-30 s, we found a new CH_2 (or CH_3) asymmetric vibration band located at ~1390 cm^{-1} and a D' band at ~1622 cm^{-1} was observed after 8 s of plasma treatment. With prolonged plasma etching duration of 10 s and 30 s, the intensity of CH_2 (or CH_3) and D' bands have become more significant, indicating the incremental sp^3 distortion of rGO flakes caused by the incorporation of oxygen-containing functional groups.[37,38] XPS measurements of oxygen plasma etched triple-layer rGO membranes were conducted to further clarify the influence of plasma etching duration on the elemental composition of the membranes (Figure 3.11b). Upon plasma treatment, the C/O atomic ratio decreased with increasing of etching duration, suggesting that the oxidation degree and the relative amount of attached oxygen-containing functional groups of the rGO membrane can be tuning by the plasma treatment. Moreover, the XPS results also consistent with the surface hydrophilicity of etched rGO membranes, as shown in Figure 3.11c, due to the incrementally introduced hydrophilic oxygen-containing functional groups, the water contact angle decreased as the etching time increased, therefore, the rGO membrane surface wettability was improved with oxygen plasma treatment.

Performance of Plasma Etched Triple-layer rGO Membrane

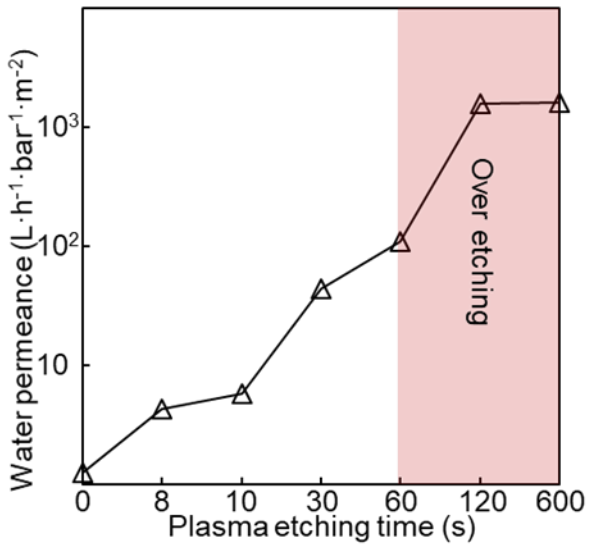

Figure 3.12 Pure water permeance of triple-layer rGO membrane exposed to different plasma etching time.

The pure water permeation test was first applied to study the transport characteristic of oxygen plasma etched triple-layer rGO membranes, the water permeance of rGO membranes with different plasma exposure time was measured and shown in Figure 3.12. After the triple-layer rGO membranes exposed to 8-30 s oxygen plasma treatment, the water permeance increases to 4.3-43.7 $L \cdot h^{-1} \cdot bar^{-1} \cdot m^{-2}$. However, with elongated plasma exposure, more than 1 min, the rGO layer of the membrane could be fully etched away since the corresponding membranes exhibited water flux close to bare AAO substrate. Therefore, to avoid over-etching of rGO layers, we kept the plasma treatment duration within 1 min.

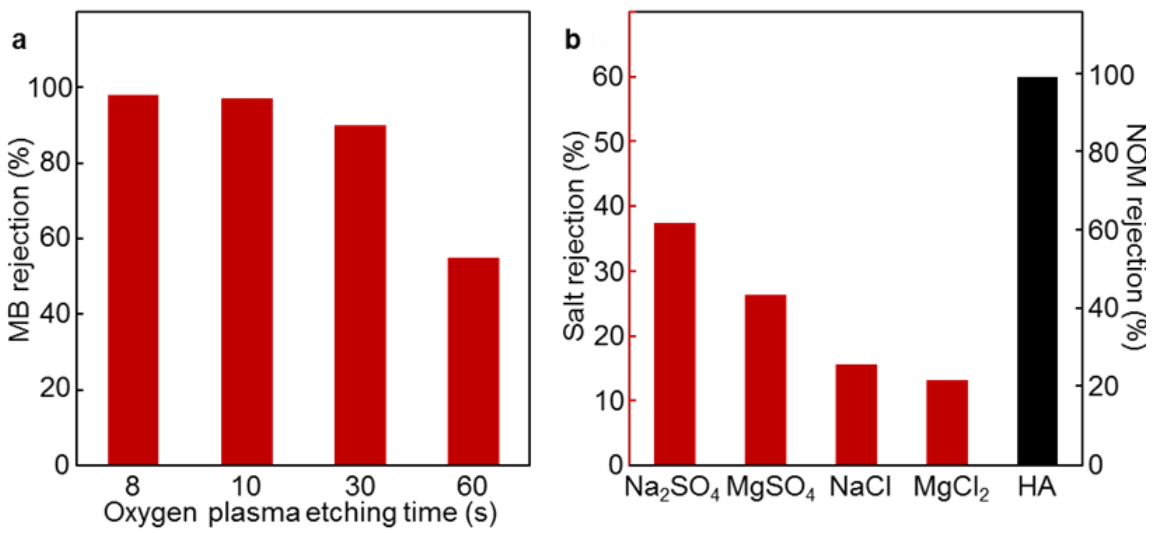

Figure 3.13 Separation performance for the O_2 Plasma Etched 5nm rGO Membrane: (a) Methylene blue (MB) rejection of rGO membranes exposed to different plasma treatment times; (b) Salts and nature organic matter (NOM) rejection of 10 s etched 5 nm rGO membrane (HA represents humic acid).

The separation performance of plasma etched triple-layer rGO membranes was examined by measuring the rejection for methylene blue (cationic dye, MW = 373.90 $g \cdot mol^{-1}$). As shown in Figure 3.13a, the 8 s etched rGO membrane exhibited a high rejection (98%) for MB after 2 h filtration. Up on 10 s plasma treatment, similar MB rejection (97%) was observed for the corresponding rGO membrane. After exposed to O_2 plasma for longer duration (30 s), the dye rejection slightly declined, but can still maintain 90% rejection for MB. However, the MB rejection was significantly dropped (50 %) while the rGO membrane had 60 s plasma exposure, which might due to the over etching of rGO layer. The dye separation performance suggests that when apply appropriate oxygen plasma treatment on the triple-layer rGO membrane surface, defects with size smaller than MB (0.7×1.6 nm) could be etched on the rGO layer,[39] which enable the non-permeative rGO membrane to obtain high water permeation (43.7 $L \cdot h^{-1} \cdot bar^{-1} \cdot m^{-2}$) and comparable high

organic dye rejection (more than 90%) at same time. Moreover, a nature organic matter (humic acid) and salt solutions were used to further demonstrate the nanofiltration characteristic of the chosen 10 s O_2 plasma etched rGO membrane (Figure 3.13b). The 10 s etched rGO membrane exhibited high rejection for humic acid (100%) and decent rejection for $NaSO_4$ (38%). Ascribed to the slight negatively charged membrane surface and Donnan exclusion theory, the rejection for these salts follows the order of Na_2SO_4 > $MgSO_4$ > NaCl > $MgCl_2$ since divalent co-ions have greater repulsive force than monovalent co-ions.[39,40]

To demonstrate the natural organic matter (NOM) antifouling ability for the O_2 plasam etched rGO membrane, the humic acid (10 ppm) fouling test was coducted by using the 10 s etched rGO memrbane. Normalized flux, which defined as the measured permeation flux at different water recovery divided by the initial flux in the first cycle, was used to evalute the anitifouling performance and recovery capability.[39] Figure 3.14 shows that, during the first cycle, after collect 10.5 mL of permeate (35% water recovery), the flux dropped by only 38%, similar trends were observed in the second and third cycles of the fouling tests. By cleaning in D.I water with stirring for 12 h when each filtation cycle was done, the 10 s etched membane exhibited a comparative flux recovery capability (75-88%) to the reported polysulfone nanofiltration membrane. Further more, during each cycle of tests, the 10 s rGO memrbane also showed around 100 % rejction for humic acid. Therefore, according to the results of the humic acid fouling test, the 10 s rGO membrane presents both high rejection and good anitfouling ability for natural organic matters.

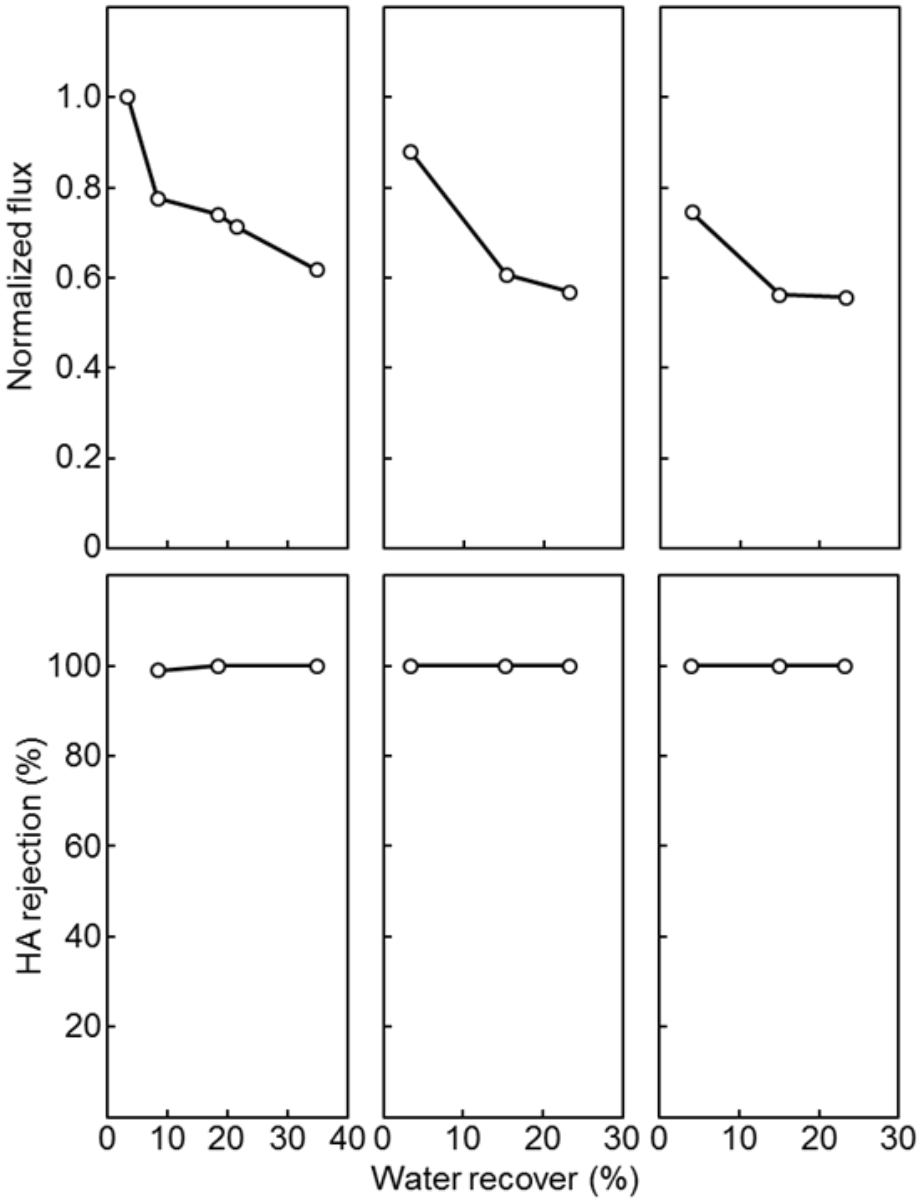

Figure 3.14 Three filtration cycles of humic acid on 10s etched rGO membrane: flux decline (first row) and NOM removal for the corresponding cycle (second row).

3.5 CONCLUSION

In conclusion, an hihg efficent ultrathin nanofiltation membrane was obatiend by applying post fabircation etching treatment on the triple-alyer rGO membrane. This “water tight” rGO memrbane was prepared by a layer-by-layer depsotion method and followed with thermal reduction which not only “lock” the membrnae interlayer d-spacing at sub-nanometer scale but also prevent the peratration of water moleaucles. Upon introducing appropriate oxygen plasma etching, the water permeation of the triple-layer rGO membrane was dramatically facilitated, but the etched rGO membrane still exhibited hihg efficiency in blocking large solute molecules, such as orgainc dye and nature organic matter. By tuning the plasma treatment time, the triple-layer rGO membranes achieved ~98% rejection for MB and pure water flux as high as about 44 $L \cdot h^{-1} \cdot bar^{-1} \cdot m^{-2}$. Moreover, the plasma etched triple-layer rGO membrane also demonstrated good antifouling perforamcne and recovery capability. Comparing with direct etching on the single layer graphene memrbane, plasma etching on multilayered rGO membrane could be applied with more control and scability . We expect our finding can eventually lead to novel design of ultrathin GO-based nanoflitration membranes with high flux and selecivity.

REFERENCE

(1) Vorosmarty, C. J.; McIntyre, P. B.; Gessner, M. O.; Dudgeon, D.; Prusevich, A.; Green, P.; Glidden, S.; Bunn, S. E.; Sullivan, C. A.; Liermann, C. R.; Davies, P. M. *Nature* **2010**, *468*, 334.

(2) Shannon, M. A.; Bohn, P. W.; Elimelech, M.; Georgiadis, J. G.; Marinas, B. J.; Mayes, A. M. *Nature* **2008**, *452*, 301.

(3) Elimelech, M. *Journal of Water Supply Research and Technology-Aqua* **2006**, *55*, 3.

(4) Fu, F. L.; Wang, Q. *Journal of Environmental Management* **2011**, *92*, 407.

(5) Chakraborti, D.; Rahman, M. M.; Das, B.; Murrill, M.; Dey, S.; Mukherjee, S. C.; Dhar, R. K.; Biswas, B. K.; Chowdhury, U. K.; Roy, S.; Sorif, S.; Selim, M.; Rahman, M.; Quamruzzaman, Q. *Water Res.* **2010**, *44*, 5789.

(6) Kimura, K.; Toshima, S.; Amy, G.; Watanabe, Y. *J Membrane Sci* **2004**, *245*, 71.

(7) Comerton, A. M.; Andrews, R. C.; Bagley, D. M.; Hao, C. Y. *J Membrane Sci* **2008**, *313*, 323.

(8) Basile, T.; Petrella, A.; Petrella, M.; Boghetich, G.; Petruzzelli, V.; Colasuonno, S.; Petruzzelli, D. *Industrial & Engineering Chemistry Research* **2011**, *50*, 8389.

(9) Dikin, D. A.; Stankovich, S.; Zimney, E. J.; Piner, R. D.; Dommett, G. H. B.; Evmenenko, G.; Nguyen, S. T.; Ruoff, R. S. *Nature* **2007**, *448*, 457.

(10) Lee, C.; Wei, X. D.; Kysar, J. W.; Hone, J. *Science* **2008**, *321*, 385.

(11) Geim, A. K.; Novoselov, K. S. *Nat Mater* **2007**, *6*, 183.

(12) Geim, A. K. *Science* **2009**, *324*, 1530.

(13) Dreyer, D. R.; Park, S.; Bielawski, C. W.; Ruoff, R. S. *Chem Soc Rev* **2010**, *39*, 228.

(14) Fathizadeh, M.; Xu, W. W. L.; Zhou, F. L.; Yoon, Y.; Yu, M. *Adv Mater Interfaces* **2017**, *4*.

(15) Konatham, D.; Yu, J.; Ho, T. A.; Striolo, A. *Langmuir* **2013**, *29*, 11884.

(16) Lin, L. C.; Grossman, J. C. *Nat Commun* **2015**, *6*.

(17) Rollings, R. C.; Kuan, A. T.; Golovchenko, J. A. *Nat Commun* **2016**, *7*.

(18) Wang, Y. H.; He, Z. J.; Gupta, K. M.; Shi, Q.; Lu, R. F. *Carbon* **2017**, *116*, 120.

(19) O'Hern, S. C.; Stewart, C. A.; Boutilier, M. S. H.; Idrobo, J. C.; Bhaviripudi, S.; Das, S. K.; Kong, J.; Laoui, T.; Atieh, M.; Karnik, R. *Acs Nano* **2012**, *6*, 10130.

(20) Robertson, A. W.; Lee, G. D.; He, K.; Gong, C. C.; Chen, Q.; Yoon, E.; Kirkland, A. I.; Warner, J. H. *Acs Nano* **2015**, *9*, 11599.

(21) O'Hern, S. C.; Boutilier, M. S. H.; Idrobo, J. C.; Song, Y.; Kong, J.; Laoui, T.; Atieh, M.; Karnik, R. *Nano Lett* **2014**, *14*, 1234.

(22) Boutilier, M. S. H.; Sun, C. Z.; O'Hern, S. C.; Au, H.; Hadjiconstantinou, N. G.; Karnik, R. *Acs Nano* **2014**, *8*, 841.

(23) Surwade, S. P.; Smirnov, S. N.; Vlassiouk, I. V.; Unocic, R. R.; Veith, G. M.; Dai, S.; Mahurin, S. M. *Nat Nanotechnol* **2016**, *11*, 995.

(24) Wang, L.; Williams, C. M.; Boutilier, M. S. H.; Kidambi, P. R.; Karnik, R. *Nano Lett* **2017**, *17*, 3081.

(25) Liu, L.; Xie, D. L.; Wu, M. H.; Yang, X. X.; Xu, Z.; Wang, W. L.; Bai, X. D.; Wang, E. G. *Carbon* **2012**, *50*, 3039.

(26) Liu, H. Y.; Wang, H. T.; Zhang, X. W. *Adv Mater* **2015**, *27*, 249.

(27) Zheng, S. X.; Tu, Q. S.; Urban, J. J.; Li, S. F.; Mi, B. X. *Acs Nano* **2017**, *11*, 6440.

(28) Harpale, A.; Chew, H. B. *Carbon* **2017**, *117*, 82.

(29) Marcano, D. C.; Kosynkin, D. V.; Berlin, J. M.; Sinitskii, A.; Sun, Z. Z.; Slesarev, A.; Alemany, L. B.; Lu, W.; Tour, J. M. *Acs Nano* **2010**, *4*, 4806.

(30) Ogino, I.; Yokoyama, Y.; Iwamura, S.; Mukai, S. R. *Chem Mater* **2014**, *26*, 3334.

(31) Ferrari, A. C.; Robertson, J. *Physical Review B* **2000**, *61*, 14095.

(32) Graf, D.; Molitor, F.; Ensslin, K.; Stampfer, C.; Jungen, A.; Hierold, C.; Wirtz, L. *Nano Lett.* **2007**, *7*, 238.

(33) Joshi, R. K.; Carbone, P.; Wang, F. C.; Kravets, V. G.; Su, Y.; Grigorieva, I. V.; Wu, H. A.; Geim, A. K.; Nair, R. R. *Science* **2014**, *343*, 752.

(34) Xu, W. W. L.; Fang, C.; Zhou, F. L.; Song, Z. N.; Liu, Q. L.; Qiao, R.; Yu, M. *Nano Lett* **2017**, *17*, 2928.

(35) Rezania, B.; Severin, N.; Talyzin, A. V.; Rabe, J. P. *Nano Lett* **2014**, *14*, 3993.

(36) Solis-Fernandez, P.; Paredes, J. I.; Villar-Rodil, S.; Guardia, L.; Fernandez-Merino, M. J.; Dobrik, G.; Biro, L. P.; Martinez-Alonso, A.; Tascon, J. M. D. *J Phys Chem C* **2011**, *115*, 7956.

(37) Dresselhaus, M. S.; Jorio, A.; Souza, A. G.; Saito, R. *Philos T R Soc A* **2010**, *368*, 5355.

(38) Yang, R.; Shi, Z. W.; Zhang, L. C.; Shi, D. X.; Zhang, G. Y. *Nano Lett* **2011**, *11*, 4083.

(39) Song, Z. N.; Fathizadeh, M.; Huang, Y.; Chu, K. H.; Yoon, Y. M.; Wang, L.; Xu, W. W. L.; Yu, M. *J Membrane Sci* **2016**, *510*, 72.

(40) Han, Y.; Xu, Z.; Gao, C. *Adv Funct Mater* **2013**, *23*, 3693.

CHAPTER 4

WATER PERMEATION THROUGH STRUCTURAL DEFECTS OF SINGLE-LAYERED GRAPHENE OXIDE MEMBRANES

4.1 ABSTRACT

Comparing with traditional methods, membrane-based water treatment technologies are essential due to the low energy consumption and high efficiency in removing contaminants or salts. As the flux cross the membrane decreases with membrane thickness, to balance the pay off between permeability and selectivity, membrane should possess pores large enough to allow the passage of water molecules but small enough to block the large solutes, and the membrane thickness should be as thin as possible to provide high flux, which makes the "ideal" membrane might be in the form of one atomic thickness and with suitable pores. Materials like graphene oxide, which has both carbon atom thickness and nature surface defects, just meets this requirement and have been considered as a promising candidate to prepare ultrathin membranes which mostly closing to the "ideal" state. However, due to the fact that the oxidation degree of graphene oxide is strongly depends on its synthesis conditions, and the weight of graphene oxide is hard to be exactly weighed because of its super hydrophilic nature, it's difficult to prepare a single layer GO membrane through a quantitative way. But herein, by clarifying two distinct water transportation mechanisms for membranes with sub-monolayer and multilayer GO

coverage, a generic methodology to fabricate nominal single-layered GO membrane was proposed for the first time. The Water flux exhibited a transition from linear to exponential decrease as the GO coverage increase, the condition to prepare nominal single-layered GO membrane could be extrapolated from the turning point of the transition, the as-fabricated membrane which with thickness closing to one-carbon-atom exhibits high water permeance around 64 $L \cdot m^{-2} \cdot h^{-1} \cdot bar^{-1}$, and defects on GO flakes provide major contribution for the membrane sieving property. By evaluating the separation performance of this membrane with rigid molecules, the effective defect size of GO was determined to be ~1.2-1.7 nm. This membrane with nominal single-layer GO cover also show great potential in the separation of large molecules such as proteins.

4.2 INTRODUCTION

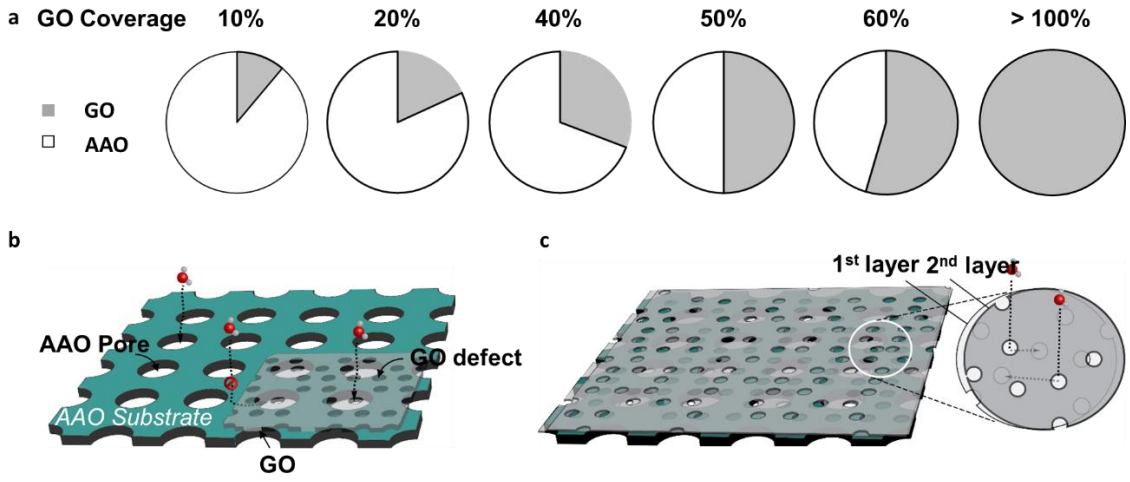

Figure 4.1 Schematic view for theoretical GO coverage (a) and possible water permeation route (b) while AAO substrate was covered by less than one layer of GO and (c) more than one layer of GO.

Graphene-based material, such as graphene and graphene oxide (GO), has been considered as a very promising membrane material due to its good stability[1,2] and high mechanical strength[3]. The two-dimensional nature and only one carbon atom thickness also makes it become possible to prepare thinnest membrane for high flux separation by using this material. Following the pioneering work on unimpeded water permeation through GO membranes by Nair et al.,[4] many studies have been conducted to explore the potential of layered GO membranes for water purification.[5,6,7] In these studies, GO or partially reduced GO sheets/flakes were packed together or grafted layer by layer via chemical bonds, and interlayer spacing was the primary water permeation pathway.[8-12] For these as-reported membranes, albeit high rejection (>99%) for large organic dye molecules could be obtained, salt rejection was still low due to nanometer-sized interlayer spacing and the swelling of the membrane. More importantly, low water flux, which caused by the relative large thickness, impeded the separation efficiency of these membranes.

To effectively utilize atomically thin graphene-based sheets for high flux water purification, a few layer thin, graphene-based membranes with direct-through, nanometer-sized structural defects are highly desired. Recently, although it has been demonstrated both theoretically, and experimentally that the porous single layer graphene membrane has great potential for gas mixture separation and desalination[13-22], due to the lack of clear understanding and control of structural defects, it is highly challenging to fabricate single graphene base membranes with desired pores for industrial scale separation applications. However, the single-layer graphene oxide membrane can work as an alternative replacement for the one-atomic-thick nanoporous graphene membrane because of its high scalability and natural porosity which created during its synthesis step. But the only

challenge is it's difficult to prepare a single layer GO membrane through a quantitative way, since the oxidation degree of graphene oxide is strongly depends on its synthesis conditions, and the weight of graphene oxide is hard to be exactly weighed because of its super hydrophilic nature.

Herein, by correlating the water permeability of membranes with GO coverage, we extrapolated the condition to deposit single layer of GO, and methodology we developed in this study could be applied in a generic way to fabricate nominal single-layered GO membranes by using GO with different oxidation degrees. As shown in Figure 4.1, we proposed two different water permeation mechanisms for membranes with sub-monolayer (Figure 4.1b) and multilayer GO coverage (Figure 4.1c). When porous substrate is not totally covered by GO, the water permeability of corresponding membrane should linearly decrease with the increasing of GO coverage, in contrary, under the multilayer coverage model, the overlapping of GO defects could make water permeability drop in an exponential fashion. To prove this concept and to investigate these two different water permeation mechanisms through GO defects, series of ultrathin membranes with different GO coverage were prepared (Figure 4.1a) and their water flux was measured respectively. By finding the linear-exponential turning point of pure water permeability, we determined the condition for the approximate single layer GO deposition, and prepared the membrane with thickness closing to one layer of GO coverage accordingly. And since the structurer defects play the main role for the separation characteristic of the membrane fabricated in this condition, the effective size of GO defects were estimated through evaluating the membrane separation performance. Besides that, for the first time, a physical water permeation model through GO defects was built based on experimental data, and we

believe such a fundamental research could lead to a more rational design of nanoporous graphene-based membranes toward water purifications.

4.3 EXPERIMENTAL

All chemicals were purchased from Sigma-Aldrich or VWR and used without further purification. Raman spectra were recorded with a J Y Horiba LabRam system using a 632 nm excitation laser. The powder X-ray diffraction experiments were performed on a Rigaku D/Max 2100 Powder X-ray Diffractometer (Cu Kα radiation), and the experiments were run using a zero background slide on which the graphene oxide film was gently pressed. XPS was conducted using a Kratos AXIS Ultra DLD XPS system, which was equipped with a monochromatic Al Kα source. The monochromatic Al Kα source was operated at 15 keV and 120 W, and the pass energy was fixed at 40 eV for the detailed scans. The binding energy was calibrated using an Ag foil with Ag3d5/2 set at 368.21 ± 0.025 eV for the monochromatic Al X-ray source.

GO synthesize

Graphene oxide was synthesized by Hummers' method. Concentrated H2SO4 (69 mL) was slowly added into the mixture of graphite flakes (3.0 g, 1 equv.) and NaNO3 (1.5 g, 0.5 equv.). After the mixture was cooled down to 0 ℃ in ice bath, KMnO4 (9.0 g, 3.0 equv.) was added into the reaction mixture slowly to keep the mixture at a low temperature. The mixture was warmed up to 35 ℃ and kept stirring for 30 min. Then 138 mL D.I water was added into the reaction mixture, which produced large amount of heat and brought reaction temperature to 98 ℃. Maintained the reaction temperature at 98 ℃ for 2 hour and then slowly cooling it down with water bath. Additional 420 mL D.I water and 3 mL of

H2O2 (30%) was added into the mixture, the black solid was collected by filtration after the mixture cool down to r.t. The final product was washed with 200 mL of water, 200 mL of 1N HCl and 200 mL of ethanol for two times, then dried under vacuum.

Dispersion (1mg/mL) of as-prepared graphene oxide was sonicated for 1 hour and followed by centrifugation at 10,000 rpm for 30 min. The supernatant was collected and the sediment was re-dispersed in water, repeated this procedure for several times and collected all the supernatant, the single-layer graphene oxide was obtained by drying supernatant under vacuum.

Fabrication of membrane

The extremely diluted graphene oxide dispersion was prepared by dispersing certain amount of GO in 250 mL D.I. water and followed by 10 min sonication. The membrane was deposited through a simple vacuum filtration process on a commercial available anodized aluminum oxide (AAO) substrate which has effective area of 10.5 cm2. To fabricate membrane with different degree of GO coverage and thickness, a series of diluted GO dispersion were prepared with concentration arranged from 0.00077 to 0.031 μg/mL. For instance, by assuming GO has same density as graphene, to theoretically cover 10% area of 10.5 cm2 AAO substrate, 250 mL single layer GO dispersion with concentration of 0.00077 μg/mL was needed to be filtered through. Based on same idea, to cover AAO substrate with theoretical calculated 4 nm thick GO layer, concentration of GO dispersion should increase to 0.031 μg/mL. Upon fabrication, all membranes were dried in the vacuum at r.t for 12 hours before use. The rGO membrane was fabricated by reducing corresponding GO membrane in the vacuum at 220 ℃ for 12 hours.

Measurement of pure water flux

Pure water flux of GO membranes (GOMs) were measured on a dead end system purchased from Sterlitech and driven by N2 gas. The permeation area of the system was 19.6 mm2, and the chosen sample was fixed at the bottom of water tank. The driving pressure for membranes with more than 40% GO coverage was fixed to 5 bar; for bare AAO, and membranes with only 10% and 20% GO coverage, applied pressure was adjusted to 1 bar. The water flux can be obtained by measuring the mass of water collected for certain time under certain pressure.

Calibration of GO defect size

The size of GO defects was estimated by evaluating the separation performance of the membrane which close to mono layer GO coverage (~1.4 layer, extra 40% of GO was applied to make sure no exposed AAO area was left). In this case, the influence of interlayer spacing was negligible and the GO defects were assumed to play the only factor for the membrane sieving performance. Molecules and particles with size arranged from 0.6-3.2 nm were selected to calibrate the GO defects: sucrose (0.6 × 0.72 × 1.06 nm), γ-cyclodextrin (1.2 nm), Evans blue (1.2 × 3.1 nm), TMpyP (1.7 × 1.7 nm) and Au Nps (3.2 nm). The separation tests were performed on the same dead end system for water flux measurement, and 25 mL of diluted solution of chosen molecule or particle was filtered through this single layer GO membrane. After certain time, 2 mL of permeance was collected and monitored by TOC or UV-vis, correspondingly, to evaluate the rejection. Dimension of the cut-off molecule should represent the size of GO defects.

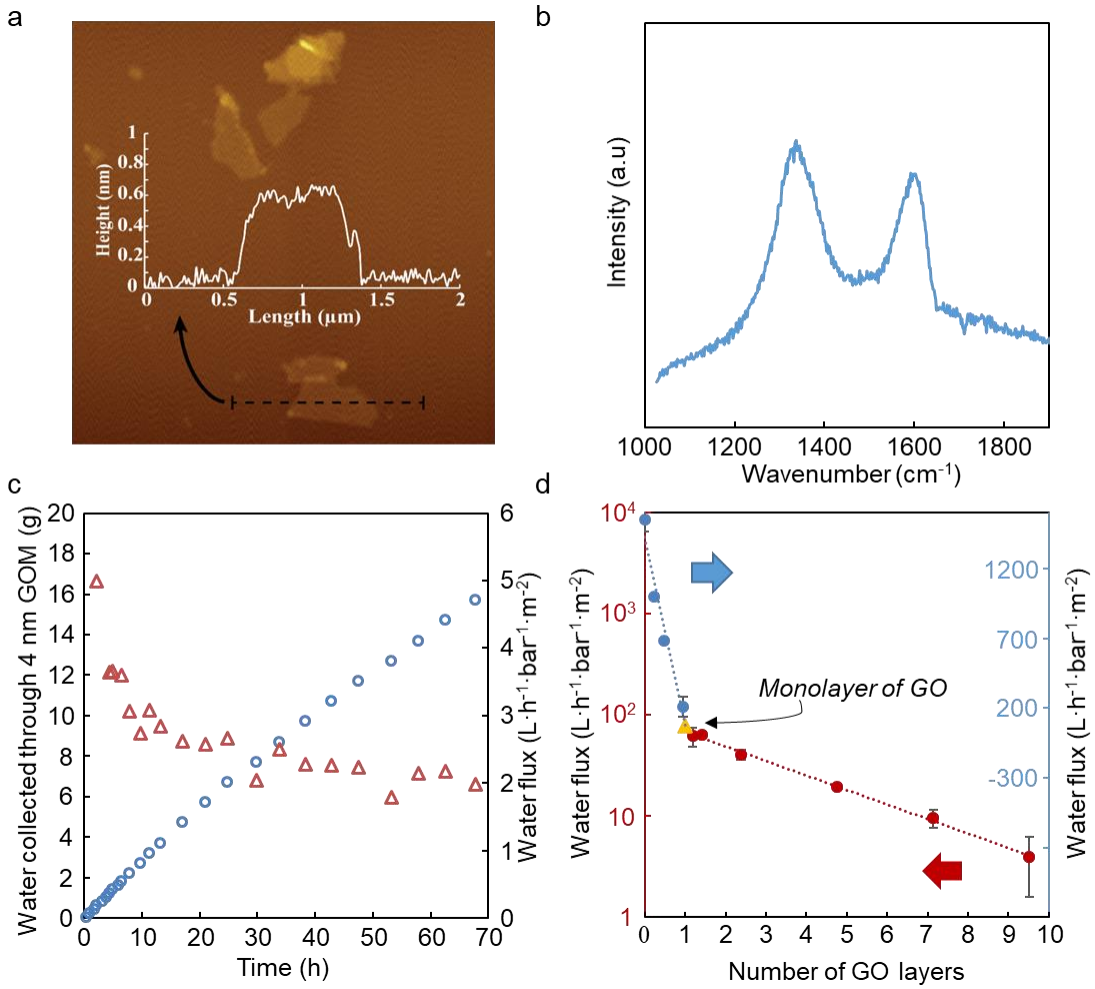

Figure 4.2. (a) AFM image of single layer GO deposited on a mica substrate; inset shows the height profile of a GO flake; (b) Raman spectrum of graphene oxide; (c) Water flux of GO membrane with theoretical calculated 4 layers of GO coverage; (d) Water flux of membranes with different degrees of calibrated GO coverage. (blue circles represent membranes with GO coverage less than 100%; red circles represent membranes have more than one layer of GO coverage; yellow triangle represent the extrapolated position which membrane just covered with one layer of GO.)

Water permeation performance.

In this study, the graphene oxide was synthesized through a Hummers' method, as illustrated in Figure 4.2a, the as-prepared graphene oxide exhibit a single layer feature with thickness about 0.7 nm, and average size of the single layer GO is in the range of 500 nm

to 1 μm. Figure 4.2b exhibited the Raman spectrum which measured under the excitation energy $\boldsymbol{E_L}$ of 1.96 eV, the spectrum shown a G peak at ~1590 cm^{-1} and a D peak at ~1350 cm^{-1}, the I_D/I_G peak intensity ratio was calculated to be 1.39, which assigned to lower disorder (less defects) in the graphitized structure of as-prepared GO. According to Ferrari et al's work, on the low-defect regime of graphene, where the distance between point-like defects ($\boldsymbol{L_D}$) was defined larger than 10 nm, an equation $L_D^2(nm^2) = \frac{(4.3\pm1.3)\times10^3}{E_L^4}(\frac{I_D}{I_G})^{-1}$ could be developed to correlate the I_D/I_G ratio with $\boldsymbol{L_D}$. By assuming the dependence of I_D/I_G on $\boldsymbol{L_D}$ could also be applied on graphene oxide, the distance of defects ($\boldsymbol{L_D}$) on our single layer GO was calculated between 12.1 to 16.5 nm. The defects density $\boldsymbol{\rho_{def}}$ (m^{-2}), which determined by $\rho_{def} = \frac{10^{18}}{\sqrt{\pi\times L_D^2}}$, was in the range of 3.42×10^{16} to 4.67×10^{16}.

The GO membrane was prepared via a vacuum filtration process, anodized aluminum oxide (AAO) nanoporous substrate was applied as support for the membrane, GO coverage on AAO substrates was adjusted by tuning the concentration of GO dispersion to be filtrated (see detail in experimental section). To investigate the mechanism of water transportation in the ultrathin GO membrane, the pure water permeability of a series of membranes which with theoretically calculated 10% coverage to 4 layers of GO was measured on a dead-end system, and the driving pressure was adjusted accordingly from 1 to 5 bar. Figure 4.2c exhibited the water permeation detail of GO membrane with theoretical 4 layers of GO coverage, under fixed operation pressure (5 bar) and effective permeation area (19.6 mm^2), the water permeability of the corresponding membrane can be estimated by the tangent line of the permeation curve (right axis). As illustrated in Figure 4.2c (left axis), water permeability was progressively decreased and stabilized after 30

hours of performance, and the equilibrium water permeability was about 2.41 $L.m^{-2}.h^{-1}.bar^{-1}$.

Table 4.1 Pure water permeability of membranes with different degree of theoretically calculated GO coverage

GO coverage	Percentage of GO covered area [a]						GO membrane thickness (nm)			
	0%	10%	20%	40%	50%	60%	1	2	3	4
Pure water flux ($L.m^{-2}.h^{-1}.bar^{-1}$)	1552.01	999.39	685.68	209.23	62.15	63.93	40.73	19.37	9.59	3.96

a) the GO coverage of the membrane was defined by GO covered area relative to the effective area of AAO substrate (10.5 cm^2), and the water flux measurement detail was listed in experimental section

Table 4.1. shown the water flux of membranes which covered with different amount of GO, and the plot of water flux versus this theoretically calculated GO coverage was illustrated in Figure 4.3, which exhibited that the water flux variation tendency was clearly separated into two stages: before theoretical GO coverage increased to 50%, a linear decreasing trend can be observed; but upon crossing this point, water flux was observed decreasing exponentially. Albeit water flux is usually inversely proportional to the membrane thickness for conventional membranes.[23,24] similar to our observations, an exponential decrease of water flux with increasing membrane thickness was also reported by Han et al. for a base-refluxing partially-reduced GO (brGO) membrane (~22 to 53 nm thick), and the combination of interlayer-spacing and structural defects as the water transport pathway was proposed as a mechanism to explain this phenomenal. Due to the ultrathin nature of our membranes, the abnormal exponential decrease of water flux with the increasing membrane thickness could attribute to fact that only structural defects work as water permeation route.

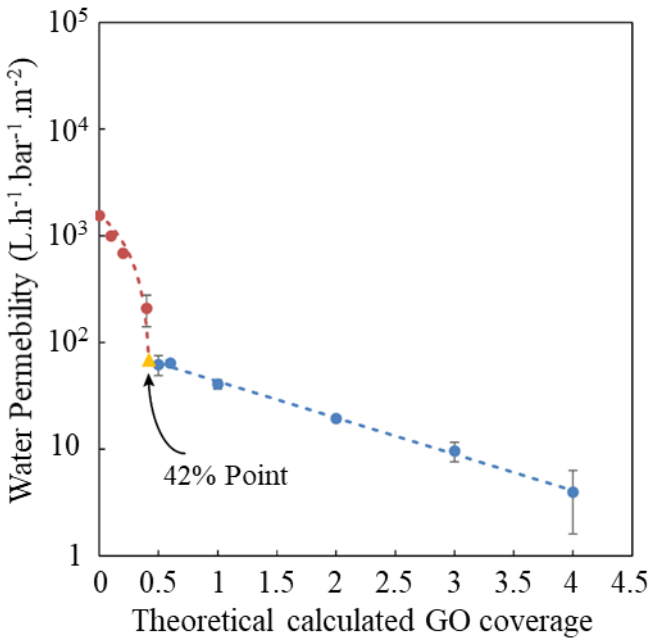

Figure 4.3 Water permeability of membranes with different degrees of theoretical calculated GO coverage.

The linear to exponential transformation of water flux decreasing tendency might suggest the change of actual degree of GO coating on AAO substrate. After GO flakes 100% cover the effective area of AAO and before forming continuous nano-channels between GO layers, the overlapped GO defects will reduce the membrane effective pore size in an exponential way, and so does the corresponding water flux. Therefore, the intersection of two plots (Figure 4.3) should represent the point where AAO substrate was just covered with monolayer of graphene oxide, and a correction coefficient can be determined accordingly to calibrate the theoretical GO coverage to actual number of GO layers. The correlation between water flux and corrected number of GO layers was plotted in Figure 4.2d. Before AAO substrate was totally covered with GO, water flux could be fitted into a function which linearly depended with GO coverage ***X***:

$$P = -1357.5 \times X + 1426.6 \quad (1).$$

As more than one layers of GO were deposited on AAO substrate, water flux can be fitted into an exponential function of ***n***

$$P = 94.958e^{-0.33n} \quad (2),$$

where n represent the number of GO layers.

The size of defects:

To estimate the size of GO defects, the separation performance of the membrane with approximately monolayer GO coating was evaluated by filtrating molecules with different sizes. Since, in this case, GO defects were assumed to provide major contribution for the membrane sieving property, the average size of the defects could be determined by the molecule which exhibits 100% size-dependent rejection. Herein, five molecules or particles with different sizes and charges, including sucrose, γ-cyclodextrin, Evans blue (EB), 5, 10, 15, 20-tetrakis-(N-methyl-4-pyridyl)-21, 23-H-porphyrin tetratosylate (TMpyP), and Au NPs were chosen to evaluate the separation performance of the membrane. As shown in Figure 2A, the monolayer GO covered membrane exhibited rejection rate of 5% for sucrose, 15% for γ-cyclodextrin, 43% for EB, 100% for TMpyP and Au NPs.

Although rejection rate of molecules through nanoporous membrane is normally dominated by both molecular size sieving mechanism and charge effect, the negative surface of GO causes the rejection rate of EB and Au NPs, which are negatively charged, only dominated by size sieving mechanism. This size-dependent rejection for EB (43%) and Au NPs (100%) indicated the effective defect size should in the range of 1.2 to 3.2 nm. Despite the monolayer GO membrane also demonstrated 100% rejection for TMpyP, the

rejection contributed to both size sieving and charge effect makes it's hard to narrow the range of the defect size accordingly. To eliminate the influence of surface charge, the monolayer GO membrane was reduced by a thermal treatment under vacuum, the corresponding rGO membrane exhibited surface property similar to the neutral graphene. The monolayer rGO membrane demonstrated higher rejection rate for sucrose (11%) and γ-cyclodextrin (27%), 83% rejection for EB, and still maintain 100% rejection for TMpyP and Au NPs. The separation performance of rGO suggests only molecules with width or dimeter smaller than 1.7 nm, such as sucrose, γ-cyclodextrin and EB, could pass through the defects (Figure 2B), and therefore the dimension of the defects should between 1.2 to 1.7 nm. Combining the average defect size with density ρ_{def}, the GO porosity could be estimated and in the range of 5.64% to 7.70%.

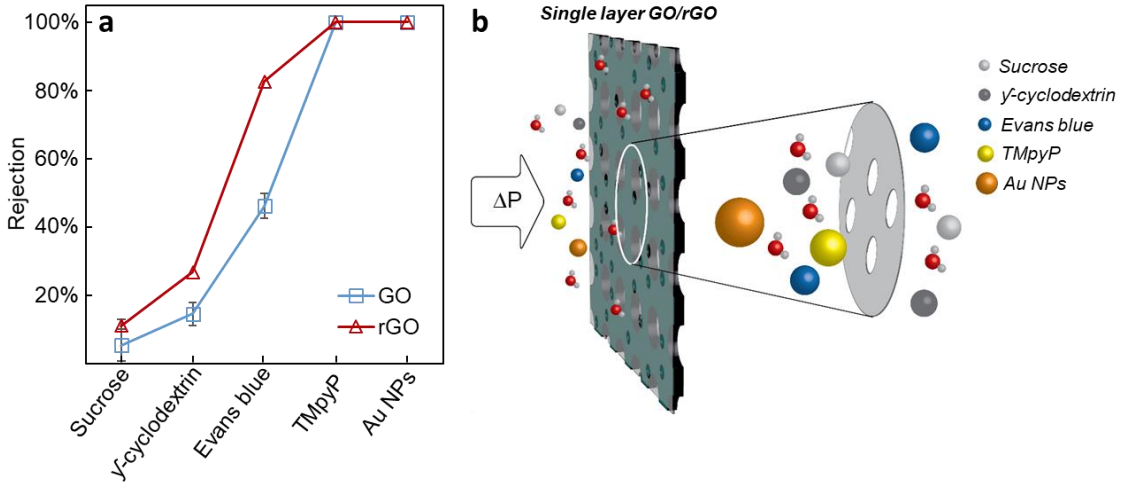

Figure 4.4 (a) Separation performance of monolayer GO/rGO membrane; (b) Schematic view of sieving property of defects.

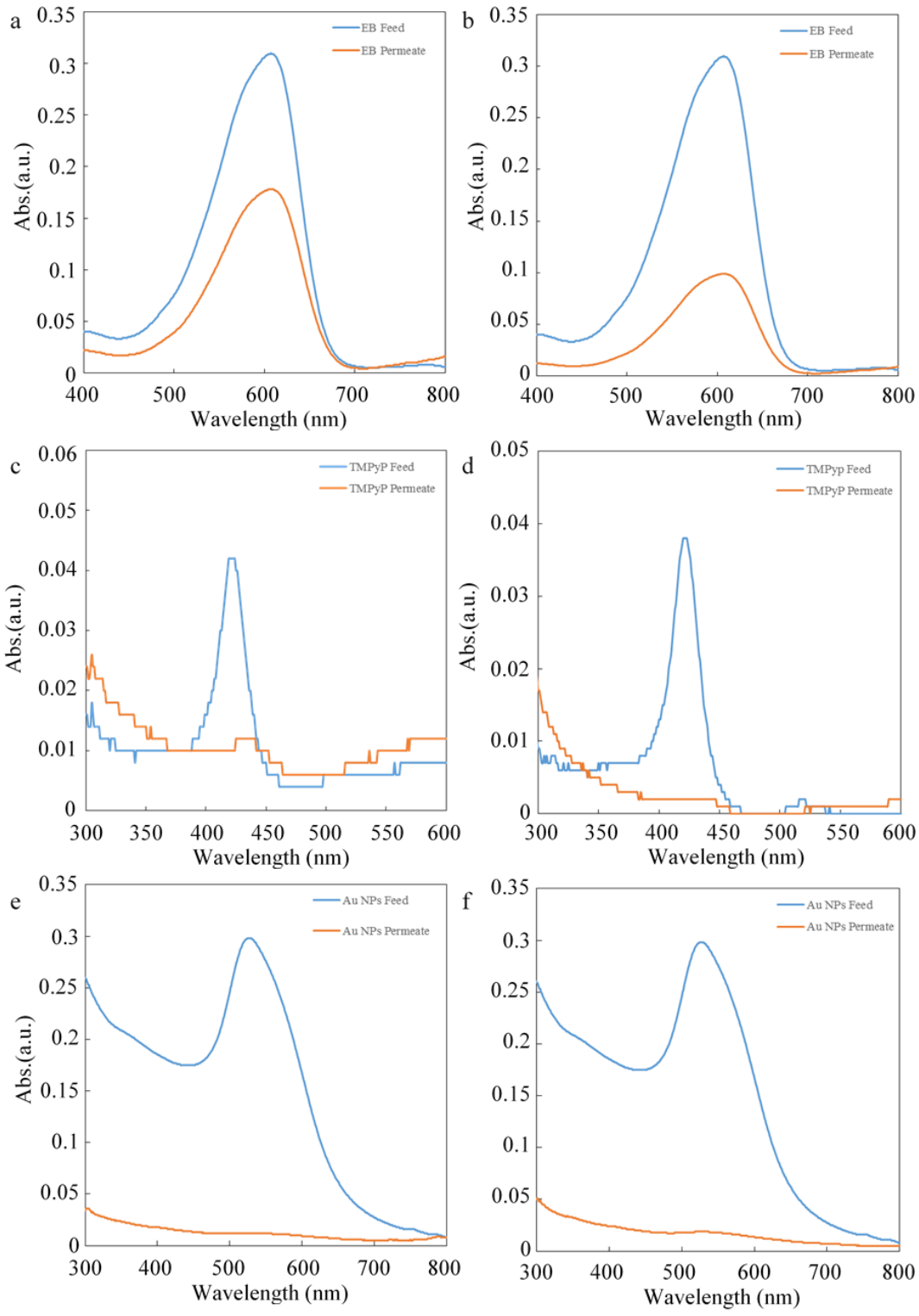

Figure 4.5 UV-vis spectra of both feed and permeate after filtering (a) Evans blue, (c) TMpyP, and (e) Au Nps through single layer GO membranes; and similar spectra by filtering (b) Evans blue, (d) TMpyP, and (f) Au Nps through reduced single layer GO membranes.

Table 4.2 Rejection results for single layer GO membrane.

GO	Charge of Molecule	rejection	Diameter or Size (nm)
Sucrose	N	5%	0.6×0.72×1.06
y-cyclodextrin	N	15%	1.2
EB	-	43%	1.2×3.1
TMpyP	+	100%	1.7×1.7
Au NPs	-	100%	3.2

Table 4.3 Rejection results for single layer rGO membrane.

rGO	Charge of Molecule	rejection	Diameter or Size (nm)
Sucrose	N	11%	0.6×0.72×1.06
y-cyclodextrin	N	27%	1.2
EB	-	83%	1.2×3.1
TMpyP	+	100%	1.7 ×1.7
Au NPs	-	100%	3.2

Water permeation model.

Based on the water permeation performance for membranes with different degree of GO coverage, a physical model could be built to investigate the water transportation mechanism and figure out physical meanings behind equation (1) and (2). As shown in Figure 1D, two separated stages were taken into consideration to build our water permeation model: 1st under the condition where GO did not 100% cover AAO substrate; 2nd more than one layers of GO were deposited on the AAO substrate. In order to simplify our model, several hypotheses needed to be made: (1) GO flakes uniformly distribute on

AAO substrate and no overlap with each other; (2) There is no water "leakage" from the edge of GO flakes, which means we only take consideration of water directly go through AAO pores and defects on GO flakes (Figure 3A); (3) Assuming all the AAO pores have uniform size, shape (circle) and water permeance $\boldsymbol{P_{AAO}}$ ($L.m^{-2}.h^{-1}.bar^{-1}$); similar assumption was made for GO defects, $\boldsymbol{P_{def}}$ ($L.m^{-2}.h^{-1}.bar^{-1}$) represents average water permeance for each defect.

As AAO substrates were covered by less than a monolayer of GO, the overall water flux of the membrane was contributed from two parts: water permeated through GO covered area and through exposed AAO area. Therefore, according to the Darcy's law, in this circumstance, the overall water permeance **P** can be described by the function

$$P = (1 - X).\eta_{AAO}.P_{AAO} + \left(\frac{1}{X.\eta_{AAO}.P_{AAO}} + \frac{1}{X.\eta_{def}.P_{def}}\right)^{-1} \quad (3),$$

where $\boldsymbol{\eta_{AAO}}$ and $\boldsymbol{\eta_{def}}$ is porosity of AAO substrate and GO flake, respectively, $\boldsymbol{\eta_{AAO}}$ could be estimated by the SEM image of AAO substrate and calculated as 60% (Figure S2). The first part eq. (3) represent water transport through uncovered AAO pores; the second part represents water transport through GO covered area, which contributed from the combination of permeance from defects on GO flakes and underneath AAO pores. By rearranging eq. (3), **P** can be re-expressed as

$$P = \eta_{AAO}.P_{AAO} - \left[\frac{X.(\eta_{AAO}.P_{AAO})^2}{\eta_{AAO}.P_{AAO} + \eta_{def}.P_{def}}\right] \quad (4),$$

which exhibited that the overall permeance was linearly depend on GO coverage $\boldsymbol{X}$. $\boldsymbol{P_{AAO}}$ and $\boldsymbol{\eta_{def}} \times \boldsymbol{P_{def}}$ which represent the water permeance of GO flake with unit area, could be estimated by combining eq. (4) with the experimentally fitted eq. (1), $\boldsymbol{P_{AAO}}$ was 2377.66 $L.m^{-2}.h^{-1}.bar^{-1}$, and $\boldsymbol{\eta_{def}} \times \boldsymbol{P_{def}}$ was calculated to be 72.62 $L.m^{-2}.h^{-1}.bar^{-1}$. Since the porosity

of GO was estimated around 5.64% to 7.70%, the water permeability of each defects on the surface should in range of 943 to 1287 $L.m^{-2}.h^{-1}.bar^{-1}$.

4.5 CONCLUSION

In conclusion, a series of ultrathin membranes with different GO coverage were prepared in this study to investigate the water permeation mechanism through defects. Water flux exhibited a transition from linear to exponential decrease with the increasing of GO covering, and the condition to fabricate single layer GO coverage was extrapolated from the turning point of the transition, and the membrane which close to single layer GO coverage was prepared accordingly. By evaluating the separation performance of this membrane, the effective defect size of GO was determined to be ~1.2-1.7 nm. Through the correlation between I_D/I_G and $\boldsymbol{L_D}$ (distances between defects), the porosity $\boldsymbol{\eta_{def}}$ of GO flakes could be estimated and in the range of 5.64% to 7.70%, and water permeability of GO defects was determined around of 943 to 1287 $L.m^{-2}.h^{-1}.bar^{-}1$. Furthermore, for the first time in this work, a physical water permeation model through GO defects was built based on experimental water flux results.

REFERENCE

(1) Dikin, D. A.; Stankovich, S.; Zimney, E. J.; Piner, R. D.; Dommett, G. H. B.; Evmenenko, G.; Nguyen, S. T.; Ruoff, R. S. Nature 2007, 448, 457.

(2) Chen, S. S.; Brown, L.; Levendorf, M.; Cai, W. W.; Ju, S. Y.; Edgeworth, J.; Li, X. S.; Magnuson, C. W.; Velamakanni, A.; Piner, R. D.; Kang, J. Y.; Park, J.; Ruoff, R. S. Acs Nano 2011, 5, 1321.

(3) Lee, C.; Wei, X. D.; Kysar, J. W.; Hone, J. Science 2008, 321, 385.

(4) Nair, R. R.; Wu, H. A.; Jayaram, P. N.; Grigorieva, I. V.; Geim, A. K. Science, 335, 442.

(5) Nair, R. R.; Wu, H. A.; Jayaram, P. N.; Grigorieva, I. V.; Geim, A. K. Science 2012, 335, 442.

(6) Hu, M.; Mi, B. Environmental Science & Technology 2013, dx.doi.org/10.1021/es400571g.

(7) Han, Y.; Xu, Z.; Gao, C. Advanced Functional Materials 2013, DOI: 10.1002/adfm.201202601.

(8) Hu, N. T.; Meng, L.; Gao, R. G.; Wang, Y. Y.; Chai, J.; Yang, Z.; Kong, E. S. W.; Zhang, Y. F. Nano-Micro Letters 2011, 3, 215.

(9) An, Z.; Compton, O. C.; Putz, K. W.; Brinson, L. C.; Nguyen, S. T. Advanced Materials 2011, 23, 3842.

(10) Burress, J. W.; Gadipelli, S.; Ford, J.; Simmons, J. M.; Zhou, W.; Yildirim, T. Angewandte Chemie-International Edition 2010, 49, 8902.

(11) Park, S.; Lee, K. S.; Bozoklu, G.; Cai, W.; Nguyen, S. T.; Ruoff', R. S. Acs Nano 2008, 2, 572.

(12) Srinivas, G.; Burress, J. W.; Ford, J.; Yildirim, T. Journal of Materials Chemistry 2011, 21, 11323.

(13) Bunch, J. S.; Verbridge, S. S.; Alden, J. S.; van der Zande, A. M.; Parpia, J. M.; Craighead, H. G.; McEuen, P. L. Nano Letters 2008, 8, 2458.

(14) Leenaerts, O.; Partoens, B.; Peeters, F. M. Applied Physics Letters 2008, 93.

(15) Jiang, D. E.; Cooper, V. R.; Dai, S. Nano Lett 2009, 9, 4019.

(16) Du, H. L.; Li, J. Y.; Zhang, J.; Su, G.; Li, X. Y.; Zhao, Y. L. J Phys Chem C 2011, 115, 23261.

(17) Schrier, J. Journal of Physical Chemistry Letters 2010, 1, 2284.

(18) Hauser, A. W.; Schwerdtfeger, P. Journal of Physical Chemistry Letters 2012, 3, 209.

(19) Suk, M. E.; Aluru, N. R. Journal of Physical Chemistry Letters 2010, 1, 1590.

(20) Schrier, J.; McClain, J. Chemical Physics Letters 2012, 521, 118.

(21) Li, Y. F.; Zhou, Z.; Shen, P. W.; Chen, Z. F. Chemical Communications 2010, 46, 3672.

(22) Cohen-Tanugi, D.; Grossman, J. C. Nano Letters 2012, 12, 3602.

(23) Peng, X.; Jin, J.; Nakamura, Y.; Ohno, T.; Ichinose, I. Nat Nano 2009, 4, 353.

(24) Nijhuis, H. H.; Mulder, M. H. V.; Smolders, C. A. Journal of Membrane Science 1991, 61, 99

APPENDIX A

COPYCRIGHT PERMISSION